Reviews in Mineralogy & Geochemistry
Vol. 88 pp. 393-450, 2022

Geochemistry of Silicate and Oxide Inclusions in Sublithospheric Diamonds

Michael J. Walter

Earth and Planets Laboratory
Carnegie Institution for Science
5241 Broad Branch Road NW
Washington D.C. 20015
USA

mwalter@carnegiescience.edu

Andrew R. Thomson

Department of Earth Sciences
University College London
Gower Street
London WC1E 6BT
UK

a.r.thomson@ucl.ac.uk

Evan M. Smith

Gemological Institute of America
50 west 47th Street
New York, NY 10036
USA

evan.smith@gia.edu

INTRODUCTION

Minerals included in diamonds provide direct information about the petrologic and chemical environment of diamond crystallization. They record information relating to local and regional mantle processes and provide important contextual information for global-scale tectonic interpretations (Stachel et al. 2005; Stachel and Harris 2008; Harte 2010; Shirey et al. 2013, 2019). Most mined inclusion-bearing diamonds originate in sub-continental, cratonic mantle lithosphere but a small percentage host mineral inclusions consistent with an origin beneath the lithosphere (~1%, Stachel and Harris 2008). Key among these inclusions are silicate and oxide minerals that provide either direct (e.g., majoritic garnet, ringwoodite) or circumstantial (e.g., $CaSiO_3$-rich and $MgSiO_3$-rich phases; ferropericlase) evidence for a high-pressure origin deep in the convecting mantle; we refer to these diamonds as "sublithospheric" although they are also commonly called "superdeep". Studies over the past four decades have provided a wealth of information to draw upon to interrogate the origins of sublithospheric diamonds and their inclusions and to speculate on broader geologic and geodynamic implications.

In the 1980s researchers began to recognize that some diamonds carry inclusions indicative of an origin beneath continental lithosphere, extending to depths even into the lower mantle (Scott-Smith et al. 1984; Moore et al. 1986; Wilding et al. 1991; Harte and Harris 1994;

1529-6466/22/0088-0007$10.00 (print)
1943-2666/22/0088-0007$10.00 (online)
http://dx.doi.org/10.2138/rmg.2022.88.07

Harris et al. 1997; Stachel et al. 1998a; Harte et al. 1999). Paramount among these are inclusions with (Mg,Fe)O and $(Mg,Fe)SiO_3$ stoichiometry, and on the basis of co-occurrence in the same diamond they were interpreted as ferropericlase and retrograde Mg-silicate perovskite (bridgmanite) from the shallow lower mantle. Discoveries of inclusions with $CaSiO_3$ stoichiometry, sometimes also co-occurring with $MgSiO_3$-rich phases and/or ferropericlase and interpreted as retrograde Ca-silicate perovskite, supported the view of a lower mantle genesis related to mantle peridotite (Harte et al. 1999; Joswig et al. 1999; Stachel et al. 2000b; Kaminsky et al. 2001; Hayman et al. 2005). Garnet inclusions with excess octahedrally coordinated silicon per formula unit (Moore and Gurney 1985, 1989; Moore et al. 1991; Stachel and Harris 1997; Stachel et al. 1998a) provided further evidence for a sublithospheric origin on the basis of experiments that revealed the pressure dependence of elemental substitutions (Akaogi and Akimoto 1977).

Over several decades numerous studies have uncovered many new examples of sublithospheric diamonds hosting these key indicator phases while also identifying a wide variety of other mineral inclusions interpreted to have an origin in the deep upper mantle to lower mantle, including but not limited to ringwoodite, stishovite, CF-phase, NAL-phase, K-hollandite, CAS phase, and phase Egg (Wirth et al. 2007; Bulanova et al. 2010; Walter et al. 2011; Thomson et al. 2014; Zedgenizov et al. 2015). The reader is referred to several recent review papers that provide an inventory of inclusion types in sublithospheric diamonds (Stachel and Harris 2008; Harte 2010; Kaminsky 2012; Shirey et al. 2013, 2019).

On the basis of mineralogical, petrological and geochemical data it has become increasingly apparent that many sublithospheric diamonds record processes that are related to subduction of lithospheric plates (Stachel et al. 2000a,b; Stachel 2001; Walter et al. 2008; Tappert et al. 2009b; Bulanova et al. 2010; Kiseeva et al. 2013b; Thomson et al. 2014; Burnham et al. 2015; Ickert et al. 2015; Shirey et al. 2019). The major and trace element geochemistry of majoritic garnet and Ti-rich $CaSiO_3$-rich phases in particular point to an origin involving subducted basaltic oceanic crust, as does the presence of rare inclusions interpreted as retrograde CF-phase and NAL-phase. The prevalence of light carbon isotopic compositions in diamonds and heavy oxygen isotopes in hosted inclusions provide additional supporting evidence for this hypothesis (Burnham et al. 2015; Ickert et al. 2015).

Sublithospheric diamonds have distinctly low N with ~70% considered Type II (e.g., $<\sim 20$ at.ppm N) and with $> 90\%$ having < 100 at.ppm N. When measurable the N is highly aggregated and dominated by B centers (~87% have >50 %B), consistent with storage in the mantle at high temperature. In comparison lithospheric diamonds have higher N, are typically classified as Type I, averaging ~250 at.ppm N but extending to > 1000 at.ppm N, and with $< 20\%$ low N Type II. Lithospheric diamonds also commonly exhibit poorly aggregated N (e.g., <50 %B) indicative of storage at cooler cratonic temperatures (Harlow 1998; Stachel et al. 2002; Pearson et al. 2003; Shirey et al. 2013; Smith and Kopylova 2014). Sublithospheric diamonds tend to be irregular in shape, show weak cathodoluminescence, have textures indicating residence in a high-strain environment and sometimes exhibit multiple nucleation sites, resorption and regrowth. Like their lithospheric counterparts, precipitation of sublithospheric diamonds is thought to occur primarily from C-saturated fluids or melts, with carbonatitic, hydrous, methane-rich and metallic liquids all implicated on the basis of the mineralogy and geochemistry of the inclusions (Walter et al. 2008; Harte 2010; Harte and Richardson 2012; Shirey et al. 2013, 2019; Smith et al. 2016b, 2018).

Here we review the mineralogy, major and trace element geochemistry of key silicate and oxide mineral inclusions in sublithospheric diamonds from global data sets assembled from the literature. The purpose of this synthesis is to focus on inclusions that have compositions of major mineral phases in upper mantle, transition zone and lower mantle assemblages in both meta-peridotite (e.g., peridotite, harzburgite, dunite) and meta-basalt (e.g., basalt, pyroxenite).

A further requirement is that inclusions occur commonly enough for substantial geochemical data to be available from locations spanning multiple continents and cratons. Accordingly, we focus on inclusions of majoritic garnet, $MgSiO_3$- and $CaSiO_3$-rich phases, ferropericlase, olivine and clinopyroxene, assembling datasets comprising 659 inclusions. We will not ignore other inclusion types entirely but will rather discuss them in relation to these more abundant inclusions.

Depending on when they formed or equilibrated relative to their diamond hosts, inclusions in diamonds are classified as protogenetic (preceding diamond formation), syngenetic (co-crystallizing with diamond) or epigenetic (crystallizing after diamond formation). Typically, a syngenetic origin for inclusions has been inferred if, regardless of their crystal system, the inclusions show a cubo-octahedral morphology that is imposed by their diamond hosts, which is most commonly the case (Harris and Gurney 1979; Meyer 1987; Stachel and Harris 2008; Bulanova et al. 2010). On the basis of the commonly observed diamond-imposed morphology the sublithospheric inclusions described herein are all assumed to be syngenetic, or at least have equilibrated synchronous with diamond crystallization and were trapped at the time of diamond growth, recording a geochemical snapshot of this process. These issues are discussed more extensively, from a geochronology perspective, in Smit et al. (2022, this volume).

Throughout this review the geochemistry and mineralogy of sublithospheric inclusions will be discussed relative to observations from petrological experiments performed at mantle conditions. Figure 1 shows experimentally derived estimates of the modal mineralogy expected in primitive mantle peridotite (e.g., pyrolite), harzburgite and mid-ocean ridge basalt (MORB) compositions (Ishii et al. 2018, 2019), illustrating how majoritic garnet, bridgmanite, Ca-perovskite, ferropericlase, olivine polymorphs and clinopyroxene dominate mineral assemblages at the depths of the deep upper mantle, transition zone and shallow lower mantle. Of the inclusions in our global dataset, ~42% are ferropericlase inclusions, 32% are majoritic garnet, $MgSiO_3$-rich and $CaSiO_3$-rich inclusions comprise about 8% each, 6% are clinopyroxene and 4% are olivine. We also discuss the occurrence of SiO_2 and retrograde CF and NAL phases that have been reported in sublithospheric diamonds, but these make up only a small fraction (< 1%) of the silicate inclusion population with reported chemistry.

Thus, the most common phases in sublithospheric diamonds mirror those in meta-basaltic and meta-peridotitic lithologies at high pressure (Harte 2010) but have been reported in proportions inconsistent with expected modal abundances in natural mantle assemblages (Fig. 1). This observation has been used to suggest the mantle might not accurately reflect a model primitive peridotite composition (Kaminsky 2012, 2017). However, diamond growth and trapping processes combined with sampling and preservation biases make observed inclusion proportions unreliable for assessing the modal mineralogy of the ambient mantle at depth (Liu 2002; Nimis et al. 2019). In this review we provide an analysis of the geochemistry of the common sublithospheric diamond inclusion types and use experimentally and theoretically derived phase relations and element partitioning data to constrain their depth of origin, plausible lithological associations and formation processes.

MAJORITIC GARNET

Garnet is the dominant aluminous mineral in mantle assemblages at depths greater than ~30–70 km, eventually becoming the second most abundant mineral in mantle peridotite and the dominant mineral in basaltic compositions throughout the deeper upper mantle and transition zone (Irifune 1987; Irifune and Ringwood 1993; Ishii et al. 2019) (Fig. 1). Garnet is chemically diverse, following the ideal formula $A_3B_2Si_3O_{12}$, where A cations occupy dodecahedral sites and B cations occupy octahedral sites. It is generally the case that divalent cations occupy the A-site in garnet, while the octahedral B-site is normally filled with trivalent cations. There are many exceptions to this simplified scheme (Grew et al. 2013)

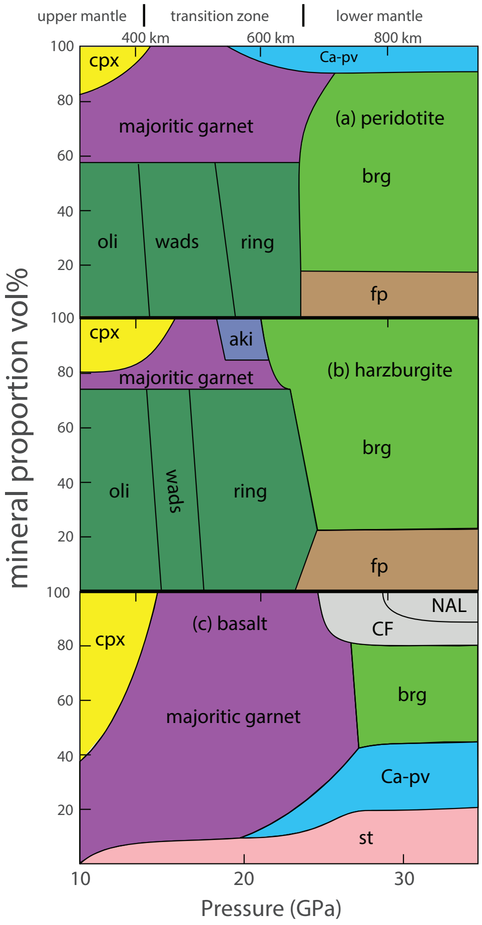

Figure 1. Mineral proportions (vol%) at 1600 °C based on the experiments of Ishii et al. (2018, 2019) in **(a)** primitive mantle peridotite, **(b)** harzburgite and **(c)** basalt bulk compositions as a function of pressure (GPa). Phase labels: cpx = clinopyroxene; oli = olivine; wads = wadsleyite; ring = ringwoodite; brg = bridgmanite; Ca-pv = Ca-silicate perovskite; st = stishovite; fp = ferropericlase; NAL = NAL phase; CF = CF phase.

but the most significant for understanding mantle garnets is that of titanium and phosphorus cations. Titanium occurs almost exclusively as Ti^{4+} in natural garnets (Locock 2008; Grew et al. 2013), and at lithospheric conditions can occupy either the tetrahedral Si site or the B-site (Waychunas 1987; Proyer et al. 2013; Ackerson et al. 2017a,b). However, at conditions relevant to sublithospheric inclusions, it is assumed that all Ti occupies the octahedral site in garnet (Ackerson et al. 2017b), charge balanced by monovalent Na^+ (or K^+) on the A-site (Ono and Yasuda 1996; Locock 2008; Proyer et al. 2013). Phosphorus, which is assumed to be exclusively pentavalent, is believed to occupy the tetrahedral silicon site, predominantly charge balanced by monovalent cations on the A-site (Haggerty et al. 1994).

Lithospheric garnets have a maximum of 3 silicon atoms per formula unit (pfu), whereas those that formed at pressures greater than about 6 to 8 GPa (equivalent to ~180–240 km depth) contain additional silicon, which is commonly referred to as the "majorite" component. The additional silicon is a consequence of the increasing solubility of pyroxene into garnet as equilibration pressure increases, and can be described by two principal substitution mechanisms:

$$2B^{3+} = {}^{VI}M^{2+} + {}^{VI}Si^{4+}\ [\mathrm{maj}] \quad (1)$$

$$A^{2+} + B^{3+} = {}^{VIII}X^{+} + {}^{VI}Si^{4+}\ [\mathrm{Na\text{-}maj}] \quad (2)$$

where ${}^{VI}M^{2+}$ is a divalent octahedral cation and ${}^{VIII}X^{+}$ is a monovalent dodecahedral cation. Both substitutions have been shown to increase with pressure, indicating that the octahedral silicon content (majorite component) in garnet is pressure dependent.

In the $MgO–Al_2O_3–SiO_2$ system, completion of substitution (1) leads to the formation of the majorite (Mj) garnet endmember ${}^{VIII}Mg_3{}^{VI}[MgSi]{}^{IV}Si_3O_{12}$ (Akaogi and Akimoto 1977; Irifune 1987), whereas substitution (2) produces the Na-majorite (NaMj) component ${}^{VIII}[Na_2Mg]{}^{VI}Si_2{}^{IV}Si_3O_{12}$ in the $Na_2O–MgO–Al_2O_3–SiO_2$ system (Irifune et al. 1989; Dymshits et al. 2013). The extent to which substitutions (1) and (2) occur is a complex function of pressure, temperature and composition (Collerson et al. 2010; Wijbrans et al. 2016; Beyer and Frost 2017; Tao et al. 2018), but substitution (1) tends to dominate in meta-peridotitic assemblages and substitution (2) in meta-basaltic assemblages (Kiseeva et al. 2013b; Thomson et al. 2021).

Importantly, any measurable majorite component can be used as a single mineral barometer via several available calibrations (Collerson et al. 2010; Wijbrans et al. 2016; Beyer and Frost 2017; Tao et al. 2018; Thomson et al. 2021). Majoritic garnets are classified as those that have a discernible majorite component (e.g., > 3 Si pfu) in their reported chemical analysis. In contrast with many previous studies, we follow the approach of Thomson et al. (2021) and explicitly account for tetrahedral phosphorus and monovalent charge balanced titanium, with the majorite component defined as:

$$\text{majorite component [maj]} = \mathrm{Si} + \mathrm{P} - 3\ (\mathrm{pfu}) \quad (3)$$

Majoritic garnet inclusions provide direct evidence of an origin at depths greater than ~ 200 km on the basis of their pressure sensitive substitutions (Eqns. 1, 2) and are the only inclusions that provide a quantifiable, chemistry-based barometer. Inclusions of majoritic garnet are widespread and have been observed in diamonds collected from a wide range of localities, including cratons in South Africa, Brazil, Western Africa, Canada, Russia and China. We have compiled major element chemical analyses from 214 garnet inclusions that have a majorite component ≥ 0.005. Data and references are provided in Table 1 (Available at: https://doi.org/10.5683/SP3/LIVK1K). Most of the majoritic garnet inclusions are reported as single or multiple occurrences in a single diamond (>60%) or co-occurrences with clinopyroxene (~20%), and there are seven co-occurrences with a $CaSiO_3$-rich phase and seven with SiO_2. Thus, the co-occurring mineralogy indicates crystallization of majoritic garnet inclusions throughout the deep upper mantle and transition zone (Fig. 1).

Many, if not most, majoritic garnet inclusions have undergone retrograde re-equilibration and exsolution (Fig. 2). Exsolution of omphacitic clinopyroxene sometimes with other minor phases has frequently been reported (Harte and Cayzer 2007; Thomson et al. 2014; Zedgenizov et al. 2014a, 2016; Burnham et al. 2016; Sobolev et al. 2016), often as volumetrically small rinds at the extremities of individual inclusions (Fig. 2). In many studies where majoritic garnet inclusions are reported, exsolution features are not described or analysed. Our experience suggests that exsolution features may have commonly gone unreported, possibly as a consequence of poorer imaging capabilities in early generations of electron microprobes. This may be especially prevalent in studies where inclusions were broken out of diamonds rather than exposed by polishing. Omission of exsolved clinopyroxene affects the bulk inclusion chemistry such that it will always lead to underestimation of pressure using empirical, chemistry-based barometers. Analysis of entire majoritic garnet inclusions is also critical for future attempts to accurately date the inclusions.

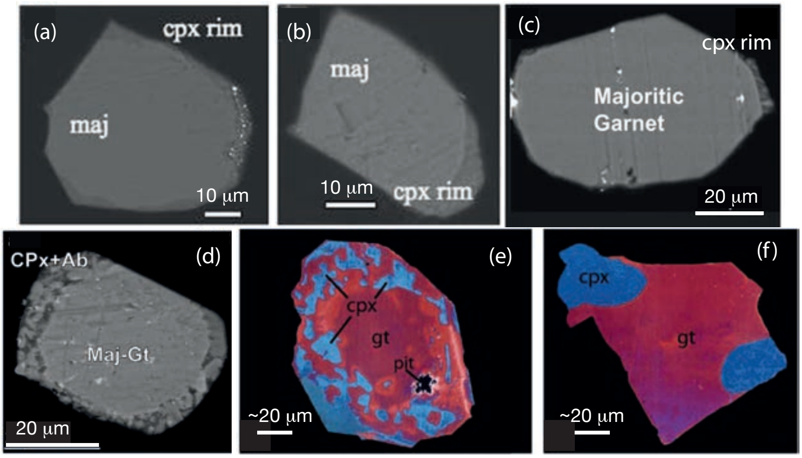

Figure 2. Backscattered electron images of majoritic garnet inclusions from the literature: **(a, b)** CC BY from Thomson et al. (2014); **(c)** Reprinted by permission from Springer Nature Customer Service Centre GmbH: Springer Nature. Bulanova et al.(2010), Copyright 2010; **(d)** Reprinted from Zedgenizov et al. (2014a) Copyright (2014), with permission from Elsevier; **(e, f)** false color: Reprinted by permission from Springer Nature Customer Service Centre GmbH: Springer Nature. Harte and Cayzer (2007), Copyright 2007. Majoritic garnet inclusions commonly exhibit exsolution of clinopyroxene, often as rinds around the margin of the inclusions (a–d), although more pervasive unmixing features also occur (e, f).

Major and minor element compositions

The major and minor element compositions of 215 majoritic garnet inclusions as determined by electron probe microanalysis are provided in Table 1 (Available at: https://doi.org/10.5683/SP3/LIVK1K) along with references describing analytical protocols. We compare these inclusion chemistries to a dataset of synthetic experimental majoritic garnets crystallized in peridotitic, harzburgitic, basaltic, sedimentary and hybrid bulk compositions across a wide range of upper mantle and transition zone pressure and temperature conditions. To our knowledge, the compositional data presented in Table 1 are based on microprobe analysis of the garnet portion of exposed/extracted inclusions without reincorporation of any exsolved material, making their derived pressures minimum estimates.

Figure 3a is a plot of CaO vs Cr_2O_3, a scheme originally constructed for classifying lithospheric garnets, which effectively delineates the majoritic garnet inclusions into two types: ***Low-Cr*** garnet inclusions exhibit low Cr_2O_3 (< ~1 wt.%), a wide range of Ca content (~ 2–18 wt.% CaO) and have Mg#s (Mg/(Mg+Fe)) predominantly lower than 0.7; ***High-Cr*** garnet inclusions exhibit high Cr_2O_3 (1–20 wt.%), low CaO (< 6 wt.%) and have Mg#s > 0.7 and typically > 0.8. In comparison with majoritic garnets from experimental studies, low-Cr inclusions are unlike garnets that crystallize in meta-peridotitic assemblages but overlap extensively with those produced in meta-basaltic assemblages that generally have extremely low Cr_2O_3 (< 0.1 wt.%) contents (Fig. 3, dark field) and a similarly wide range of CaO contents. We note that Cr_2O_3 contents in majoritic garnets produced in meta-sediment experiments invariably are not reported but are also expected to yield low-Cr garnet. Several low-Cr inclusions extend towards higher Cr_2O_3 and somewhat lower CaO contents and appear intermediate between majoritic garnet produced in meta-peridotitic and meta-basaltic assemblages (Thomson et al. 2016a).

High-Cr inclusions, with the exception of just a few, have much higher Cr than reported experimental garnets in fertile meta-peridotitic assemblages (Fig. 3, light-grey field) but overlap considerably with garnets produced in meta-harzburgitic assemblages (Fig. 3, red hex-stars), suggesting the high Cr_2O_3 may originate in highly depleted mantle compositions (Moore and Gurney 1985; Stachel et al. 2000a; Wang et al. 2000b; Schulze et al. 2008; Motsamai et al. 2018).

Figure 3b presents an alternative chemography based on CaO and TiO_2 contents. Experimental garnets generally occupy separate regions of this diagram depending on bulk composition, with meta-peridotitic garnets having low CaO and TiO_2, and meta-basaltic and meta-sedimentary garnets having higher CaO and TiO_2. Low-Cr inclusions, as distinguished primarily by lower Mg# on Figure 3b, are best represented by meta-basaltic and meta-sedimentary experimental garnets. In contrast the high-Cr inclusions have TiO_2 contents on the low-side of those observed in meta-peridotitic assemblages but are akin to some experimental meta-harzburgitic garnets. We note also that experimental meta-sediment garnets typically have Mg#s $\ll$ 0.4, generally inconsistent with the observed compositional range of majoritic garnet inclusions. Overall, low-Cr majorite inclusions are similar to lithospheric garnet inclusions that have been classified as eclogitic (Stachel et al. 2000a) and which we refer to as meta-basaltic, whereas high-Cr inclusions are similar to garnets with depleted, meta-harzburgitic affinity.

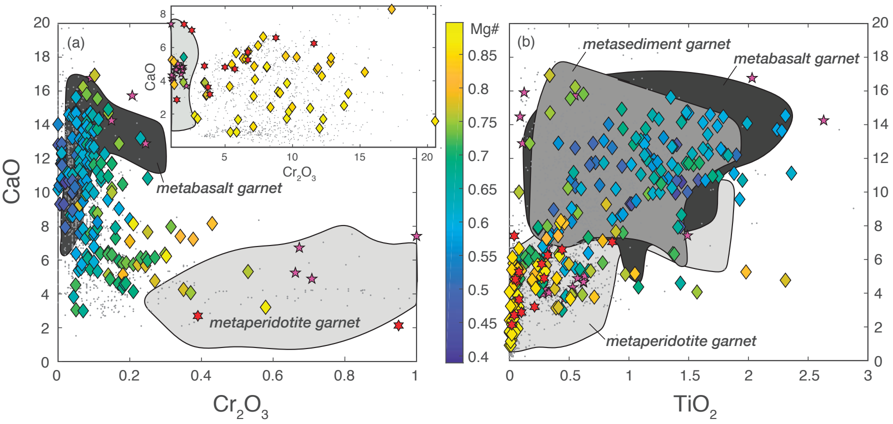

Figure 3. **(a)** CaO vs Cr_2O_3 (wt. %) and **(b)** CaO vs TiO_2 in the global majoritic garnet database (Table 1). Shaded fields depict the range of majoritic garnet compositions formed in meta-peridotitic (**light grey**), meta-basaltic (**dark grey**), and meta-sediment (**medium grey**) assemblages in high pressure-temperature experiments. Also shown are compositions for garnets formed in meta-harzburgitic assemblages (**red hex-stars**) and those produced by reaction of carbonated melt with meta-peridotite (**pink stars**). **Diamond symbols** show majoritic garnet inclusions in diamonds from the global sublithospheric database and are colored for Mg# ($Mg/[Mg+Fe_{tot}]$). **Small grey dots** are lithospheric garnet inclusions (see Stachel et al. 2022, this volume). The inset in (a) shows an expanded range for Cr_2O_3. Experimental data are from: ***meta-peridotite:*** Akaogi and Akimoto 1979; Irifune 1987; Irifune and Ringwood 1987; Herzberg and Zhang 1996; Walter 1998; Wang and Takahashi 2000; Wood 2000; Nishihara and Takahashi 2001; Hirose 2002; Ulmer and Sweeney 2002; Dasgupta et al. 2004; Kawamoto 2004; Walter et al. 2004; Brey et al. 2008; Dalou et al. 2009; Ghosh et al. 2009, 2014; Rohrbach and Schmidt 2011; Corgne et al. 2012; Tao et al. 2018; Rzehak et al. 2020; ***meta-harzburgite***: Irifune and Ringwood 1987; Ishii et al. 2019; ***meta-basalt***: Irifune et al. 1986; Yasuda et al. 1994; Ono and Yasuda 1996; Ono 1998; Okamoto and Maruyama 1999, 2004; Hirose and Fei 2002; Hammouda 2003; Litasov and Ohtani 2005; Kiseeva et al. 2013a; Thomson et al. 2016a; Beyer and Frost 2017; Zhang et al. 2020; ***meta-sediment***: Irifune et al. 1994; Ono 1998; Grassi and Schmidt 2011; Ishii et al. 2012; Bulatov et al. 2014; Brey et al. 2015; ***reaction***: Thomson et al. 2016a; Sun and Dasgupta 2019; Zhang et al. 2020.

Substitution mechanisms. Figure 4 is a plot showing majoritic garnet substitutional components (Eqns. 1–3) for inclusion and experimental garnets expressed as variation of monovalent and divalent cations. Majoritic garnets stable in meta-peridotitic assemblages predominantly follow the [maj] substitution vector. These meta-peridotitic garnets possess few, but often not zero, monovalent cations that are not charge balancing titanium (Fig. 4a), and they have an increasing proportion of divalent cations with increasing majorite component (Fig. 4b). The scatter around the ideal substitution vectors in Figure 4b may be partially explained by unidentified Fe^{3+}, but the incorporation of "extra" monovalent cations, especially at higher values of (Si + P – 3), demonstrates the occurrence of both substitution mechanisms in the experimental garnet compositions but with the [maj] substitution predominant. In contrast, experimental majoritic garnets from meta-basaltic and meta-sedimentary assemblages predominantly follow the ideal [Na-maj] substitution vector. This behavior reflects the higher alkali and lower magnesium contents in these bulk compositions, resulting in increasing monovalent cations with increasing majorite component (Fig. 4a), whereas divalent cations decrease (Fig. 4b).

Also shown on Figure 4 (as diamonds) are global majoritic garnet inclusion compositions from Table 1. High-Cr inclusions (green diamonds) cluster around the origin and extend solely along the [maj] vector to approximately 0.3. Low-Cr inclusions (blue diamonds) do not exclusively follow either substitution but rather span the range of compositions between both the [maj] and [Na-maj] substitutions. This could indicate lower Na basaltic protoliths, perhaps due to more Mg-rich basalts produced earlier in Earth's history (Pearson et al. 2003), but has previously been interpreted to indicate an association with hybrid or pyroxenitic compositions (Kiseeva et al. 2013b; Thomson et al. 2016a, 2021). Low-Cr inclusions with larger [maj] components possess higher but variable magnesium contents, $0.6 < Mg\# < 0.85$, and generally follow the [maj] substitution. However, these inclusion compositions are clearly not tied exclusively to the [maj] vector, and some skew significantly towards the [Na-maj] substitution.

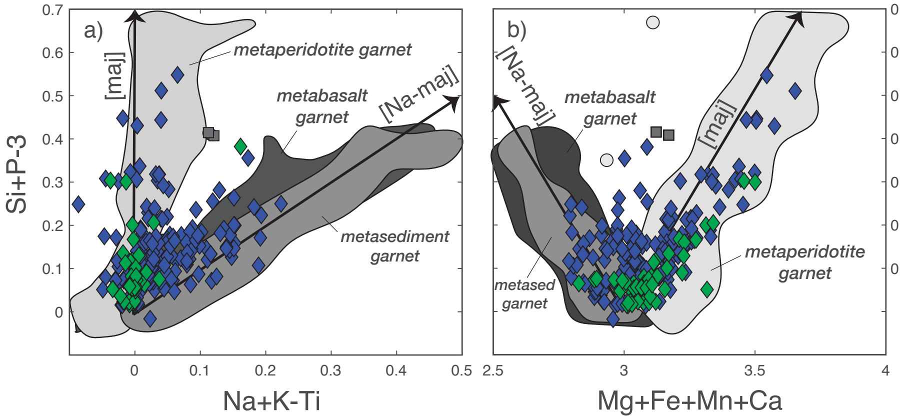

Figure 4. Majoritic garnet substitution vectors expressed in terms of Si+P–3 versus **(a)** variation in Na+K–Ti, which specifically accounts for monovalent cations charge balancing octahedral titanium, thus isolating only the components of pressure dependent substitutions, and **(b)** Mg+Fe+Mn+Ca. Since very few experimental samples have been explicitly analysed for ferric/ferrous iron content (Kiseeva et al. 2018), total iron content is calculated as Fe^{2+} together with Mg^{2+}, Ca^{2+} and Mn^{2+}. [maj] = majorite substitution; [Na-maj] = Na-majorite substitution. **Blue diamonds** are low-Cr inclusions and **green diamonds** are high-Cr inclusions. Fields showing experimental garnets are shaded as in Figure 3.

Majoritic garnet barometry

The chemical variation expressed by elemental substitutions in experimental majoritic garnet data sets has been used to calibrate empirical barometers for quantifying crystallization pressures, providing important constraints on the depths of diamond formation. The reader is referred to Nimis 2022 (this volume) for additional coverage of mineral barometry.

All published majoritic garnet barometers exclude effects of temperature from their experimental calibrations, relying solely on a parametrization of the major element chemistry to predict inclusion formation pressures (Collerson et al. 2010; Wijbrans et al. 2016; Beyer and Frost 2017; Tao et al. 2018; Thomson et al. 2021). The accuracy of calculated pressures in each study is based on the ability to reproduce their respective calibration datasets and is estimated to be ± 1–2 GPa. However, uncertainties can be much larger when these barometers are applied to experimental majoritic compositions outside the range of the calibration data. For example, when applied to majoritic garnets in the entire experimental database, Thomson et al. (2021) demonstrated much larger uncertainties among extant barometers, and a tendency for pressure underestimation, sometimes by as much as 10 GPa, when applied to the highest-pressure experimental garnets. In contrast to previous studies that used experimental subsets with limited compositional range, Thomson et al. (2021) trained a machine learning algorithm with all available experimental data to produce a barometer calibrated across the entire experimental pressure, temperature and composition space, with a significantly improved accuracy in reproducing the complete experimental dataset, especially at the highest pressures.

Shown on Figure 5 are histograms of garnet inclusion pressures calculated using majoritic garnet barometers. Despite differences in absolute pressures, all barometers exhibit a bimodal pressure distribution with distinct pressure modes at ~ 7–10 and ~ 12–15 GPa. The barometer of Thomson et al. (2021) predicts the highest-pressure modes with some inclusions indicating pressures as high as ~ 22 GPa (~ 600 km depth). However, we emphasize that many, if not all, majoritic garnet inclusions contain small amounts of exsolved omphacitic pyroxene, whose omission leads to pressure underestimation. This exsolution is presumably the effect of partial re-equilibration at lower pressures, post-entrapment, during diamond exhumation. Based on eight inclusions available from the entire global dataset where adequate data is available to estimate bulk inclusion compositions and correct for exsolution, Thomson et al. (2021) demonstrate that inclusion pressures may be underestimated by ~4 ± 2.5 GPa if exsolution features are ignored.

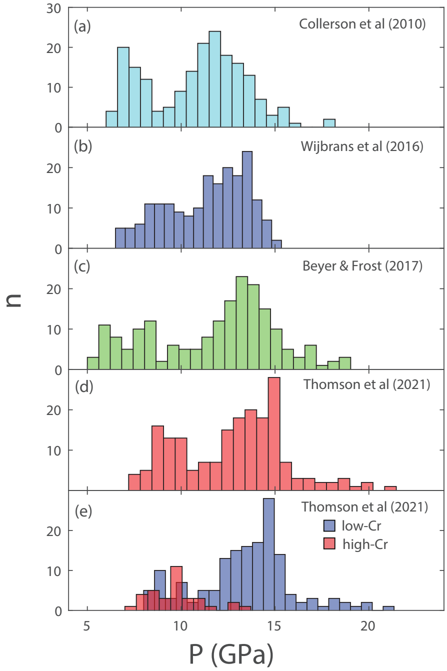

Figure 5. Pressure histograms of the global majoritic garnet inclusion dataset based on four recent experimentally calibrated empirical barometers: **(a)** Collerson et al. 2010; **(b)** Beyer and Frost 2017; **(c)** Wijbrans et al. 2016; **(d)** Thomson et al. 2021. The barometer of Tao et al. (2018) yields a distribution almost identical to Collerson et al. (2010). Note that there is no correction applied for pyroxene exsolution. **(e)** Pressure histogram applying the barometer of Thomson et al. (2021) with garnets separated on the basis of Cr-content.

Figure 5e shows histograms of majoritic garnet inclusion pressures calculated using the barometer of Thomson et al. (2021) separated according to low-Cr and high-Cr varieties. The distribution demonstrates that nearly all of the high-pressure mode is occupied by low-Cr garnets, which are meta-basaltic in composition. The concentration of the high-Cr majoritic garnets at lower pressures (e.g., < ~10 GPa) suggests that the diamonds hosting these depleted meta-peridotitic inclusions formed in a unique environment compared to high-Cr inclusions, possibly even in deep cratonic lithosphere rather than in the convecting mantle.

Trace element compositions

Measurements of trace element concentrations, mostly made using SIMS analyses at the Edinburgh Ion Probe Facility (EIMF), are reported for fifty-eight majoritic garnet inclusions in Table 2 (Available at: https://doi.org/10.5683/SP3/LIVK1K). Figure 6 shows trace element 'spidergrams' for majoritic garnet inclusions with element abundances normalized to the silicate Earth model of McDonough and Sun (1995), which we refer to as BSE (bulk silicate Earth). We have opted to maintain the low-Cr (Fig. 6a,c) and high-Cr (Fig. 6b,d) divisions and find that trace element abundance patterns are also generally distinct between these two groups.

Low-Cr majorite inclusions are systematically more enriched in trace elements than high-Cr inclusions, generally by about one order of magnitude. Virtually all majoritic garnet inclusions possess a negative Sr anomaly and many have positive Zr and Hf anomalies. Rare earth element (REE) patterns generally show depletions in the light rare earths (LREE), with Lu/La ratios ranging from ~ 0.15–1800 with >80% of inclusions greater than unity. Low-Cr inclusions generally have higher Lu/La than high-Cr inclusions. Where measured,

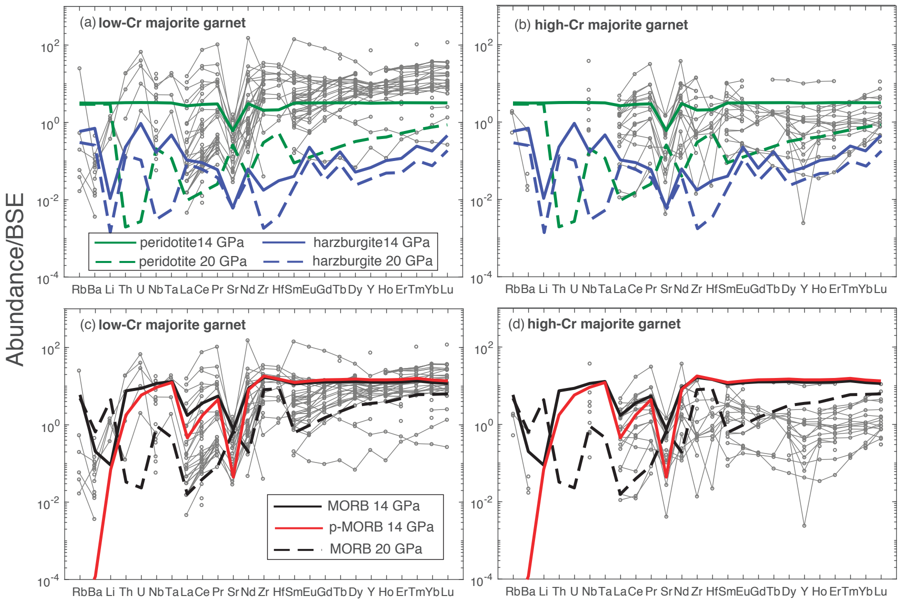

Figure 6. Trace element abundances in majoritic garnet inclusions from the global dataset. **(a)** and **(c)** show low-Cr garnets and **(b)** and **(d)** high-Cr garnets. Shown in panels **(a)** and **(b)** are calculated abundance patterns for majoritic garnet expected in meta-peridotitic and meta-harzburgitic mineral assemblages at 14 GPa (garnet + wadsleyite + clinopyroxene) and 20 GPa (garnet+ ringwoodite + Ca-silicate perovskite). Shown in panels **(c)** and **(d)** are calculated abundance patterns for majoritic garnet expected in meta-basaltic (MORB) mineral assemblages at 14 GPa (garnet + clinopyroxene + stishovite) and 20 GPa (garnet + Ca-silicate perovskite + stishovite), and in 'processed' MORB at 14 GPa (garnet + clinopyroxene + stishovite).

Th, U and Nb are relatively enriched relative to BSE whereas Ba, Li and Rb, with a few exceptions, are variably depleted. Small negative Eu and Y anomalies are present in some low-Cr majoritic garnets, whereas a number of the high-Cr inclusions exhibit large Y anomalies.

Also shown on Figure 6 for comparison with observed inclusions are calculated trace element concentrations estimated for majoritic garnet in subsolidus meta-peridotitic, meta-harzburgitic and meta-basaltic (MORB) mineral assemblages. Subsolidus majoritic garnet compositions were calculated using published mineral/melt partition coefficients for experimentally constrained phase assemblages following the approach of Thomson et al. (2016b).

For example, the following mass balance defines the trace element contents of any single phase in a multi-phase assemblage:

$$X_i^{\text{total}} = \alpha X_i^{\text{A}} + \beta X_i^{\text{B}} + \gamma X_i^{\text{C}} + \ldots \tag{4}$$

$$X_i^{\text{A}} = X_i^{\text{total}} \Bigg/ \left(\alpha + \beta \frac{D_i^{\text{B/melt}}}{D_i^{\text{A/melt}}} + \gamma \frac{D_i^{\text{C/melt}}}{D_i^{\text{A/melt}}} + \ldots \right) \tag{5}$$

where X_i^A, X_i^B, X_i^C are the concentrations of trace element i in phase A, B, and C, D_i are mineral/melt partition coefficients, and α, β and γ are the proportions of phases A, B and C in the phase assemblage. Bulk trace element contents (X_i^{total}) for peridotite are taken as BSE (McDonough and Sun 1995), for harzburgite are taken from the average of nine samples formed by melt depletion in a subduction zone environment as reported in Secchiari et al (2020), and mean mid-ocean ridge basalt (ALL-MORB) is used to represent basaltic compositions (Gale et al. 2013). 'Processed' MORB is calculated as described in Thomson et al. (2016b) and is used as an estimate of subducted MORB crust post sub-arc dehydration. Table 3 (Available at: https://doi.org/10.5683/SP3/LIVK1K) provides the source of partition coefficients and the phase proportions used in each phase assemblage to calculate trace element abundances in coexisting phases in mineral assemblages at pressures from the transition zone to the lower mantle.

Figure 6a shows that low-Cr inclusions are unlike those expected in meta-peridotitic assemblages at conditions of the transition zone; majoritic garnet in equilibrium with Ca-silicate perovskite in meta-peridotite or meta-harzburgite are significantly more depleted than the low-Cr inclusions. Peridotitic majoritic garnets at shallow transition zone conditions in equilibrium with wadsleyite and clinopyroxene have similar overall levels of enrichment relative to BSE as some low-Cr inclusions but the overall pattern and especially the abundances and slope of the REE and mild Sr anomaly are unlike the majoritic garnet inclusions. Consistent with their Ca and Cr contents, trace elements show that low-Cr majoritic garnets do not have meta-peridotitic affinity.

In contrast, Figure 6c demonstrates that low-Cr majoritic inclusions share characteristics of majoritic garnet compositions expected in meta-basaltic assemblages. The calculated trace element abundances of garnet at 14 GPa are generally within the range observed in low-Cr inclusions, while at 20 GPa calculated abundances are at the lower range of the inclusions due to coexistence with Ca-silicate perovskite. We note that the depletions in some large ion lithophile elements (LILE) and Sr are best reproduced in the 'processed' MORB composition, consistent with loss during sub-arc slab devolatilization. While some low-Cr inclusions have relatively flat middle to heavy REE similar to meta-basaltic garnet at 14 GPa (e.g., Lu/Sm near unity), many show depletions in LREE and MREE similar to MORB at 20 GPa, although with higher overall abundances by up to an order of magnitude. Thus, while low-Cr inclusions are more like meta-basaltic garnet compositions they generally have trace elements abundances that are elevated relative to expectations for trapped portions of subsolidus materials in processed MORB.

Overall abundance levels in high-Cr inclusions are generally similar to those expected in meta-peridotitic lithologies. They tend to possess negative Sr anomalies and generally have relatively flat REE abundance patterns (Fig. 6b), most akin to meta-peridotite at lower pressures where Ca-silicate perovskite is not stable, which is consistent with their lower calculated pressures (Fig. 5e). There are very few measurements of LILE, Th, U, Nb, Ta for high-Cr inclusions; while this may suggest they were very depleted in these components, it is important to note that these elements were not analyzed in all studies. Two additional features of the high-Cr inclusions are that many have negative Y anomalies, whose origin is unclear but are suggested to be associated with Earth surface processes (Thomson et al. 2016b). Additionally, several of the high chromium samples possess sinusoidal REE patterns, features that are common amongst lithospheric xenoliths and are thought to record the influence of metasomatic fluids (Stachel et al. 1998b; Wang et al. 2000b; Stachel et al. 2004), potentially consistent with their origin in the deep lithospheric mantle.

$CaSiO_3$-RICH AND $MgSiO_3$-RICH INCLUSIONS

Inclusions in sublithospheric diamonds with ABO_3 stoichiometry occur in both calcium-rich and magnesium-rich varieties. On the basis of their mineralogy and chemistry these inclusions are commonly interpreted to represent high-pressure phases with a former ‘perovskite’ structure that have retrogressed to lower-pressure polymorphs or phase assemblages (Harte and Harris 1994; Stachel et al. 1998a, 2000b, 2005; Harte et al. 1999; Joswig et al. 1999; Hutchison et al. 2001; Kaminsky et al. 2001; Brenker et al. 2002, 2005, 2021; Davies et al. 2004b; Hayman et al. 2005; Walter et al. 2008, 2011; Tappert et al. 2009b; Harte 2010; Thomson et al. 2014; Zedgenizov et al. 2015, 2016, 2020; Burnham et al. 2016; Nestola et al. 2018). As such, these inclusions are some of the few known samples thought to originate from the deep transition zone and shallow lower mantle and, therefore, can provide insight into the lithologies and processes occurring at these depths.

The mineral perovskite *sensu stricto* has a $CaTiO_3$ composition, is orthorhombic, and crystallizes in the *Pnma* space group. Perovskite-structured phases with both $MgSiO_3$ (bridgmanite) and $CaSiO_3$ compositions crystallize in high-pressure and temperature experiments in meta-basaltic and meta-peridotitic assemblages (Liu and Ringwood 1975; Yagi et al. 1978; Ito et al. 1984; Irifune 1987; Kesson et al. 1994; Kesson et al. 1995). $MgSiO_3$-rich inclusions interpreted as former bridgmanite occur as retrograde enstatite. $CaSiO_3$ and $Ca(Si,Ti)O_3$ inclusions in diamond are typically interpreted as products of originally perovskite-structured phases that have retrogressed to lower-pressure polymorphs, with $CaSiO_3$ most often occurring as breyite (formerly known as calcium walstromite) but wollastonite has also been observed (Nestola et al. 2018; Smith et al. 2018). $CaTiO_3$ perovskite coexisting with $CaSiO_3$ is also observed as part of composite inclusion assemblages.

Here we review the chemistry of $MgSiO_3$-rich and $CaSiO_3$-rich phases that occur as inclusions in sublithospheric diamonds. We recognize that the inclusions do not occur as high-pressure perovskite-structured polymorphs but rather as retrograde minerals, and we will review the evidence for their identification as former bridgmanite and Ca-silicate perovskite minerals, respectively.

$CaSiO_3$-RICH INCLUSIONS

The compilation of $CaSiO_3$-rich inclusion compositions includes fifty-three samples in diamonds from four cratons, forty-one of which are from South America. Mineralogical identification of the observed inclusions is often assumed on the basis of major element stoichiometry, although in some studies crystal structures have been determined by Raman spectroscopy or X-ray diffraction (Joswig et al. 1999; Brenker et al. 2005; Walter et al. 2011; Thomson et al. 2014; Burnham et al. 2016; Korolev et al. 2018; Nestola et al. 2018; Smith et al. 2018). Inclusions are either single phase $CaSiO_3$ (breyite or wollastonite) or composite mixtures of $CaSiO_3$ and other phases including $CaTiO_3$ (perovskite), $CaSi_2O_5$ (titanite-structured), Ca_2SiO_4

(larnite) and ZrO_2 (Fig. 7). Composite inclusions with overall $Ca(Si,Ti)O_3$ stoichiometry are typically interpreted to represent unmixing of an originally homogeneous phase; the alternative to the unmixing interpretation is that a portion of a 'rock' or melt was trapped encapsulating exactly a composition with ABO_3 stoichiometry, which is exceedingly improbable.

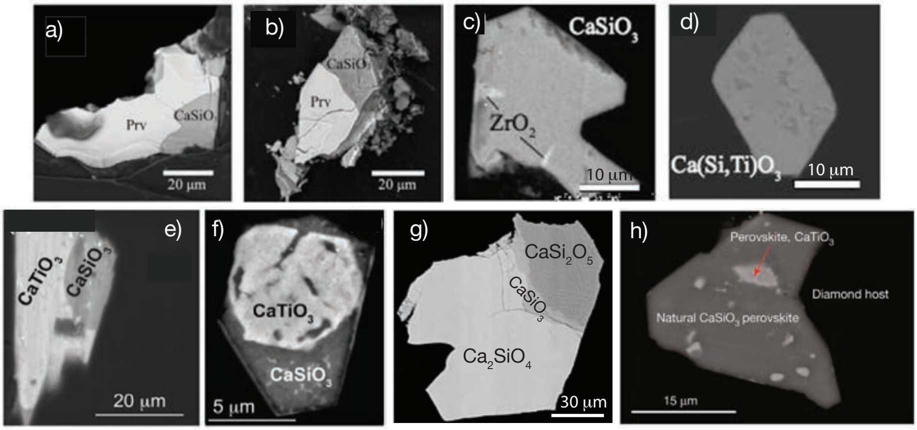

Figure 7. Backscattered electron images of composite $CaSiO_3$-rich inclusions from previous studies: **(a–b)** Prv = $CaTiO_3$ perovskite. Reprinted by permission from Springer Nature Customer Service Centre GmbH: Springer Nature. Hayman et al. (2005), Copyright 2005; **(c–d)** CC BY from Thomson et al. (2014); **(e, f)** Walter et al. 2008, reprinted by permission from Springer Nature Customer Service Centre GmbH: Springer Nature. Bulanova et al. (2010), Copyright 2010; **(g)** Reprinted from Joswig et al. (1999) Copyright (1999), with permission from Elsevier; **(h)** Reprinted by permission from Springer Nature Customer Service Centre GmbH: Springer Nature. Nestola et al. (2018b), Copyright 2018.

In five instances $CaSiO_3$-rich phases co-occur in the same diamond with $MgSiO_3$-rich phases, in nine cases they co-occur with ferropericlase, and in only three diamonds with both $MgSiO_3$ and ferropericlase. These non-touching, co-occurring assemblages are generally attributed to a lower mantle association (Stachel et al. 2000b; Kaminsky et al. 2001; Davies et al. 2004a; Hayman et al. 2005; Zedgenizov et al. 2014a) (Fig. 1). In five cases a $CaSiO_3$-rich phase occurs in the same diamond with majoritic garnet (Kaminsky et al. 2001; Hayman et al. 2005; Bulanova et al. 2010; Zedgenizov et al. 2014a). Other phases co-occurring with $CaSiO_3$-rich phases include SiO_2 (likely former stishovite), merwinite ($Ca_3Mg(SiO_4)_2$), $CaSi_2O_5$-titanite, chromite, Fe–Ni-metal and sulphide (Stachel et al. 2000b; Kaminsky et al. 2001; Brenker et al. 2005, 2021; Hayman et al. 2005; Walter et al. 2008; Bulanova et al. 2010; Thomson et al. 2014; Zedgenizov et al. 2014a,b; Burnham et al. 2016; Smith et al. 2016b).

Major and minor element compositions

Reported major and minor element compositions of $CaSiO_3$-rich inclusions are provided in Table 4 (Available at: https://doi.org/10.5683/SP3/LIVK1K). Many workers have noted that $CaSiO_3$-rich inclusions tend to be nearly phase pure, with analyzed compositions showing only minor amounts of MgO, Al_2O_3 and FeO in nearly all occurrences (Harte et al. 1999; Joswig et al. 1999; Stachel et al. 2000b; Kaminsky et al. 2001; Davies et al. 2004b; Hayman et al. 2005; Walter et al. 2008; Bulanova et al. 2010; Thomson et al. 2014; Zedgenizov et al. 2014a; Nestola et al. 2018). Most notably, MgO abundances are < 0.1 wt% in 29 of 40 inclusions where MgO was measured, and in those cases where MgO is not reported inclusions presumably also have exceptionally low abundances of this routinely measured oxide. Such low MgO contents are inconsistent with expectations for Ca-silicate perovskite in a meta-peridotitic assemblage at mantle temperatures (Wang et al. 2000a; Walter et al. 2008; Bulanova et al. 2010; Armstrong et al. 2012; Thomson et al. 2014).

We divide the $CaSiO_3$-rich inclusions into two groups based on a distinct compositional gap in TiO_2 contents, resulting in forty ***low-Ti*** inclusions with $TiO_2 < 0.7$ wt% and thirteen ***high-Ti*** inclusions with $TiO_2 > 2$ wt%. Figure 8 is a plot of Ti/(Ti + Si) versus (a) Mg/(Mg + Ca) and (b) Al (per formula unit), illustrating the unusual bulk compositions of many of the inclusion relative to the compositions of Ca-silicate perovskite in meta-peridotitic and meta-basaltic mineral assemblages synthesized in experiments.

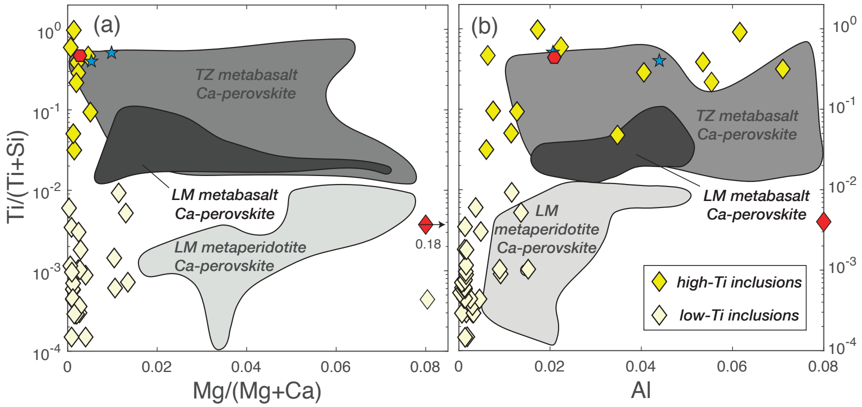

Figure 8. Molar Ti/(Ti+Si) versus **(a)** Mg/(Mg+Ca) and versus **(b)** Al (per formula unit) for $CaSiO_3$-rich inclusions (low-Ti = **light yellow diamonds**; high-Ti = **dark yellow diamonds**) in the global database. The **red diamond** is the calculated composition of an alkali and Cr-rich inclusion reported in Tschauner et al. (2021). Shown for comparison are fields for Ca-silicate perovskite synthesized in experimental studies: **Light grey field** shows Ca-silicate perovskite equilibrated with a lower mantle meta-peridotitic assemblage (LM = ± bridgmanite / ferropericlase / majorite); **Medium grey field** shows Ca-silicate perovskite equilibrated with a transition zone meta-basaltic assemblage (TZ = ± majorite / st / CAS phase / K-hollandite / aragonite / melt) and the **dark grey field** Ca-silicate perovskite equilibrated with a lower mantle meta-basaltic assemblage (LM = ± Al-bridgmanite /majorite / st /NAL / CF). Experimental data are from (Irifune 1994; Wood 2000; Ono et al. 2001; Hirose 2002; Hirose and Fei 2002; Litasov and Ohtani 2005; Ishii et al. 2011, 2018; Kiseeva et al. 2013a; Thomson et al. 2016a; Kuwahara et al. 2018). **Blue stars** are Ca-silicate perovskite produced by reaction between carbonated melt derived from basaltic crust and reducing primitive mantle (+majorite / ringwoodite / fp) (Thomson et al. 2016a). The **red hexagon** shows Ca-silicate perovskite equilibrated with majoritic garnet, magnesite and carbonated melt at 20 GPa, 1475 °C, in the system $CaO–MgO–Al_2O_3–TiO_2–SiO_2– CO_2$ (Walter et al. 2008).

Low-Ti $CaSiO_3$ inclusions. Most of the low-Ti $CaSiO_3$-rich inclusions are unlike those synthesized in experiments, having both exceptionally low MgO and TiO_2 contents (Fig. 8a), and also typically very low Al_2O_3 (Fig. 8b) and FeO contents. Three of the low-Ti inclusions co-occur in diamonds together with $MgSiO_3$-rich inclusions that have been interpreted to be of lower mantle origin, yet in each case the MgO contents are < 0.1 wt% (Stachel et al. 2000b; Davies et al. 2004b; Hayman et al. 2005; Zedgenizov et al. 2014a). Such low MgO contents are inconsistent with Ca-silicate perovskite in equilibrium with bridgmanite ($MgSiO_3$) in a lower mantle assemblage at mantle temperatures (Fig. 8), which have much higher MgO contents (Irifune et al. 2000; Walter et al. 2008). Only one inclusion, from Machado River in Brazil, has an MgO content high enough to potentially be consistent with an origin as part of a meta-peridotitic assemblage at lower mantle pressures and temperatures, albeit with much lower Ti (Burnham et al. 2016). Also shown on Figure 8 are experiments where Ca-silicate perovskite is in equilibrium with transition zone phases like majoritic garnet and ringwoodite in metabasaltic compositions. These experiments produce some Ca-silicate perovskites with lower Mg contents but with much higher Ti contents. In any case, the compositions of nearly all low-Ti $CaSiO_3$ inclusions are very unlike Ca-silicate perovskites produced in equilibrium with bridgmanite in primitive mantle peridotite at temperatures appropriate for ambient lower mantle (e.g., > 1700 °C).

A potential explanation for the low MgO content of the low-Ti $CaSiO_3$ inclusions is that they formed initially as Ca-silicate perovskite in equilibrium with bridgmanite but at low temperatures, considerably lower than in the experiments plotted on Figure 8 (Irifune et al. 2000; Armstrong et al. 2012). Irifune et al. (2000) demonstrated that at temperatures of 1500 °C and above, substantial (~10× higher than inclusions) MgO dissolves into Ca-silicate perovskite and suggested that the low-MgO content in $CaSiO_3$-rich inclusions reported in Harte et al. (1999) might reflect equilibration and inclusion entrapment at <1200 °C where the solvus widens, possibly in cool subducted lithosphere. Currently the solvus at temperatures below ~1400 °C is poorly constrained experimentally but could potentially be used as a thermometer for low-Ti $CaSiO_3$ inclusions.

High-Ti $CaSiO_3$ inclusions. Of the thirteen inclusions identified as having high titanium, ten are described as composite inclusions of $CaSiO_3$ + $CaTiO_3$ (e.g., Fig. 7). Reconstructing the bulk composition of composite inclusions, when attempted, has been done either through broad beam analysis of entire inclusions, or by analyzing phases separately and recombining them based on estimates of their modal abundance; both of these approaches can have considerable uncertainties (Walter et al. 2008, 2011; Bulanova et al. 2010; Thomson et al. 2014). Like low-Ti inclusions, high-Ti inclusions also have very low MgO contents but have higher Al_2O_3 and FeO (Fig. 8). Armstrong et al. (2012) showed that as the Ti-content in Ca-silicate perovskite in equilibrium with bridgmanite increases so does the solubility of MgO, such that the high-Ti inclusions should have levels of MgO at the several weight percent level if they formed in the lower mantle. On this basis, equilibrium of the high-Ti inclusions with bridgmanite at lower mantle pressures is excluded for all high-Ti inclusions.

As shown on Figure 8, some experimental Ca-silicate perovskites produced in meta-basaltic assemblages at transition zone pressures in equilibrium with majoritic garnet have low-Mg contents and high-Ti contents consistent with the high-Ti inclusions. We note that the experiments that best reproduce the inclusions are at relatively low temperatures and were produced in equilibrium with hydrous fluids or carbonatitic melts. Especially noteworthy are two experiments at 1000 °C where Ca-silicate perovskite is equilibrated with majoritic garnet, stishovite and a hydrous fluid, and has very low MgO contents but relatively high Al_2O_3 contents (Litasov and Ohtani 2005). Walter et al. (2008) reported on experiments in a simplified carbonated basalt system that showed $Ca(Si,Ti)O_3$-perovskite with very low MgO contents in equilibrium with majoritic garnet (red hexagon, Fig. 8). Similarly, Ca-silicate perovskite compositions in equilibrium with majoritic garnet and carbonatitic melt in experiments with basaltic starting compositions, or where carbonated melts were reacted with peridotite, also have high-TiO_2, low-MgO and high Al_2O_3 (Fig. 8b) and FeO similar to the inclusions (Walter et al. 2008; Thomson et al. 2016a).

Phase Relations

$CaSiO_3$-rich inclusions are often cited as evidence for diamond formation in the lower mantle (Harte et al. 1999; Joswig et al. 1999; Stachel et al. 2000b; Hayman et al. 2005; Harte 2010; Walter et al. 2011; Burnham et al. 2016; Smith et al. 2016b, 2018; Nestola et al. 2018). However, phase relations do not require a lower mantle or even transition zone origin for perovskite-structured $CaSiO_3$-rich phases to occur as inclusions in diamond (Kubo et al. 1997; Walter et al. 2008; Bulanova et al. 2010; Woodland et al. 2020; Brenker et al. 2021). Because the inclusions typically have only minor amounts of MgO, Al_2O_3 and FeO, phase relations for $CaSiO_3$-rich inclusions are well represented in the system CaO–SiO_2–TiO_2.

Low-Ti $CaSiO_3$ inclusions. Figure 9a shows phase relations in the $CaSiO_3$ system. Ca-silicate perovskite is stable at pressures above about 13 to 14 GPa at temperatures expected in the mantle, in contrast to the higher pressures at which Ca-silicate perovskite stabilizes in meta-basaltic or meta-peridotitic mantle assemblages (~20 GPa, Fig. 1). $CaSiO_3$ decomposes

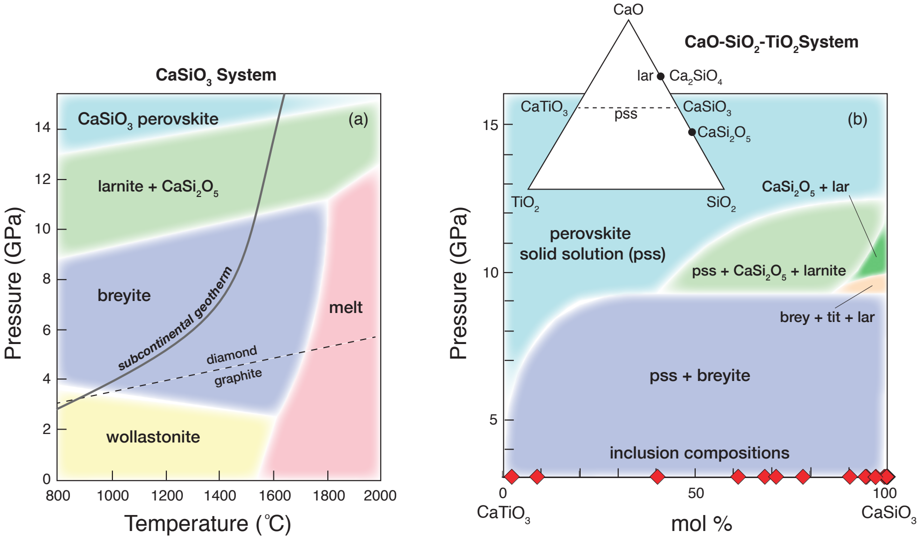

Figure 9. (a) Phase relations in the system $CaSiO_3$, after Figure 1 in Woodland et al. (2020). **(b)** Phase relations in the system $CaTiO_3$-$CaSiO_3$ after Kubo et al. (1997) in mol%. Phase relations are binary at compositions < ~40 mol% $CaSiO_3$ above ~9 GPa, with the ternary phase chemography depicted in the inset figure. **Red diamonds** are $CaSiO_3$-rich inclusions from the global dataset. Phase labels: pss = perovskite solid solution; lar = larnite; brey = breyite.

to a mixture of larnite (Ca_2SiO_4) plus titanite-structured $CaSi_2O_5$ between about 10 and 13 GPa, transforming to breyite at pressures below about 9 to 10 GPa and to wollastonite below ~3 GPa. Of the low-Ti inclusions where crystal structure was determined by Raman or X-ray diffraction, the majority indicate breyite as the $CaSiO_3$ phase (Table 4—Available at: https://doi.org/10.5683/SP3/LIVK1K). If the inclusions were originally formed as Ca-silicate perovskite, phase relations suggest the diamonds were transported from depths of at least ~ 400 km (~13 GPa) to depths of < 300 km where breyite is stable (~10 GPa) prior to exhumation by kimberlite. Wollastonite has also been observed in one inclusion (Nestola et al. 2018; Smith et al. 2018), which has a stability at less than about 3 GPa (Chatterjee et al. 1984; Sokolova and Dorogokupets 2021), requiring temperatures below ~1000 ºC for both wollastonite and diamond to co-exist in equilibrium (Fig. 9a).

Four of the low-Ti $CaSiO_3$ inclusions show evidence of retrograde phase unmixing consistent with decompression. Joswig et al. (1999) reported on a low-Ti $CaSiO_3$ inclusion from Kankan (Guinea) with the composite assemblage breyite + larnite + titanite (Fig. 7g), which would ostensibly place its last equilibration directly on the phase boundary at ~10 GPa (Fig. 9a). Burnham et al. (2016) report clinopyroxene exsolution in two inclusions from Machado River (Brazil), one with a reconstructed bulk composition that could be in equilibrium with bridgmanite as described below. Two of the low-Ti $CaSiO_3$ inclusions from Juina (Brazil) co-occur with majoritic garnet (Tables 1 and 4—Available at: https://doi.org/10.5683/SP3/LIVK1K) and barometry yields pressures of ~13 and ~8 GPa but no information about possible clinopyroxene exsolution is provided so these are minimum pressures. Nine of the low-Ti inclusions co-occur with ferropericlase with Mg#s ranging from 0.75 to 0.9, with three of these co-occurring with an $MgSiO_3$-rich phase, indicating a deep transition zone or lower mantle origin related to a meta-peridotitic assemblage. However, we reiterate, the low MgO contents preclude equilibration with bridgmanite along a mantle geotherm and indicate either that the inclusions did not equilibrate with bridgmanite or did so at a significantly lower temperature, possibly in cold subducted lithosphere.

High-Ti $CaSiO_3$ inclusions. Figure 9b shows phase relations along the $CaTiO_3$-$CaSiO_3$ join. Of the ten composite inclusions exhibiting unmixing of $CaSiO_3$ and $CaTiO_3$ phases (Fig. 7), in five cases $CaSiO_3$ breyite and $CaTiO_3$ perovskite were confirmed through Raman or X-ray diffraction (Table 4—Available at: https://doi.org/10.5683/SP3/LIVK1K). Figure 9b shows that the pressure at which a single-phase $Ca(Si,Ti)O_3$ perovskite solid solution stabilizes depends on Ti-content, ranging from ~13 GPa at the $CaSiO_3$-rich end to <5 GPa at the $CaTiO_3$-rich end. If the high-Ti inclusions originated as perovskite solid solutions then crystallization pressures of greater than ~6 to 13 GPa are indicated, with most > 9 GPa. Five of the high-Ti $CaSiO_3$ inclusions co-occur with majoritic garnet, and barometry yields pressures of ~11, 12, 13, 14 and 22 GPa with no correction for clinopyroxene exsolution (Thomson et al. 2021). These pressures are consistent with formation of the composite $CaSiO_3$ inclusions originally as perovskite solid solutions but at depths spanning the deep upper mantle and transition zone rather than the lower mantle, consistent with their low MgO contents.

Pressures based on co-occurring majoritic garnet for the entire $CaSiO_3$-rich inclusion suite are generally consistent with minimum estimates from elastic barometry (Anzolini et al. 2018) and suggest that pressures of Ca-silicate perovskite entrapment in diamond may be considerably lower than expectations based on phase relations of mantle lithologies (Fig. 1), possibly due to crystallization from Ca-rich fluids or melts (Brenker et al. 2005, 2021; Walter et al. 2008; Bulanova et al. 2010). The unmixing exhibited in many of the $CaSiO_3$-rich inclusions to breyite-bearing assemblages requires transport of the diamond from the perovskite stability field to shallower depths in the mantle, with suggested mechanisms including mantle convection (e.g., transport in a plume) or with a percolating melt (Davies et al. 2004b; Harte and Cayzer 2007; Walter et al. 2008; Bulanova et al. 2010; Sun et al. 2020).

While exsolution as well as co-occurring minerals indicate an origin as Ca-silicate perovskite for many of the $CaSiO_3$-rich inclusions, it is possible that in some cases inclusions crystallized directly as single phase breyite at upper mantle pressures (e.g., ~ 3 to 9 GPa, Fig. 9a) rather than as Ca-silicate perovskite. It has been suggested that this might occur in Ca-rich lithologies like subducted meta-sediment or through reactions of melts derived from such Ca-rich sediments and peridotitic mantle (Brenker et al. 2005, 2021; Woodland et al. 2020). It is noteworthy that merwinite ($Ca_3MgSi_2O_8$) has been recognized as an inclusion co-occurring with low-Ti $CaSiO_3$ in two cases, suggestive of a Ca-rich association. We also note a few Ca-rich inclusions have a Ca/Si ratio greater than unity in composite assemblages of breyite + larnite (Brenker et al. 2005, 2021; Smith et al. 2018), although no bulk compositions have been reported and these are not part of our data compilation. It is currently unclear whether these composite inclusions represent a Ca-rich silicate phase formed in a unique lithology, or they contain a mass-balancing $CaSi_2O_5$-titanite phase that has gone undetected, or whether such inclusions might represent a trapped melt phase.

Perovskite-structured $CaSiO_3$ inclusions. Two studies present evidence for $CaSiO_3$-rich inclusions retaining a perovskite structure, both concluding petrogenesis within the lower mantle and preservation to the surface. Nestola et al. (2018) combined Raman, X-ray diffraction and EBSD on a composite $CaSiO_3$ + $CaTiO_3$ inclusion from South Africa (Cullinan) and interpreted the $CaSiO_3$ portion of the inclusion to be in an orthorhombic perovskite structure (Fig. 7h). However, this interpretation cannot be reconciled with the phase relations in Figure 9b, as there is no stability field where $CaTiO_3$-perovskite and $CaSiO_3$-perovskite coexist; experiments demonstrate a complete solid solution between these phases and unmixing should yield $CaTiO_3$ perovskite + breyite or wollastonite. Given the proximity of both $CaSiO_3$ and $CaTiO_3$ regions in the inclusions (Fig. 7h) and their very similar Raman spectra, as well as the large uncertainty in unit cell volume from the X-ray diffraction data, this interpretation requires further evaluation.

Tschauner et al. (2021) presented evidence from X-ray diffraction coupled with compositional information derived from a bulk LA-ICP-MS analysis (diamond plus inclusions) to argue that the core of a coated diamond from Botswana (GRR-1507) contains inclusions of an unusual alkali and chrome-rich variety of $CaSiO_3$ in the cubic perovskite structure. The data presented for both the diamond and the inclusion are more easily reconciled with an origin in cratonic lithospheric mantle. The high N content and poorly aggregated N of the diamond core are inconsistent with an origin at temperatures of the convecting mantle but are consistent with storage at lithospheric temperatures. X-ray diffraction data are not unique and can be well matched to phases common in micro-inclusion-bearing lithospheric diamonds. The calculated (not directly measured) bulk inclusion composition is too imprecise to confirm a phase with $CaSiO_3$ stoichiometry. Most notably, the remarkably high K, Na and Cr contents of the calculated inclusion are unlike any known $CaSiO_3$-rich inclusions in our data set, greater by factors of the order 10× (Fig. 8, Table 4—Available at: https://doi.org/10.5683/SP3/LIVK1K), but are similar to micro-inclusions found in the same suite of samples and other coated lithospheric diamonds (Navon et al. 1988; Weiss et al. 2014).

Both of these results require further evaluation, but we suggest the geological implausibility of recovering a sample of perovskite-structured $CaSiO_3$ at Earth's surface that originated in the transition zone or lower mantle. Experiments indicate that lower pressure polymorphs of $CaSiO_3$ (e.g., breyite or wollastonite) equilibrate in experiments in a matter of minutes to hours at 1200 °C (Kubo et al. 1997; Sueda et al. 2006), and these minerals are commonly observed in our $CaSiO_3$-rich inclusion database both as mono-crystalline phases and as unmixed components of composite inclusions (Fig. 7; Table 4—Available at: https://doi.org/10.5683/SP3/LIVK1K). Further, no experimentally synthesized perovskite-structured $CaSiO_3$ phase has ever been recovered from high pressure to 1 atmosphere conditions to our knowledge, converting instead to an amorphous phase upon decompression (Mao et al. 1989; Wang and Weidner 1994; Thomson et al. 2019). More work is needed to better evaluate potential *P–T* paths that may permit a stable perovskite-structured phase to be retained to the surface, but currently the data presented in these studies do not, in our view, support the interpretation of stable perovskite-structured $CaSiO_3$-rich phases as inclusions in diamonds.

Trace element compositions

Trace elements have been analyzed in twenty of the $CaSiO_3$-rich inclusions, eleven from the low-Ti group and nine from the high-Ti group. These data are provided in Table 5 (Available at: https://doi.org/10.5683/SP3/LIVK1K) and plotted as spidergrams on Figure 10, normalized to BSE. Eighteen of the twenty inclusions were measured by SIMS at the Edinburgh Ion Probe Facility (EIMF) and two by LA-ICP-MS. Also shown on these diagrams are the calculated abundance patterns for Ca-silicate perovskite in equilibrium with assemblages predicted for meta-peridotite and meta-basalt (MORB) at transition zone and lower mantle conditions.

Low-Ti $CaSiO_3$ inclusions. Figure 10a shows trace element abundances for the low-Ti inclusions. The inclusions are enriched relative to BSE in most trace elements by up to more than two orders of magnitude. Most trace elements are also enriched by up to an order of magnitude relative to models for the trace element abundances expected for sub-solidus Ca-silicate perovskite in meta-peridotitic or meta-harzburgitic assemblages in either the lower mantle or deep transition zone. They are most akin to Ca-silicate perovskite in either MORB or processed MORB, but this is not consistent with their low Ti contents (Fig. 8). Many of the inclusions have relative depletions in Rb, Ba, Sr, Zr, Hf, Nb, Ta and Y and enrichments in light REE relative to heavy REE. It is noteworthy that the least enriched inclusion could be consistent with an origin in a meta-peridotitic lower mantle assemblage, and this inclusion, from Machado River in Brazil (Burnham et al. 2016), is also the only inclusion in the entire dataset with an MgO content plausibly consistent with equilibration with bridgmanite at lower mantle temperatures. Thus, the low-Ti inclusions have a meta-peridotitic major element affinity but are generally enriched in incompatible trace elements.

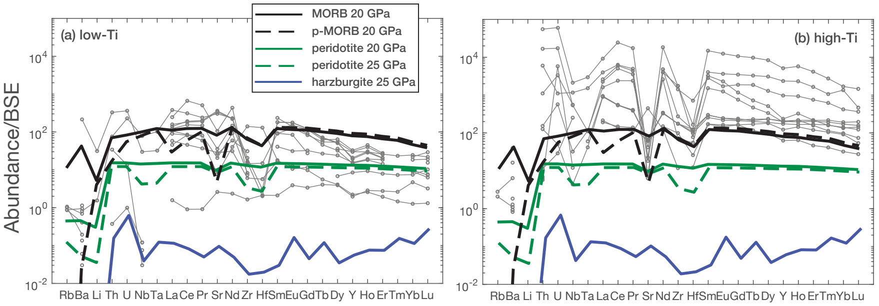

Figure 10. Trace element abundances in $CaSiO_3$-rich inclusions from the global dataset normalized to BSE: **(a)** low-Ti inclusions, and **(b)** high-Ti inclusions. Also shown are calculated abundance patterns for Ca-silicate perovskite expected in meta-peridotitic, meta-harzburgitic, and meta-basaltic (MORB and processed MORB) mineral assemblages in the transition zone and lower mantle; meta-basalt (MORB/p-MORB) at 20 GPa = Ca-silicate perovskite + majoritic garnet + ringwoodite; meta-peridotite at 20 GPa = Ca-silicate perovskite + majoritic garnet + ringwoodite; meta-peridotite/harzburgite at 25 GPa = Ca-silicate perovskite + bridgmanite + ferropericlase. Mineral modes and partition coefficients are provided in Table 3.

High-Ti $CaSiO_3$ inclusions. Figure 10b shows trace element abundances for the high-Ti inclusions. A distinguishing feature of these inclusions is their extremely elevated trace element abundances relative to BSE. For example, the most enriched inclusions have 1000 to 70,000 × BSE in incompatible elements like Th, U and the light REE. The inclusions also exhibit a large negative Sr anomaly in all but one inclusion and are characterized by relative depletions in Hf, Zr, Nb and Ta, and also Rb and Ba when measured (these elements were below detection levels in several inclusions).

The trace element abundances in the inclusions are not consistent with subsolidus Ca-silicate perovskite in either meta-peridotitic or meta-basaltic mineral assemblages in the upper to lower mantle. Abundances in the least enriched inclusions overlap with modeled Ca-silicate perovskite in MORB or processed MORB but have much more pronounced Sr and HFSE anomalies. Most inclusions are significantly enriched relative to expectations for MORB, by up to more than two orders of magnitude for many elements (Wang et al. 2000a; Walter et al. 2008; Bulanova et al. 2010; Thomson et al. 2016b). Models for the overall enrichments in trace elements and the characteristics of the abundance patterns in $CaSiO_3$ inclusions are generally consistent with equilibration involving low-degree melts, likely derived from meta-basaltic assemblages, as described further in the '*Discussion*' section.

$MgSiO_3$-RICH INCLUSIONS

The compilation of $MgSiO_3$-rich phases with ABO_3 stoichiometry includes fifty-five inclusions in diamonds from six cratons, forty-two of which are from South America (Table 6—Available at: https://doi.org/10.5683/SP3/LIVK1K). Both single phase and composite (Fig. 11) inclusions have been reported. Thirty-five of the inclusions occur in diamonds with assemblages that include ferropericlase and four co-occur with $CaSiO_3$-rich phases. There are three co-occurrences with both ferropericlase and $CaSiO_3$ in the same diamond. The co-occurrence of $MgSiO_3$-rich phases with ferropericlase and/or $CaSiO_3$-rich phases has provided the basis for the interpretation of a meta-peridotitic, lower mantle association for these inclusion assemblages (Harte et al. 1999; Stachel et al. 2000b; Hutchison et al. 2001; Kaminsky et al. 2001; Davies et al. 2004b; Hayman et al. 2005; Harte 2010; Burnham et al. 2016). No $MgSiO_3$-rich inclusions have been found with a bridgmanite crystal structure, and it has been commonly assumed that the observed enstatite structured $MgSiO_3$ inclusions, identified on the basis of X-ray diffraction and Raman spectroscopy (Hutchison et al. 2001; Walter et al. 2011; Thomson et al. 2014; Burnham et al. 2016), represent retrogression from bridgmanite.

Minerals observed together with $MgSiO_3$ in composite inclusions and interpreted as exsolved phases during retrogression include olivine, ferropericlase, jeffbenite (formerly known as TAPP, ideally $Mg_3Al_2Si_3O_{12}$), ilmenite, magnetite, spinel and magnesian ulvöspinel (Fig. 11) (Harte et al. 1999; Stachel et al. 2000b; Hutchison et al. 2001; Kaminsky et al. 2001; Hayman et al. 2005; Walter et al. 2011; Thomson et al. 2014; Zedgenizov et al. 2014a). Other phases co-occurring with $MgSiO_3$-rich phases in the same diamond include clinopyroxene, olivine, carbonate and Ni-rich metal. We note that eight jeffbenite inclusions have been included in our $MgSiO_3$-rich inclusion compilation.

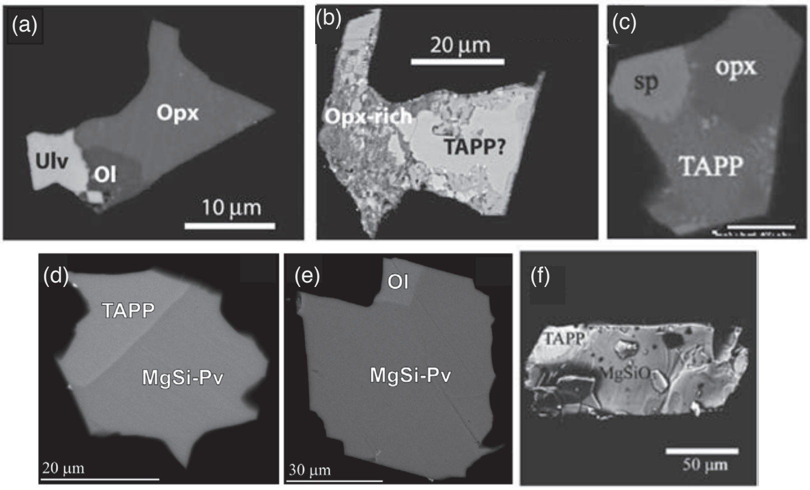

Figure 11. Backscattered electron images of composite $MgSiO_3$-rich inclusions from previous studies: (**a–b**) From Walter et al. (2011). Reprinted with permission from AAAS; (**c**) CC BY Thomson et al. (2014a); (**d–e**) Reprinted from Zedgenizov et al. (2014a) Copyright (2014), with permission from Elsevier; (**f**) Reprinted by permission from Springer Nature Customer Service Centre GmbH: Springer Nature. Hayman et al. (2005), Copyright 2005. Opx = orthopyroxene; Ol = olivine; Ulv = ulvöspinel; TAPP = jeffbenite; sp = spinel; MgSi-Pv = $MgSiO_3$-phase.

Major element compositions

Published major element compositions of the $MgSiO_3$-rich inclusions as determined by electron microprobe are provided in Table 6 (Available at: https://doi.org/10.5683/SP3/LIVK1K). The inclusions are separated into two distinctive groups on the basis of a gap in their alumina contents: a ***low-Al*** group with $Al_2O_3 < 3.5$ wt% and a ***high-Al*** group with $Al_2O_3 > 7$ wt%.

The *low-Al* group comprises thirty-four $MgSiO_3$-rich inclusions, twenty-four of which are reported as single-phase inclusions and a further ten are composite and contain minor exsolved phases that include olivine, ferropericlase and jeffbenite. The EPMA analyses of the composite inclusions, to the best of our knowledge, do not include exsolved phases but represent the $MgSiO_3$-rich portion of the inclusion. The exceptions are two composite inclusions reported by Burnham et al. (2016) where bulk inclusion compositions are reported by recombination of observed phases. Twenty-seven of the low-Al inclusions co-occur with ferropericlase and four with ferropericlase and $CaSiO_3$-rich phases.

The *high-Al* group comprises twenty-one inclusions, all from South America. Seven of these are single-phase inclusions and six are composite inclusions (Fig. 11) containing enstatite ± jeffbenite/olivine/spinel-ulvöspinel/magnetite/SiO_2. The bulk compositions of four of the six composite inclusions were estimated either through broad beam or multiple analyses of entire inclusions or by combining spot analyses of individual phases on the basis of their mode estimated from image analysis (Walter et al. 2011; Thomson et al. 2014). The remaining eight inclusions in this group are jeffbenite.

Armstrong et al (2012) noted the similarity of jeffbenite inclusions to high-Al bridgmanite produced in experiments on basaltic starting compositions and speculated on this basis that jeffbenite could represent retrograde aluminous bridgmanite. These authors also located a low-pressure stability field for jeffbenite at < 10 GPa that is consistent with its formation as a lower-pressure phase. Three high-alumina, single phase inclusions co-occur with ferropericlase inclusions, as does one of the Na-rich inclusions and five of the jeffbenite inclusions.

Figure 12 shows $MgSiO_3$-rich inclusions plotted in the compositional ternary diagram $(Mg+Fe^{2+})-(Si+Ti)-(Al+Cr+Fe^{3+})$. The *low-Al* inclusions plot in a well-defined region that partially overlaps the field of experimental bridgmanites synthesized in meta-peridotitic assemblages. However, most experimental bridgmanites made using primitive mantle compositions have higher trivalent cations than the inclusions. Many *low-Al* inclusions have similarity with bridgmanite produced in experiments using harzburgitic bulk compositions, and also overlap with akimotoite synthesized in peridotitic bulk compositions; akimotoite is an ilmenite-structured $MgSiO_3$-rich phase that is stable over a limited pressure-temperature range in meta-peridotite near the base of the transition zone (Fig. 16; Stixrude and Lithgow-Bertelloni 2011).

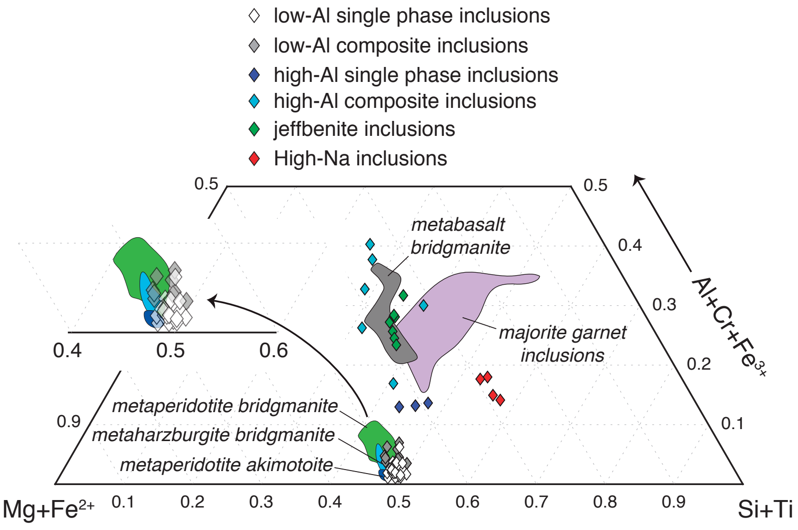

Figure 12. Projection of $MgSiO_3$-rich inclusion compositions (Table 6) into the pseudo-ternary $(Mg+Fe^{2+})$-$(Si+Ti)$-$(Al+Cr+Fe^{3+})$. Iron is treated as a 50:50 mixture of Fe^{2+} and Fe^{3+} for plotting purposes based on the established proclivity for bridgmanite to accommodate ferric iron (McCammon et al. 1997; McCammon et al. 2004). Inclusions types are separated as follows: **white diamonds**, low-Al single phase inclusions; **grey diamonds**, low-Al composite inclusions; **blue diamonds**, high-Al single phase inclusions (Type-II of Hutchison et al. 2001); **cyan diamonds**, high-Al composite inclusions; **green diamonds**, jeffbenite inclusions; **red diamonds**, high-Na (Type III of Hutchison et al. 2001). Fields are also shown for experimental bridgmanite and akimotoite produced in meta-basaltic, meta-peridotitic and meta-harzburgitic assemblages at pressures from 23 to 47 GPa (Irifune and Ringwood 1987; Irifune et al. 1994, 2010; Wood 2000; Ono et al. 2001; Hirose 2002; Hirose and Fei 2002; Tronnes and Frost 2002; Nishiyama and Yagi 2003; Nishiyama et al. 2004; Walter et al. 2004; Litasov and Ohtani 2005; Ishii et al. 2011, 2018, 2019). Also shown is the field of majoritic garnet inclusions, this study.

In contrast, the *high-Al* inclusions show considerable compositional variation, with Figure 12 showing that the six composite inclusions (cyan diamonds) and the jeffbenite inclusions (green diamonds) are generally similar to bridgmanite produced in meta-basalt on this projection, whereas the three single phase inclusions (blue diamonds; Type II $MgSiO_3$ inclusions of Hutchison et al. 2021) plot between experimental meta-peridotitic and meta-basaltic bridgmanites. The four Na-rich (~4–6 wt% Na_2O) inclusions (red diamonds; Type III $MgSiO_3$ inclusions of Hutchison et al. 2021) are unlike any experimental bridgmanite or other $MgSiO_3$-rich inclusions.

Figure 13 shows the Mg# of $MgSiO_3$-rich inclusions plotted against the Mg# of ferropericlase inclusions that co-occur in the same diamond. Also shown are fields for bridgmanite and ferropericlase equilibrated together in experiments on fertile peridotite bulk compositions and in a harzburgite composition. Ferropericlase with Mg#s less than ~0.8 are inconsistent with equilibration with co-occurring bridgmanite in meta-peridotitic or meta-harzburgitic assemblages. In diamonds hosting ferropericlase with Mg#s greater than 0.8, it is striking that very few of the inclusion pairs plot within the field of fertile meta-peridotite. Many of the *low-Al* bridgmanite-ferropericlase inclusion pairs overlap with or plot close to the field of meta-harzburgite, with $MgSiO_3$-rich inclusions tending to have very high Mg#s. Three single-phase high-Al $MgSiO_3$-ferropericalse pairs and two jeffbenite-ferropericlase pairs plot just within or close to the experimental meta-peridotite field.

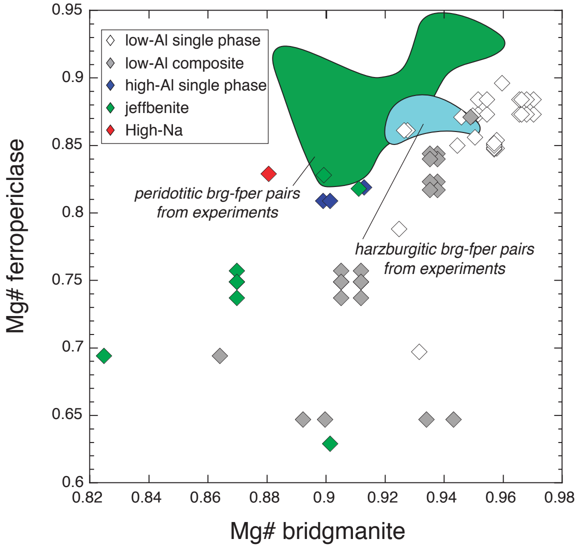

Figure 13. Mg# of $MgSiO_3$-rich inclusions versus the Mg# of co-occurring (same diamond) ferropericlase inclusions (all iron calculated as divalent). The fields show bridgmanite and ferropericlase compositions from experiments on fertile primitive peridotite compositions (**green field**) (Irifune 1994; Wood 2000; Hirose 2002; Tronnes and Frost 2002; Nishiyama and Yagi 2003; Walter et al. 2004; Ishii et al. 2011, 2018; Kuwahara et al. 2018) and harzburgite composition (**cyan field**) (Ishii et al. 2019), where bridgmanite coexists with ferropericlase ± Ca-silicate perovskite.

Low-Al inclusions. Figure 14 shows NiO, Al_2O_3 and CaO versus Mg# for $MgSiO_3$-rich inclusions (diamonds) compared with bridgmanite synthesized in experiments on peridotitic bulk compositions. The low-Al inclusions (white diamonds) occur over a range of Mg# from ~ 0.86 to 0.97, most concentrated between 0.92 and 0.97. Comparatively, bridgmanites observed in primitive meta-peridotitic assemblages have bulk compositions with lower Mg#s

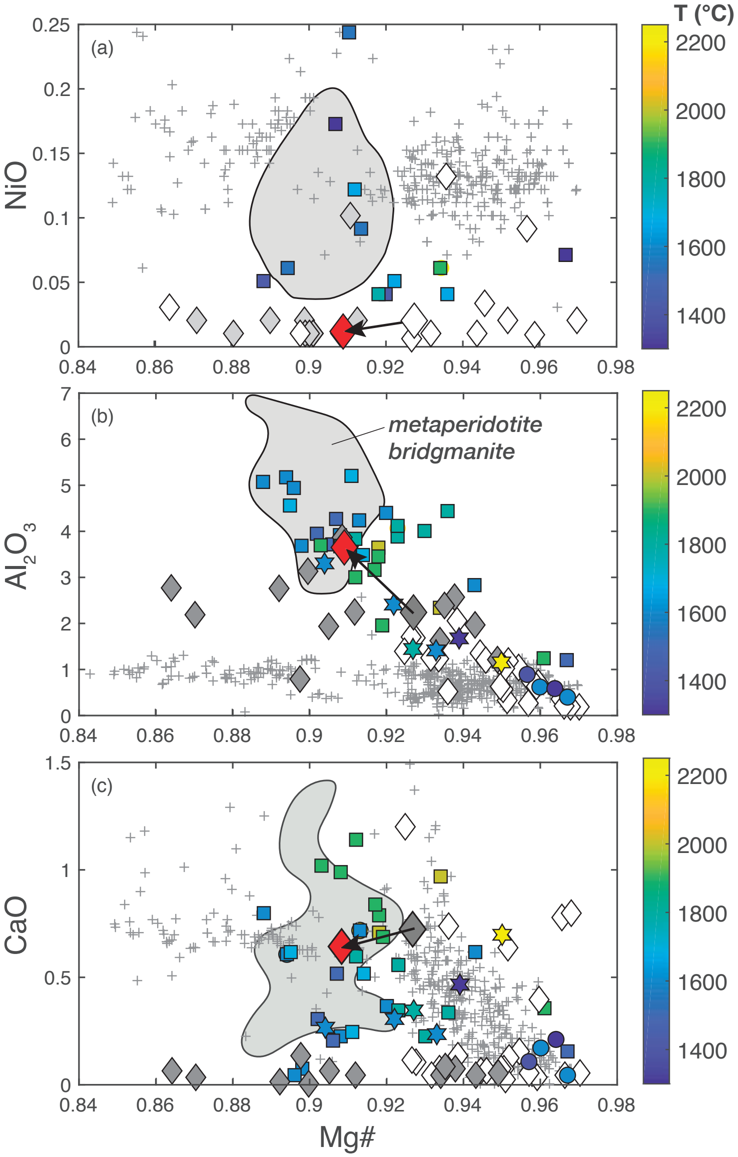

Figure 14. NiO **(a)**, Al_2O_3 **(b)** and CaO **(c)** versus Mg# showing $MgSiO_3$-rich inclusions: **white diamonds**, low-Al single phase inclusions; **light grey diamonds** in (a) are high-Al inclusions. In (b) and (c) **dark grey diamonds are** low-Al composite inclusions; **red diamond**, re-constructed low-Al, high Ca inclusion from Burnham et al. (2016), connected to the measured $MgSiO_3$ portion of the inclusion by an arrow. Experimental bridgmanites coexisting with ferropericlase ± Ca-silicate perovskite in meta-peridotitic assemblages are shown as a **light grey field** (Ito and Takahashi 1987; Irifune 1994; Wood 2000; Hirose 2002; Tronnes and Frost 2002; Nishiyama and Yagi 2003; Nishiyama et al. 2004; Walter et al. 2004; Irifune et al. 2010; Ishii et al. 2011, 2018, 2019; Kuwahara et al. 2018); **squares**, bridgmanite in experiments on meta-peridotite coexisting with majorite ± ferropericlase / Ca-silicate perovskite / ringwoodite; **circles**, akimotoite in experiments on meta-peridotitic compositions coexisting with majorite ± Ca-silicate perovskite/ringwoodite/stishovite; **six pointed stars**, bridgmanite in experiments on harzburgite composition; **crosses**, orthopyroxene inclusions in lithospheric diamonds (see Stachel et al. 2022 for references). Experiments denoted by **symbols** are shaded for experimental temperature.

that concentrate between 0.88 and 0.92, with some extending as high as 0.97. The NiO contents of the $MgSiO_3$-rich inclusions are low, generally less than 0.05 wt%; only in a few exceptions do inclusions possess values exceeding 0.1 wt%.

NiO contents of the $MgSiO_3$-rich inclusions are low relative to enstatite inclusions in lithospheric diamonds (gray crosses in Fig. 14a), which has been used as evidence to support an origin in the lower mantle because Ni is expected to partition strongly into coexisting ferropericlase (Harte et al. 1999; Stachel et al. 2000b). However, Figure 14a shows that experimental bridgmanite in equilibrium with ferropericlase in experiments at pressures between 23 and 43 GPa and over a range of high temperatures have NiO contents distinctly higher than the majority of the inclusions, ranging from about 0.05 to 0.25 wt%. This implies that equilibration with ferropericlase in a primitive mantle composition does not account for the low Ni contents of most inclusions.

Figures 14b and 14c show that like NiO, the Al_2O_3 and CaO contents of $MgSiO_3$-rich inclusions are generally lower than in experimental peridotitic bridgmanite compositions. The Al_2O_3 contents of the inclusions show a negative correlation with Mg#, ranging from about 3 to 0.2 wt% at Mg#s between 0.92 and 0.97. In composite low-Al inclusions the $MgSiO_3$ portions with Mg#s less than 0.92 are higher in Al_2O_3 (~ 3 wt%) than in single phase low-Al inclusions. Experimental bridgmanites in equilibrium with a lower mantle assemblage of ferropericlase ± Ca-silicate perovskite range from ~3 to 7 wt% Al_2O_3 and are unlike the inclusion compositions. Experimental bridgmanites in equilibrium with a deep transition zone assemblage of majoritic garnet ± Ca-silicate perovskite/ringwoodite/ferropericlase are shown as squares on Figure 14. A few of these experimental bridgmanites trend to very low Al_2O_3 and high Mg#, and we note that two experimental bridgmanites with ~1 wt% Al_2O_3 occur in majoritic garnet + ringwoodite-bearing (±Ca-silicate perovskite/ferropericlase) assemblages at ~ 23 GPa.

Also intriguing are the compositions of akimotoite in four experiments coexisting with majoritic garnet ± ringwoodite/Ca-silicate perovskite/stishovite (circles on Fig. 14), providing an alternative interpretation for original polymorph of some $MgSiO_3$-rich inclusions. Notably, bridgmanite formed in experiments on depleted harzburgite (hex-stars) can also have similarly low Al_2O_3 contents and high Mg#s that overlap with many of the low-Al inclusions. We note that while there is overlap with the Al_2O_3 contents of enstatite inclusions from lithospheric diamonds at high Mg#s, overall, the $MgSiO_3$-rich inclusions are distinct from lithospheric enstatites.

CaO contents in experimental bridgmanites in equilibrium with ferropericlase ±Ca-silicate perovskite assemblages (Fig. 14c) are also notably higher than most of the observed inclusions. Bridgmanites in several majorite-bearing experiments at lower temperatures have similarly low CaO contents, and as observed with Al_2O_3, experimental akimotoites have CaO contents similar to the inclusions as do bridgmanites in meta-harzburgite assemblages. Like Al_2O_3, there is overlap with the CaO contents of enstatite inclusions from lithospheric diamonds at high Mg#s but, overall, the $MgSiO_3$-rich inclusions have lower CaO and are distinct from lithospheric enstatite inclusions. An exception is a low-Al inclusion with high NiO that is akin to lithospheric inclusions from Eurelia (Australia) but co-occurs with ferropericlase (Tappert et al. 2009b).

Four of the low-Al inclusions that have high CaO (> 0.5 wt%) are from the Machado River deposit in Brazil as reported in the study of Burnham et al. (2016). Three of these inclusions have low NiO (<0.05 wt%) and low Al_2O_3 (<0.5 wt%), while the fourth composite inclusion has ~3.8 wt% Al_2O_3. All four of these inclusions co-occur with high Mg# ferropericlase that could be in equilibrium with bridgmanite. It is noteworthy that a $CaSiO_3$-inclusion from the Machado locality is also the only such inclusion with an MgO content consistent with an origin in primitive mantle peridotite. Burnham also reports a reconstructed $MgSiO_3$-rich inclusion that is shown as a red diamond on Figure 14. This inclusion, like other low-Al composite inclusions, has an exsolved aluminous phase with a jeffbenite composition. Reconstruction of the bulk composition results in slightly lower NiO and CaO but higher Al_2O_3. We expect that other low-Al composite inclusions may also require such corrections. This would imply that alumina contents in some cases may be underestimated, possibly reflected in the nearly constant alumina content of the low-Al composite inclusions irrespective of Mg#.

High-Al inclusions. Figure 15 shows TiO_2, Na_2O, CaO and Al_2O_3 versus Mg# for *high-Al* $MgSiO_3$-rich inclusions compared with bridgmanites synthesized in experiments on basaltic bulk compositions. The six composite inclusions and one of the jeffbenite inclusions, all from the Juina region of Brazil, have low Mg#s (~0.43–0.65) consistent with experimental bridgmanites formed in meta-basaltic assemblages (Walter et al. 2011; Armstrong and Walter 2012; Pla Cid et al. 2014; Thomson et al. 2014). The composite inclusions include high-Ti and high-Al contents, although the two inclusions reported by Pla Cid et al. (2014) are notable in their low TiO_2. The Ca-contents of all the composite inclusions are lower than observed in experimental high-Al bridgmanite phases.

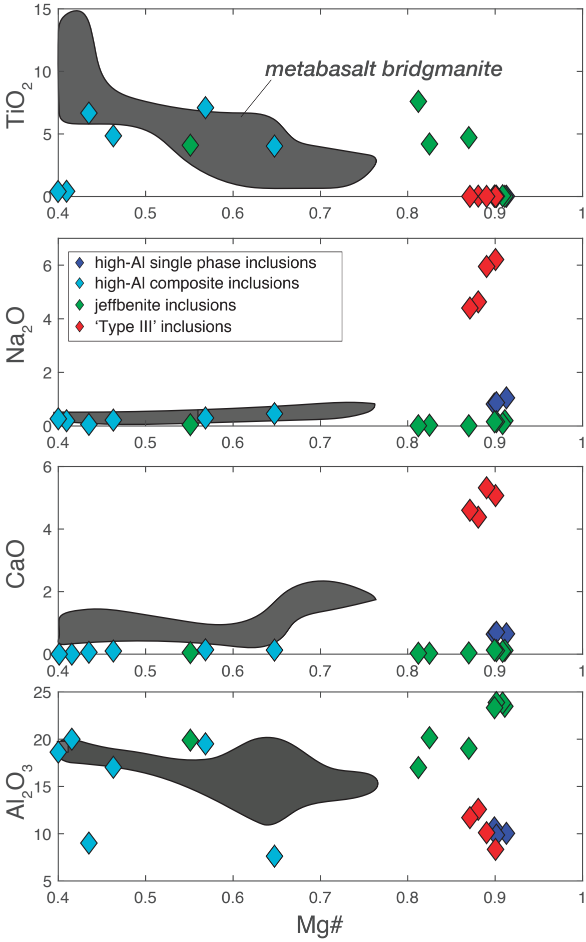

Figure 15. TiO_2 **(a)**, Na_2O **(b)**, CaO **(c)** and Al_2O_3 **(d)** versus Mg# showing high-Al $MgSiO_3$-rich inclusions: **blue diamonds**, low-Al single phase inclusions; **cyan diamonds** high-Al composite inclusions; **green diamonds**, jeffbenite inclusions; **red** diamonds, Type III inclusions of Hutchison et al. (2001); **dark grey field**, experimental high-Al bridgmanite in meta-basaltic assemblages ± majorite / Ca-silicate perovskite / CF phase / NAL phase / stishovite (Ono et al. 2001; Hirose and Fei 2002; Litasov and Ohtani 2005; Kuwahara et al. 2018).

The remaining fourteen high-alumina inclusions have Mg#s that are much higher than experimental bridgmanites in meta-basaltic assemblages and are more akin to those in meta-peridotitic assemblages. The seven high-Mg# jeffbenite inclusions have very high Al_2O_3, coupled with very low CaO and Na_2O, and several of these coexist with iron-rich ferropericlase (Mg#<0.8, Fig. 13). The TiO_2 contents of these inclusions vary, with TiO_2 present either as a minor component (< 0.1 wt%) or a major element (~ 4–8 wt%). Thus, the high Mg# jeffbenite inclusions, while having some features consistent with bridgmanite, appear to be unique relative to bridgmanite formed in either meta-peridotitic or meta-basaltic assemblages.

The three high-Al single phase inclusions ("Type II" inclusions of Hutchison et al, 2001) have alumina contents that are distinctly higher (~ 10 wt% Al_2O_3) than produced in experiments on primitive peridotite (<7 wt% Al_2O_3), but also have low CaO. These inclusions co-occur with ferropericlase with Mg#s of 0.81 to 0.82, nominally consistent with expectations from experiments on peridotite compositions (Fig. 13). The four "Type III" inclusions of Hutchison et al (2001) are unique in their very high Na_2O and CaO contents. None of these high Mg#, high-Al, high-Na inclusions are consistent with any experimental bridgmanites in the literature and may represent a unique association. On the basis of experiments on the inclusion bulk compositions, Hutchison et al. (2001) interpreted these to have a unique origin at pressures corresponding to the lower transition zone, albeit at temperatures several hundred degrees higher than the mantle geotherm.

Phase relations. Figure 16 shows calculated phase relations in the system $MgSiO_3$–Al_2O_3 with pressure at 1600 °C (Fig. 16a), and for a pyrolite (fertile peridotite) composition (Fig. 16b) at pressures and temperatures of the deep upper mantle and shallow lower mantle (Stixrude and Lithgow-Bertelloni 2011).

The alumina content in bridgmanite is a potential barometer, and Figure 16a shows the Al_2O_3 contents (mole fraction) in the low-Al and high-Al inclusions for comparison with phase relations in this simplified system. If the low-Al $MgSiO_3$-inclusions are former bridgmanite then phase relations either indicate a pressure of origin of ~ 22.5 to 26 GPa if the inclusions equilibrated with majoritic garnet, or formation at unconstrained higher pressures if they did not because alumina becomes increasingly soluble in bridgmanite at higher pressures. Because none of the low-Al inclusions are reported to co-occur with majoritic garnet, their low-Al contents likely indicate formation involving a low-alumina protolith (e.g., harzburgite) as suggested by their high Mg#s and depletion in CaO. We note that low-Al $MgSiO_3$-rich inclusions have Al_2O_3-contents that are also generally consistent with that expected for akimotoite at ~ 20 to 22.5 GPa.

The high-Al single phase inclusions have alumina contents consistent with a pressure of about 27 GPa if they co-existed with corundum, and we note that two of the three inclusions co-occur with ruby (corundum) in addition to relatively Mg-rich ferropericlase (Harte et al. 1999), suggesting that these inclusions may have originated in an alumina-rich, peridotitic protolith at the top of the lower mantle. The high-Al composite inclusions indicate pressures of ~27 to 34 GPa if they formed in equilibrium with corundum (none co-occur with ruby) but these are minimum pressure if they did not. If the jeffbenite inclusions were former bridgmanite then their alumina contents indicate minimum pressures of ~32 to 34 GPa but, again, none of these inclusions co-occur with ruby. It is noteworthy that the few low-Al $MgSiO_3$ inclusions and jeffbenite inclusions that have been analyzed for ferric iron have elevated $Fe^{3+}/\sum Fe$ that is generally compatible with expectations for bridgmanite in the shallow lower mantle (McCammon et al. 1997, 2004).

Phase relations for a pyrolytic composition are shown relative to ambient mantle and slab geotherms in Figure 16b. Along an ambient mantle geotherm, bridgmanite forms at about 24 GPa and coexists with majoritic garnet, Ca-silicate perovskite and ferropericlase, and there is only a very small akimotoite stability field. The akimotoite field expands at lower

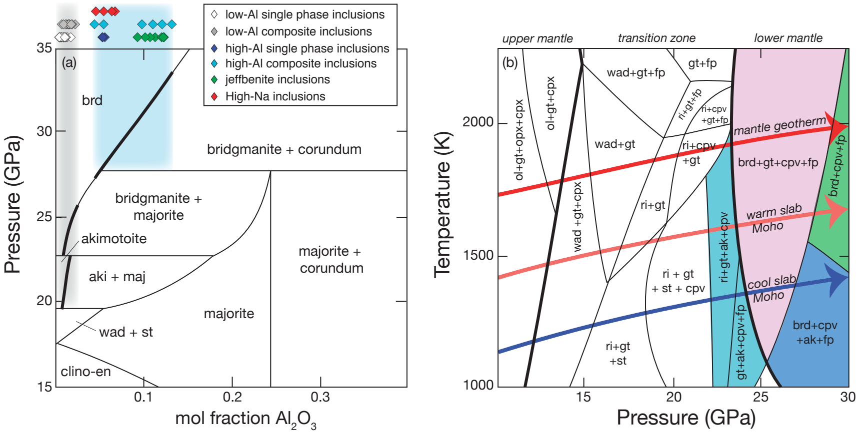

Figure 16. (a) Phase relations in the system $MgSiO_3$-Al_2O_3 (mole fraction Al/(Al+Mg)) as a function of pressure at 1600 °C (Stixrude and Lithgow-Bertelloni 2011). Also shown are the alumina contents of the $MgSiO_3$-rich inclusions (see symbol key). The **grey bar** shows the range of Al-content in low-Al inclusions and the **blue bar** the range in high-Al inclusions. **(b)** Phase relations for 'pyrolitic' mantle (Stixrude and Lithgow-Bertelloni 2011). The **cyan region** shows akimotoite + majoritic garnet stability, the **purple shaded region** shows bridgmanite + majoritic garnet stability, the **dark blue region** shows bridgmanite + akimotoite stability, and the **green region** bridgmanite stability. Also shown are model geotherms for the mantle (Katsura et al. 2010) and warm and cool slabs at the Moho (Shirey et al. 2021) (deflections at phase boundaries omitted). Phase labels are: ak = akimotoite; brd = bridgmanite; cpx = clinopyroxene; cpv = Ca-silicate perovskite; fp = ferropericlase; gt = garnet; ol = olivine; opx = orthopyroxene; ri = ringwoodite; st = stishovite; wad = wadsleyite.

temperatures such that along a warm or cold slab Moho geotherm akimotoite is stabilized over an ~2 GPa pressure interval at the base of the transition zone (Ishii et al. 2011). Whether or not the low-Al $MgSiO_3$-rich inclusions represent bridgmanite or in some cases akimotoite remains an open question. However, we re-iterate that the low CaO contents are not consistent with bridgmanite in fertile mantle peridotite at temperatures of the mantle geotherm but could be produced either at lower temperatures (Irifune et al. 2000) or in a depleted harzburgitic lithology, or both, which is also consistent with their low Al_2O_3 and high Mg#s and plausibly places their origin in subducted depleted lithospheric mantle along a cool mantle geotherm.

Trace element compositions

Trace elements have been analyzed in twenty-two of the $MgSiO_3$-rich inclusions; ten low-Al inclusions, six high-Al inclusions and six jeffbenite inclusions. Data are provided in Table 7 (Available at: https://doi.org/10.5683/SP3/LIVK1K) and plotted as spidergrams on Figure 17, normalized to BSE. All inclusions were measured by SIMS at EIMF (Harte et al. 1999; Stachel et al. 2000b; Bulanova et al. 2010; Burnham et al. 2016; Thomson et al. 2016b). Also shown on Figure 17b are the calculated abundance patterns for bridgmanite in equilibrium with assemblages predicted for meta-peridotite and meta-basalt (MORB) at transition zone and lower mantle conditions.

The low-Al inclusions have lithophile trace element abundances that, overall, are depleted or similar to BSE. Patterns exhibit notable depletions in Ba, Sr and Y relative to the generally flat REE (Fig. 17a). The two high-Al, single-phase inclusions have similar patterns to the low-Al inclusions and are among the most depleted of the inclusions. The high-Al composite inclusions are more enriched overall and exhibit conspicuous enrichments, up to three orders of magnitude relative to BSE, in Nb, Ta, Zr and Hf, while also having depletions in Ba, Sr and Y. The jeffbenite inclusions have generally similar abundance patterns to other $MgSiO_3$-rich inclusions, with some resembling closely the low-Al inclusions and others exhibiting similar enrichments in Nb, Ta, Zr and Hf as the composite inclusions. These similarities are suggestive that all the $MgSiO_3$-rich inclusions share a common mineralogical pedigree, with an origin as bridgmanite the commonly held interpretation.

Figure 17b shows modeled abundance patterns for bridgmanite in meta-peridotitic, meta-harzburgitic and meta-basaltic assemblages at shallow lower mantle conditions (25 GPa). Abundance levels of the low-Al and high-Al inclusions are similar to those predicted for bridgmanite in peridotitic mantle. However, depletions in Ba, Sr and Y are not predicted in any models and, if these inclusions are former bridgmanite minerals, this likely reflects a distinct feature of the source lithology or the melts and fluids they may have equilibrated with. However, the relative enrichments in Nb, Ta, Zr and Hf are predicted for bridgmanite in the meta-peridotitic and meta-basaltic models, which reflects the presence of Ca-silicate perovskite in the coexisting assemblage. These patterns emerge as Ca-silicate perovskite partitions most trace elements strongly with the exception of Nb, Ta, Zr and Hf. In contrast, bridgmanite has a predilection for Nb, Ta, Zr and Hf, such that strong relative enrichments in these elements occur in assemblages where both phases coexist. Note that bridgmanite in the meta-harzburgitic assemblage has a relatively flat and depleted pattern. Overall, the abundance patterns of $MgSiO_3$-rich inclusions are consistent with expectations for bridgmanite, and many indicate the control of coexisting Ca-silicate perovskite on trace element abundances.

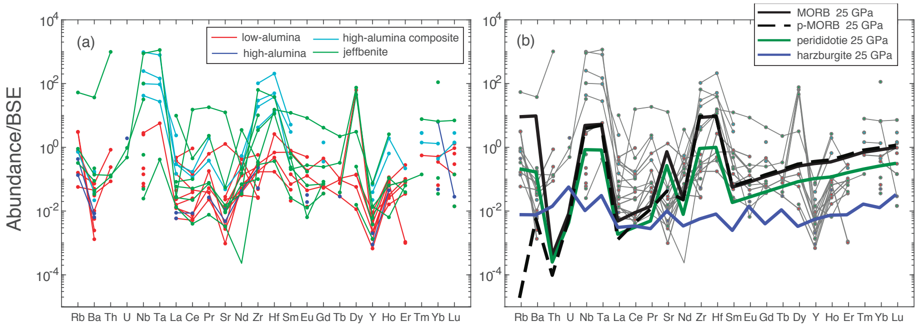

Figure 17. **(a)** Trace element abundances in $MgSiO_3$-rich inclusions from the global dataset normalized to BSE. **(b)** Includes calculated abundance patterns for bridgmanite expected in meta-peridotitic, meta-harzburgitic, meta-basaltic (MORB) and processed meta-basaltic assemblages at lower mantle conditions (25 GPa): MORB-pMORB = Al-bridgmanite + majorite + Ca-silicate perovskite + stishovite; peridotite-harzburgite = bridgmanite + ferropericlase ± Ca-silicate perovskite. Mineral modes and partition coefficients are provided in Table 3.

FERROPERICLASE

Ferropericlase is an oxide mineral with the general formula (Mg,Fe)O, representing a complete solid solution between periclase (MgO) and wüstite (FeO). The term is often used synonymously with magnesiowüstite, but for simplicity we will use ferropericlase in reference to the entire range of solid solution. Ferropericlase has cubic symmetry, crystallizing in the $Fm\bar{3}m$ space group in the B1, or rock salt structure, and is stable throughout the Earth's entire pressure range from crust to the core (Duffy et al. 2015). Ferropericlase is the most common inclusion type in sublithospheric diamonds, and here a literature dataset of 269 inclusions in diamonds collected from five continents has been compiled. More than 60% of the ferropericlase inclusions occur as the only mineral observed in their diamond hosts, often occurring in multiples in a single diamond (we note this observation could be biased by unreported co-occurring phases, especially colorless phases that are difficult to detect).

About a quarter of the reported inclusions co-occur with silicate minerals and about 15% co-occur with $MgSiO_3$-rich and/or $CaSiO_3$-rich phases.

Ferropericlase comprises about 15% by volume of a primitive, peridotitic lower mantle assemblage coexisting with bridgmanite and Ca-silicate perovskite (Fig. 1). In the numerous cases where it occurs as the only inclusion type in a diamond it is commonly used to infer a sublithospheric origin, as ferropericlase is rare as a co-occurring mineral in diamonds that are demonstrably lithospheric (Harte et al. 1999; Stachel et al. 2000b, 2005; Kaminsky et al. 2001; Davies et al. 2004a; Hayman et al. 2005; Zedgenizov et al. 2014a). In the absence of other phases that can potentially provide barometric constraints, the composition of ferropericlase provides no direct information about the depth of diamond and ferropericlase crystallization, which may occur at upper mantle or transition zone conditions and be directly related to diamond forming redox reactions (Stachel and Harris 1997; Brey et al. 2004; Thomson et al. 2016a; Seitz et al. 2018; Bulatov et al. 2019; Nimis et al. 2019). Barometric estimates based on elasticity and elastoplasticity theory can help constrain the depth of origin, for example a recent estimate for two ferropericlase inclusions from a single diamond from Brazil indicate minimum depths of entrapment of ~16 GPa (Anzolini et al. 2019), leaving open the possibility of a transition zone or lower mantle origin.

Major element compositions

Major element compositions based on a literature compilation of electron microprobe analyses of 269 ferropericlase inclusions are provided in Table 8 (Available at: https://doi.org/10.5683/SP3/LIVK1K), with Figure 18 plotting NiO, Al_2O_3, Cr_2O_3 and Na_2O versus Mg#. Also shown are compositions of ferropericlase coexisting with bridgmanite ±Ca-silicate perovskite/garnet/ringwoodite/melt in experiments on primitive peridotitic and harzburgitic bulk compositions at pressures of the deep transition zone and shallow lower mantle.

Ferropericlase inclusions span a wide range of Mg# from about 0.15 to 0.95 (Fig. 18). In comparison, ferropericlase coexisting with lower mantle phases in experiments show a limited range of Mg# from about 0.83 to 0.95, and with NiO contents between about 0.25 and 1.5 wt%. The NiO contents of the ferropericlase inclusions (Fig. 18a) range from near zero at the lowest Mg#s to about 2 wt%, with an apparent positive correlation between NiO and Mg# (Kaminsky et al. 2001; Davies et al. 2004a; Kaminsky 2012; Thomson et al. 2016a). Ferropericlase inclusions that co-occur together with both low-Al and high-Al $MgSiO_3$-rich inclusions are highlighted on Figure 18. These and other ferropericlase inclusions with high Mg#s (> 0.8) have NiO contents that are generally higher or at the extreme high end of the experimental distribution. In contrast, co-occurring $MgSiO_3$-rich inclusions generally have low NiO contents relative to experiments (Fig. 14). The average measured NiO partition coefficient between bridgmanite and ferropericlase ($D^{\mathrm{fp/brg}} = X^{\mathrm{Ni,fp}}/X^{\mathrm{Ni,brg}}$) in experiments where NiO is reported is 16 ± 9, whereas in the co-occurring inclusions it is 86 ± 56. Thus, as with Mg# (Fig. 13), co-occurring bridgmanite-ferropericlase pairs are not consistent with those produced in experiments on primitive mantle peridotite. As discussed above, the Mg#s of these bridgmanite–ferropericlase pairs do not match those from primitive mantle peridotite but are more akin to those expected in depleted meta-harzburgite assemblages.

Figure 18b–d show that the Cr_2O_3, Al_2O_3 and Na_2O contents of most ferropericlase inclusions are on the low side or lower than ferropericlase compositions produced in experiments on primitive mantle peridotite and these elements exhibit no apparent correlation with Mg#. The ferropericlase inclusions that co-occur with $MgSiO_3$-rich inclusions are also depleted in these elements. However, we note that the Cr_2O_3, Al_2O_3 and Na_2O contents in high Mg# ferropericlase inclusions overlap with ferropericlase from experiments on harzburgite composition. This depletion in high Mg# ferropericlase is consistent with the $MgSiO_3$-rich inclusions they co-occur with, which also have low Al_2O_3 (and CaO) contents relative to

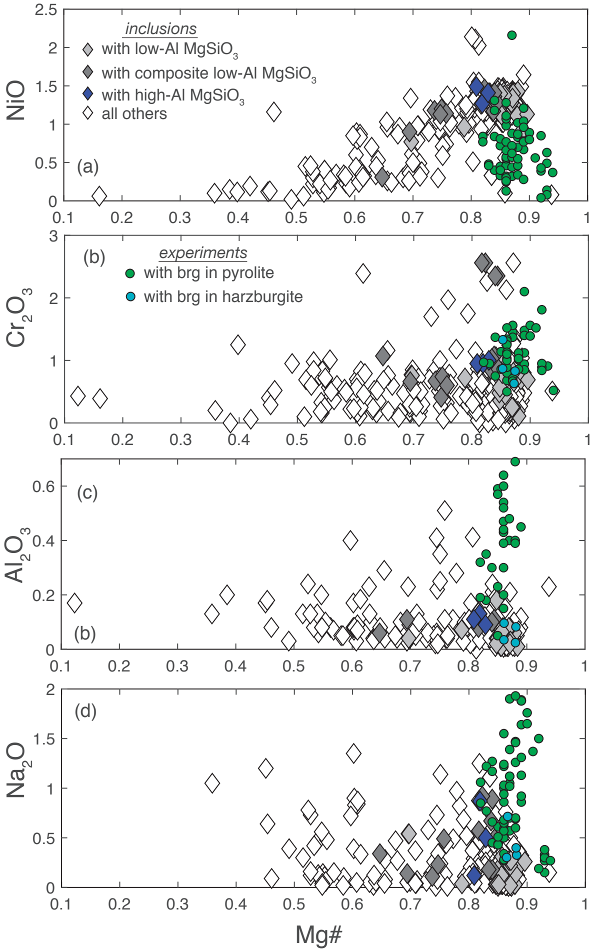

Figure 18. (a) NiO, **(b)** Al_2O_3, **(c)** Cr_2O_3 and **(d)** Na_2O versus Mg# showing ferropericlase inclusions from the global dataset: **white diamonds**, no co-occurring phases reported; **light grey diamonds**, co-occurring with single-phase, low-Al $MgSiO_3$-rich inclusions; **dark grey diamonds**, co-occurring with composite, low-Al $MgSiO_3$-rich inclusions; **blue diamonds**, co-occurring with high-Al $MgSiO_3$-rich inclusions; **green circles,** ferropericlase in experiments on primitive mantle peridotite in equilibrium with bridgmanite ± Ca-silicate perovskite/majorite/ringwoodite (Irifune 1994; Wood 2000; Hirose 2002; Tronnes and Frost 2002; Nishiyama and Yagi 2003; Nishiyama et al. 2004; Walter et al. 2004; Irifune et al. 2010; Ishii et al. 2011, 2018; Kuwahara et al. 2018); **cyan circles,** ferropericlase in experiments on harzburgite in equilibrium with bridgmanite ± majorite/ringwoodite (Ishii et al. 2019).

bridgmanite in meta-peridotite assemblages (Fig. 14). Thus, while more than half of the population of ferropericlase inclusions have Mg#s generally consistent with an origin related to meta-peridotite at lower mantle conditions, most of these have minor element abundances suggesting a relationship to a depleted composition such as harzburgite rather than primitive mantle. The low MgO contents of $CaSiO_3$-rich inclusions and low CaO and Al_2O_3 of $MgSiO_3$-rich inclusions that co-occur with ferropericlase together indicate a low temperature equilibration in depleted peridotite, implicating an association with the harzburgitic portion of cold subducted slab lithosphere.

The ferropericlase inclusions that have Mg#s below ~0.85 trend to low-NiO and Cr_2O_3 contents and have uniformly low Al_2O_3 but highly variable Na_2O contents. These low Mg# ferropericlase inclusions are too iron-rich to have equilibrated as part of an assemblage associated with primitive mantle peridotite or harzburgite. Several possible modes of origin have been postulated for these ferropericlase inclusions with lower Mg#s, including:

1. *The composition of the lower mantle is vastly different than primitive upper mantle* (Kaminsky et al. 2001; Kaminsky 2012). We consider this explanation improbable because the proportion and compositional range of syngenetic ferropericlase inclusions are expected to record diamond forming reactions (syngenesis) rather than entrapment of ambient mantle phases (protogenesis) in proportions or with compositions reflecting its bulk composition. For example, in the study by Nimis et al. (2019) nine iron-rich ferropericlase inclusions in two diamonds from Juina (Brazil) displayed a clear crystallographic orientation relationship between the diamond host and the inclusions indicative of co-crystallization during the diamond forming process.

2. *Ferropericlase crystallized in the deep lower mantle* where a spin-transition in iron (> ~1700 km) results in more iron-rich ferropericlase, or in the D" layer at base of the lower mantle due to an iron-rich composition or preferential partitioning of iron into ferropericlase relative to post-perovskite (Harte et al. 1999; Hayman et al. 2005; Wirth et al. 2014; Palot et al. 2016). Magnesioferrite $(Mg,Fe^{3+})Fe_2O_4$ exsolution blebs observed in ferropericlase, sometimes accompanied by sub-micron blebs of Fe-Ni metal, have been used as evidence in support of a deep lower mantle origin (Wirth et al. 2014; Palot et al. 2016). However, recent experimentally determined phase relations show that a stability field of magnesioferrite occurs at ~8 to 10 GPa (1000–1600 °C) and there is no indication of a high-pressure magnesioferrite stability field up to ~ 20 GPa (Uenver-Thiele et al. 2017), although one may exist at higher pressures (Andrault and Bolfan-Casanova 2001). We suggest that the simplest explanation for magnesioferrite blebs observed in ferropericlase inclusions is that they represent either exsolution from original ferropericlase with excess Fe_2O_3 under upper mantle conditions or oxidation by coexisting, carbonated fluids as described below (Thomson 2017; Uenver-Thiele et al. 2017). This exsolution is consistent with the low-pressure unmixing exhibited in both $CaSiO_3$-rich and $MgSiO_3$-rich inclusions described above. While the inclusions may have originated at higher pressures, neither the presence of magnesioferrite in ferropericlase nor their iron-rich compositions necessitate a lower mantle origin.

3. *Ferropericlase crystallized as a product of redox reactions* involving oxidized carbonate or carbonated melt and reducing peridotite at upper mantle, transition zone or lower mantle conditions (McCammon et al. 1997, 2004; Liu 2002; Bulatov et al. 2014, 2019; Thomson et al. 2016a; Seitz et al. 2018). Liu (2002) proposed that the range of iron-rich ferropericlase compositions may reflect the continuous subsolidus decarbonation of ferromagnesite according to the reaction:

$$\begin{aligned} 2\ \mathrm{Mg}_x\mathrm{Fe}_{1\text{-}x}\mathrm{CO}_3\ (\text{ferromagnesite}) &= \mathrm{Mg}_y\mathrm{Fe}_{1\text{-}y}\mathrm{CO}_3\ (\text{ferromagnesite}) \\ &+ \mathrm{Mg}_z\mathrm{Fe}_{1\text{-}z}\mathrm{O}\ (\text{ferropericlase}) + \mathrm{C}\ (\text{diamond}) + \mathrm{O}_2 \end{aligned} \tag{6}$$

In this reaction, the product ferropericlase solid solution becomes progressively iron enriched at the expense of ferromagnesite solid solution. As discussed below, there is ample evidence for the role of fluids or melts in sublithospheric diamond formation rather than subsolidus decarbonation, however, the essence of the decarbonation reaction suggested by Liu (2002) may equally apply to decarbonation in the liquid phase. Thomson et al. (2016b) performed experiments at 20 GPa in which a model carbonated melt of basaltic oceanic crust was reacted with reducing peridotite and both diamond and iron-rich ferropericlase were observed among reaction products. Similarly, Bulatov et al. (2019) showed experimentally that iron-rich ferropericlase and diamond can crystallize simultaneously during the reduction of carbonate-silicate melt in equilibrium with olivine at upper mantle conditions. Seitz et al. (2018) measured Li isotopes in iron-rich ferropericlase inclusions from Juina and observed a range that encompasses that of serpentinized ocean floor peridotites, fresh and altered MORB, seafloor sediments and of eclogites. They suggest that dehydration and redox reactions in altered portions of slabs subducted into the transition zone and shallow lower mantle led to the formation of diamond and iron-rich ferropericlase inclusions.

Iron redox state in ferropericlase. The redox state of iron in a small population of ferropericlase inclusions from both Kankan (high Mg#) and Juina (low Mg#) has been measured by Mossbauer spectroscopy (McCammon et al. 1997, 2004) and compared to experimentally determined Fe^{3+} solubility in ferropericlase applicable to depths at the top of the lower mantle (Otsuka et al. 2013). The oxygen fugacities calculated from measured $Fe^{3+}/\sum Fe$ are close to the upper stability limit of diamond and higher than expected in ambient mantle peridotite in the shallow lower mantle (Frost and McCammon 2008; Otsuka et al. 2013). Thus, if these ferropericlase inclusions are formed in the shallow lower mantle, especially those co-occurring with $MgSiO_3$-rich phases that also have high ferric iron content, their high Fe^{3+} concentrations may record diamond formation in a region of redox gradients. Such regions in the upper mantle or shallow lower mantle may arise from subduction of oxidized material into reducing mantle, and the inclusions may have precipitated from oxidized, carbonate-bearing melts or fluids (McCammon et al. 2004; Rohrbach and Schmidt 2011; Otsuka et al. 2013; Thomson et al. 2016a).

Trace element compositions

Trace elements have been analyzed in thirty-eight of the ferropericlase inclusions and data are provided in Table 9 (Available at: https://doi.org/10.5683/SP3/LIVK1K) and plotted as spidergrams on Figure 19, normalized to BSE. Twenty-one of the inclusions were measured by SIMS at the EIMF (Hutchison 1997; Harte et al. 1999; Burnham et al. 2016) and seventeen by LA-ICP-MS (Kaminsky et al. 2001). Also shown on this diagram are the calculated abundance patterns for ferropericlase in meta-peridotitic and meta-harzburgitic assemblages at lower mantle conditions.

Ferropericlase inclusions are generally depleted in lithophile trace elements relative to BSE but show a wide variation, with many elements spanning several orders of magnitude.

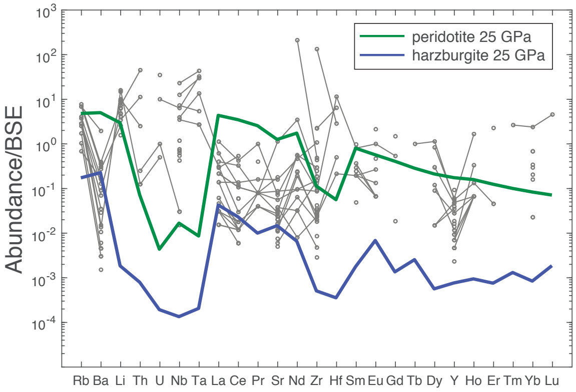

Figure 19. Trace element abundances in ferropericlase inclusions from the global dataset normalized to BSE. Also shown are calculated abundance patterns for ferropericlase expected in meta-peridotite (bridgmanite + Ca-silicate perovskite + ferropericlase) and meta-harzburgite (bridgmanite perovskite + ferropericlase) in the lower mantle at 25 GPa. Mineral modes and partition coefficients are provided in Table 3.

Relative depletions are apparent in Ba and Y, as are enrichments in Rb and Li, and in some samples, Th, U, Nb and Ta. Overall, the REE appear to be relatively unfractionated, although data are sparse for many elements. Abundances are generally in the range predicted in models for peridotitic ferropericlase in the lower mantle but with notable differences. The REE generally fall between ferropericlase in primitive meta-peridotite and meta-harzburgite assemblages, whereas Th, U, Nb and Ta are notably enriched relative to the predicted depletions for these elements in lower mantle ferropericlase. The depletions in Ba and Y are also not predicted in these lithologies and likely are inherited from a distinct source.

OLIVINE

Olivine (orthorhombic, *Pbnm*) and its higher-pressure polymorphs, wadsleyite (orthorhombic, *I2/m*) and ringwoodite (cubic, $Fd\bar{3}m$), comprise approximately 60 vol% of primitive mantle lithologies in the upper mantle and transition zone as shown on Figure 1. Inclusions with $(Mg,Fe)_2SiO_4$ stoichiometry are one of the most common inclusions in lithospheric diamonds and are typically interpreted as representative of a peridotitic association (Stachel et al. 2022, this volume) but appear to be notably rare in diamonds that are demonstrably sublithospheric in origin. We compiled a global dataset consisting of twenty eight $(Mg,Fe)_2SiO_4$ inclusions observed in diamond suites that have been identified as sublithospheric (Table 10). Fifteen $(Mg,Fe)_2SiO_4$ inclusions co-occur with ferropericlase of which six also co-occur with an $MgSiO_3$-rich phase, and one co-occurs with both $MgSiO_3$-rich and $CaSiO_3$-rich phases. Two $(Mg,Fe)_2SiO_4$ inclusions occur with an $MgSiO_3$-rich phase and one with a $CaSiO_3$-rich phase. The remainder are reported to occur either in isolation or with other rare inclusion phases.

To our knowledge, all of the inclusions included in Table 10 (Available at: https://doi.org/10.5683/SP3/LIVK1K) occur in the olivine structure. There is a single occurrence of a reported inclusion with the ringwoodite structure on the basis of Raman and X-ray diffraction measurements taken while the inclusion remained within the diamond (i.e., unexposed at the surface) with the data indicating an Mg# of ~0.75 ± 0.2 and containing about 1.5 wt% water (Pearson et al. 2014); geochemical data is not available from this inclusion so it is not part of our dataset.

The major element compositions of the $(Mg,Fe)_2SiO_4$ inclusions, as determined by electron microprobe analyses, are provided in Table 10 (Available at: https://doi.org/10.5683/SP3/LIVK1K) and plotted in Figure 20 along with 1478 olivine inclusion from lithospheric diamonds for comparison. Also shown are olivine, wadsleyite and ringwoodite compositions produced in experiments using primitive peridotite compositions at pressures >10 GPa.

Figure 20 shows that, overall, $(Mg,Fe)_2SiO_4$ inclusions are unlike the bulk of olivine inclusions in lithospheric diamonds. Lithospheric inclusions commonly have Mg#s between ~0.91–0.95, whereas the majority of sublithospheric $(Mg,Fe)_2SiO_4$ inclusions have Mg#s <0.91, with the remainder greater than 0.94. Many sublithospheric $(Mg,Fe)_2SiO_4$ inclusions have low NiO, high CaO, high Al_2O_3 and high Cr_2O_3. The low NiO contents of the $(Mg,Fe)_2SiO_4$ inclusions coexisting with an $MgSiO_3$-rich phase is consistent with the low-NiO contents of those inclusions as well. In comparison to experimentally produced $(Mg,Fe)_2SiO_4$ phases, many of the inclusions are most akin to ringwoodite and least like olivine. Like many of the inclusions, ringwoodite in experiments are notably lower in Mg# than wadsleyite and olivine. While sharing some features with higher pressure $(Mg,Fe)_2SiO_4$ polymorphs, many of the inclusions have unique compositions making it difficult to assign them to a certain polymorph, yet it is clear that they are different from the bulk of lithospheric olivine inclusions.

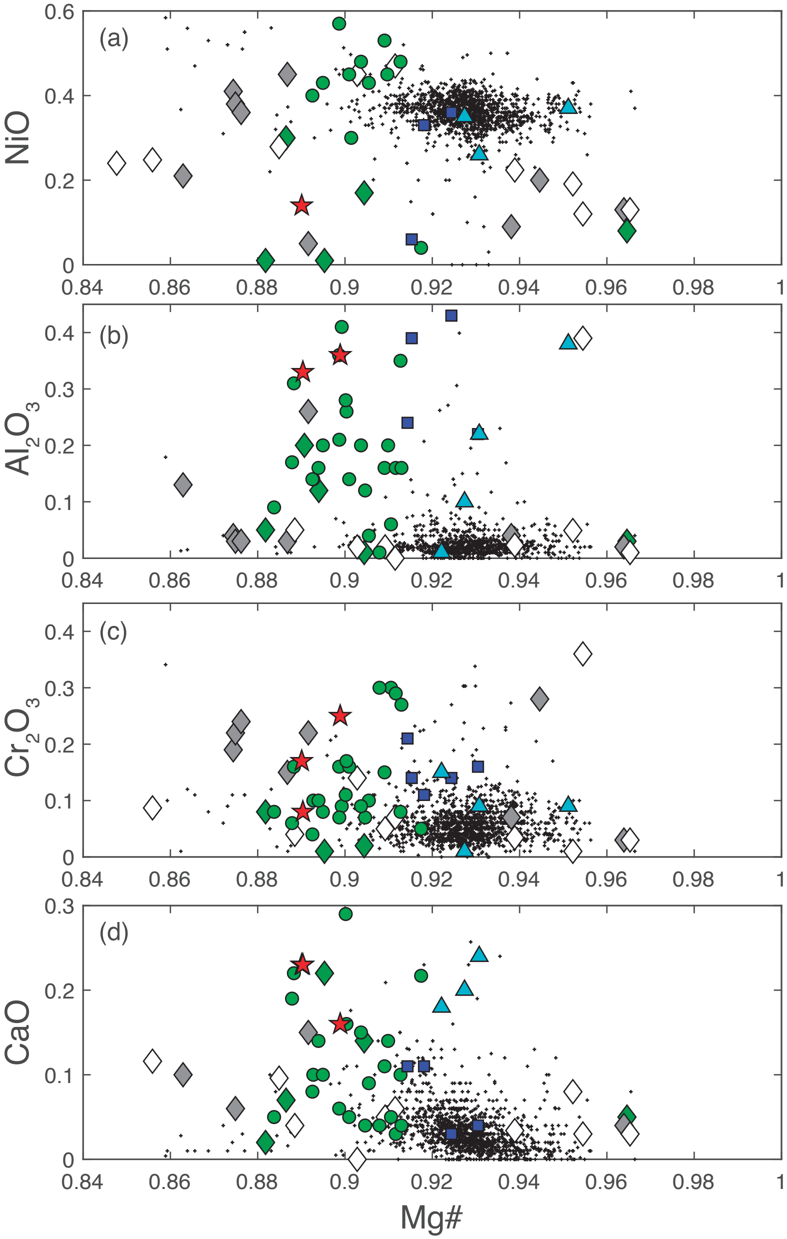

Figure 20. (a) NiO, **(b)** Al_2O_3, **(c)** Cr_2O_3 and **(d)** CaO versus Mg# showing olivine inclusions from the global dataset: **green diamonds**, co-occurring with ferropericlase, $MgSiO_3$, $\pm CaSiO_3$; **grey diamonds**, co-occurring with ferropericlase ±cpx ±jeffbenite; **white diamonds**, other; **crosses**, olivine inclusions in lithospheric diamonds (see Stachel et al. 2022, this volume for references); **green circles,** experimental ringwoodite in meta-peridotite; **red stars**, experimental ringwoodite coexisting with akimotoite; **blue squares**, experimental wadsleyite in meta-peridotite; **cyan triangles**, experimental olivine in meta-peridotite at 13–14 GPa in equilibrium with majoritic garnet ± cpx (Irifune and Ringwood 1987; Irifune 1994; Wood 2000; Hirose 2002; Ishii et al. 2011, 2018, 2019).

CLINOPYROXENE

Clinopyroxene (monoclinic) with $XY(Si,Al)_2O_6$ stoichiometry is a major constituent of meta-peridotitic (~20 vol%) and meta-basaltic assemblages (~60 vol%) at depths of ~ 300 km (Fig. 1) but disappears in these assemblages by ~400 to 500 km as it dissolves into majoritic garnet. Clinopyroxene inclusions, ranging from diopside to jadeite, are common in lithospheric diamonds but are much less common in sublithospheric diamonds. We compiled a global dataset consisting of forty clinopyroxene inclusions from four cratons in diamonds that have been identified as sublithospheric (Table 11—Available at: https://doi.org/10.5683/SP3/LIVK1K).

Clinopyroxene inclusions can be separated into two groups based on their Na_2O contents. ***High-Na*** clinopyroxene includes thirty inclusions with Na_2O ranging from 1.4 to 13.1 wt%, with bulk compositions that are generally augitic to omphacitic, but with one jadeite. The high-Na clinopyroxenes co-occur with garnet in twenty-six of the inclusions with compositions reported for twenty of these, all of which are majoritic and yield pressures ranging from ~9 to 18 GPa, providing direct evidence for their sublithospheric origin. ***Low-Na*** clinopyroxene includes ten inclusions with extremely low Na_2O of < 0.13 wt% and have compositions that are augitic to diopsidic. Five of these inclusions co-occur with ferropericlase and two of these with both ferropericlase and $MgSiO_3$-rich inclusions. Three clinopyroxene inclusions occur with a $CaSiO_3$-rich phase, and two of these also contain merwinite.

The major element compositions of clinopyroxene inclusions, as determined by electron microprobe analyses, are provided in Table 11 (Available at: https://doi.org/10.5683/SP3/LIVK1K) and plotted in Figure 21 along with 1321 clinopyroxene inclusions from lithospheric diamonds for comparison. Figure 21a shows a clear distinction between the low-Na and high-Na groups. High-Na pyroxene are generally much more aluminous and overlap extensively with 'eclogitic' lithospheric garnets in terms of Na_2O, CaO and Mg#. In contrast, the low-Na clinopyroxenes are relatively distinct, with extremely low Na_2O which does not increase with Al_2O_3 content, high CaO contents that are not seen in lithospheric inclusions and high Mg#s.

Also shown on Figure 21 are experimental clinopyroxene compositions from meta-peridotitic and meta-basaltic assemblages at pressures of 8 to 19 GPa. The high-Na inclusions are generally consistent with clinopyroxenes expected in meta-basaltic or meta-pyroxenitic assemblages, although we note that they generally do not overlap with clinopyroxenes produced in experiments on hydrous or carbonated eclogitic that are typically more alumina and sodium-rich and calcium poor relative to the inclusions. The low-Na group are generally unlike compositions produced in experiments on peridotitic compositions, especially in their very high CaO contents and low-Na_2O for a given alumina content.

SiO_2

An SiO_2 phase is reported to co-occur in fifteen diamonds hosting sublithospheric inclusions in our data sets. While coesite (monoclinic, C2/c) has been identified, the assumption is that the original inclusions were formed in the stishovite structure (tetragonal rutile-type, $P4_2/mnm$), which is the stable SiO_2 phase from ~ 9 to 75 GPa (Zhang et al. 1996; Fischer et al. 2018). SiO_2 occurs with majoritic garnet in seven diamonds in our dataset and the co-occurring majoritic garnets yield pressures of ~ 10 to 22 GPa (Table 1—Available at: https://doi.org/10.5683/SP3/LIVK1K). Two of the SiO_2 inclusions also exhibit exsolved kyanite indicating unmixing of alumina during retrogression. Two diamonds containing $CaSiO_3$-rich inclusions, both low-Ti $CaSiO_3$ from Brazil, also contain SiO_2 inclusions (Table 4—Available at: https://doi.org/10.5683/SP3/LIVK1K), whereas there are no reported co-occurrences of SiO_2 with $MgSiO_3$-rich, olivine or clinopyroxene inclusions in our data sets. SiO_2 inclusions

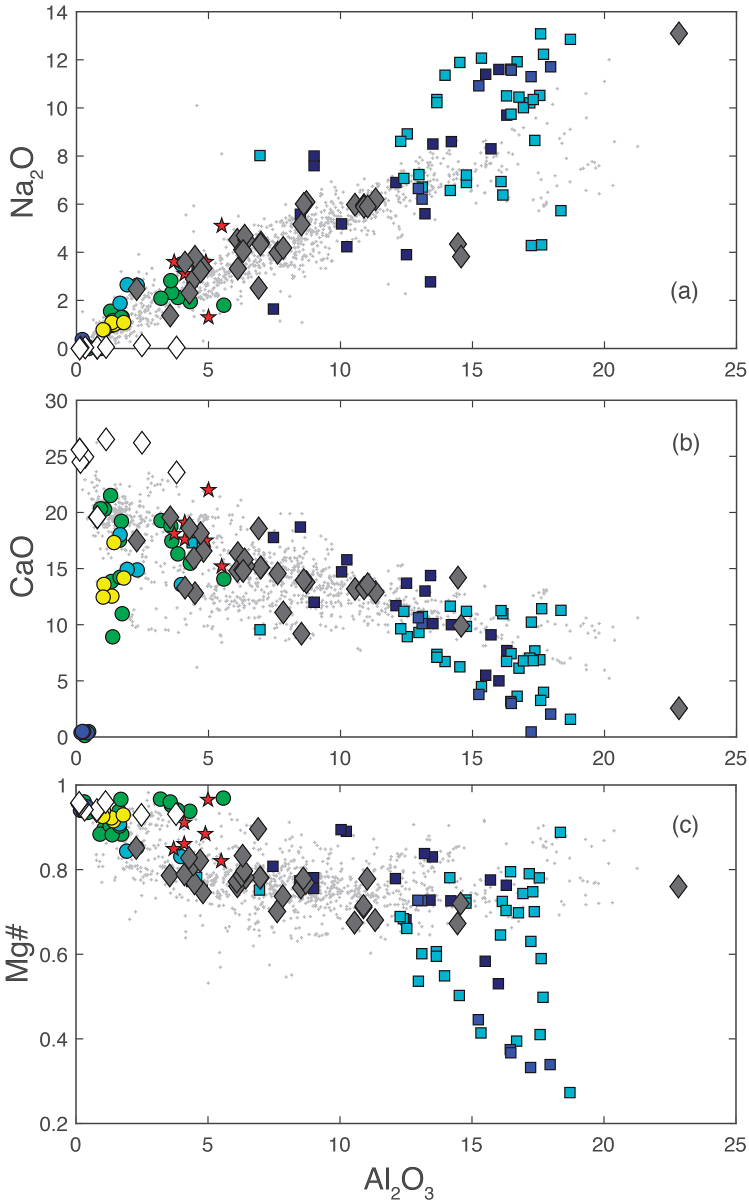

Figure 21. (a) Na$_2$O, **(b)** CaO and **(c)** Mg# versus Al$_2$O$_3$ showing clinopyroxene inclusions from the global dataset: **white diamonds**, low-Na inclusions; **dark gray diamonds, high-Na inclusions;** grey **crosses**, clinopyroxene inclusions in lithospheric diamonds (see Stachel et al. 2022, this volume, for references). Experimental clinopyroxene from the literature include: **green circles,** anhydrous fertile peridotite (Akaogi and Akimoto 1979; Irifune 1987; Ishii et al. 2018; Rzehak et al. 2020); **cyan circles,** carbonated peridotite (Ghosh et al. 2009); **yellow circles,** carbonated peridotite melt reaction experiments (Sun and Dasgupta 2019); **blue circles,** anhydrous harzburgite (Irifune and Ringwood 1987; Ishii et al. 2019); **dark blue squares,** anhydrous basalt (Irifune et al. 1986; Beyer and Frost 2017; Ishii et al. 2019); **light blue squares,** hydrous basalt (Okamoto and Maruyama 2004); **cyan squares,** carbonated basalt (Kiseeva et al. 2013a; Thomson et al. 2016a); **red stars,** anhydrous pyroxenite (Beyer and Frost 2017).

co-occur with ferropericlase in five diamonds, with examples from three cratons (Table 8—Available at: https://doi.org/10.5683/SP3/LIVK1K).

In addition to diamonds included in our data sets, nine coesite inclusions were reported in diamonds from the Juina-5 and Collier-4 kimberlites, Brazil (Burnham et al. 2015), and as isolated inclusions in diamonds from Sao Luiz, Brazil (Zedgenizov et al. 2014a). With the exception of inclusions containing evidence for exsolved kyanite, SiO_2 inclusions are reported to be nearly phase pure with only trace amounts of other elements including TiO_2 and Al_2O_3 (Bulanova et al. 2010; Kaminsky 2012; Thomson et al. 2014; Zedgenizov et al. 2014a; Burnham et al. 2015).

The occurrence of stishovite associated in diamonds with other inclusions of meta-basaltic affinity (e.g., Ti-rich $CaSiO_3$, low-Cr majoritic garnet) is expected based on phase relations (Fig. 1). Burnham et al. (2015) measured the carbon isotopic compositions of host diamonds and the oxygen isotopic composition of coesite inclusions from the Collier-4 and Juina-5 kimberlites, Brazil, two localities that have produced a variety of inclusions of meta-basaltic affinity and found a range of negative carbon isotopic compositions and positive oxygen isotopic compositions consistent with an origin related to subducted oceanic crust.

However, the co-occurrence of SiO_2 with ferropericlase, which is generally attributed to a peridotitic association, requires a different explanation. At lower mantle conditions in the MgO–FeO–SiO_2 system, ferropericlase and stishovite occur together once the FeO solubility in bridgmanite is exceeded, and at ambient lower mantle temperatures (e.g., ~1600 °C) this occurs at ~12 mol% FeO (Fei et al. 1996). However, at < ~1100 °C, bridgmanite breaks down to ferropericlase plus stishovite at < ~5 mol% FeO, and in a fertile mantle composition a field of ferropericlase coexisting with stishovite and Ca-silicate perovskite occurs at ~25 GPa at temperatures < ~900 °C (Stixrude and Lithgow-Bertelloni 2011). Thus, the association of stishovite and ferropericlase may represent bridgmanite breakdown associated with either iron-rich lithologies or low temperatures. The Mg#s of ferropericlase co-occurring with stishovite in our data set range from 0.78 to 0.86, with most 0.84 and above. For a fertile mantle these are far too magnesian to be in equilibrium with stishovite at mantle temperatures, and thus are either not in equilibrium with co-occurring stishovite (Stachel et al. 2000b), or were equilibrated at much lower temperatures.

CF AND NAL PHASES

Composite inclusions with bulk stoichiometries consistent with the calcium ferrite (CF) structured phase and new aluminous (NAL) phase that occur in meta-basaltic assemblages at conditions of the lower mantle (Fig. 1) have been described in diamonds from Brazil (Walter et al. 2011; Thomson et al. 2014; Zedgenizov et al. 2014a). Within their stability fields the CF phase is orthorhombic (*Pbnm*) and has the general formula XY_2O_4 ($X = K^+, Na^+, Ca^{2+}, Mg^{2+}$; $Y = Al^{3+}$ and Si^{4+}), whereas the NAL phase is hexagonal ($P6_3/m$) and has the general formula $AX_2Y_6O_{12}$ ($A = Na^+, K^+, Ca^{2+}$; $X = Mg^{2+}, Fe^{2+}$; $Y = Al^{3+}, Si^{4+}$ (Miyajima et al. 2001; Wicks and Duffy 2016). Inclusions interpreted as retrograde CF phase are found as composite mixtures of spinel $(Mg,Fe)Al_2O_4$ and nepheline $NaAlSiO_4$, whereas NAL phases as composite mixtures of spinel and a nepheline–kalsilite phase, $(Na,K)AlSiO_4$. Bulk inclusion compositions as determined by wide beam EPMA analysis or reconstruction from phase modes (Walter et al. 2011; Thomson et al. 2014) yield stoichiometries close to the ideal CF and NAL phases produced in experiments on basaltic compositions (Ono et al. 2001; Ricolleau et al. 2010; Ishii et al. 2019), providing strong evidence for the role of subducted oceanic crust in their origin. Trace elements have been reported for six NAL phases and two CF phases (Thomson et al. 2016b) and abundance patterns generally display depletion in REE and large negative Y anomalies and relative enrichments in Th, U, Nb, Ta and Rb relative to BSE.

DISCUSSION

We assembled comprehensive datasets of silicate and oxide inclusions in sublithospheric diamonds that ostensibly represent major rock forming minerals in the mantle (majoritic garnet, Ca-silicate perovskite, bridgmanite, ferropericlase, olivine and clinpyroxene). The major and trace element compositions of the inclusions combined with experimental phase equilibrium and element partitioning data provide a basis for conceptual models of their origin and reveal information about mantle geodynamic processes leading to diamond formation.

The geochemical features of the sublithospheric inclusions generally permit a distinction between a meta-basaltic association (low-Cr majoritic garnet; high-Ti $CaSiO_3$; low Mg#, high-Al $MgSiO_3$; CF and NAL phases) and a meta-peridotitic association (high-Cr majoritic garnet; low-Ti $CaSiO_3$; low-Al, high Mg# $MgSiO_{3;}$ ferropericlase) (Stachel et al. 2005; Harte 2010). However, it is also apparent from experimental major element systematics and trace element modeling that inclusion compositions generally do not conform, with very few exceptions, to expectations for primary subsolidus minerals in primitive meta-peridotitic assemblages (e.g., pyrolite) or meta-basaltic (e.g., MORB) assemblages at upper mantle, transition zone or lower mantle conditions.

The geochemistry of syngenetic sublithospheric inclusions cannot be separated from models for how the host diamonds form, and like their lithospheric counterparts, sublithospheric diamonds exhibit abundant evidence for crystallization from fluids or melts. Therefore, to provide context for general models of inclusion genesis we first discuss observations regarding diamond crystallization.

Diamond precipitation from fluids and melts

It is well-established that diamonds originating in cratonic lithospheric mantle precipitate primarily from carbon-bearing fluids (Deines 1980; Sunagawa 1984; Haggerty 1986; Bulanova 1995; Shirey et al. 2013) and they provide a baseline for comparison with sublithospheric diamonds. On the basis of fluid inclusions trapped in fibrous diamonds from the lithosphere the parental fluids exhibit a range in composition, including high- and low-Mg carbonatitic, chlorine-rich and silica-rich aqueous fluids (Klein-BenDavid et al. 2007, 2009; Weiss et al. 2013, 2014). Cathodoluminescence imaging of lithospheric diamonds reveals internal growth textures with intricate, concentric zoning, as well as evidence of resorption and recrystallization, textures indicative of precipitation from carbon-saturated fluids as opposed to solid-state transformation from graphite (Bulanova 1995; Shirey et al. 2013). Further evidence for fluid-mediated diamond precipitation includes fracture infillings (Czas et al. 2018) and systematic changes in carbon and nitrogen abundance and isotopic composition, features that are consistent with crystallization from a fractionating fluid phase (Boyd et al. 1987; Smart et al. 2011).

Sublithospheric diamonds can potentially form through subsolidus decarbonation reactions in the mantle, for example, through reaction with silica in oceanic crust (Maeda et al. 2017; Li et al. 2018; Drewitt et al. 2019) or through reaction of carbonate with reduced phases such as iron or iron carbide (Liu 2002; Zhu et al. 2019). However, sublithospheric diamonds typically have internal textural features that are similar to lithospheric diamonds, displaying intricate, complex growth layering, and in some cases multiple nucleation centers, indicative of crystallization from fluids or melts, examples of which are provided in Figure 22 (Hayman et al. 2005; Bulanova et al. 2010; Thomson et al. 2014; Zedgenizov et al. 2014a; Palot et al. 2017). An exception may be CLIPPIR and Type IIb diamonds, which typically have no discernible growth structure but show abundant dislocation networks indicative of plastic deformation and annealing (Smith et al. 2016b, 2018). Sublithospheric diamonds commonly exhibit deformation textures indicative of residence in a high-strain environment at high temperature (Bulanova et al. 2010; Thomson et al. 2014; Smith et al. 2016a, 2018; Shirey et al. 2019). Sublithospheric diamonds also preserve both small-scale and large-scale intra-diamond carbon isotope variations among growth zones (Fig. 22), consistent with growth from fractionating fluids/melts or multiple episodes of growth from fluids/melts of variable composition (Stachel et al. 2002; Bulanova et al. 2010; Shirey et al. 2013, 2019; Thomson et al. 2014; Zedgenizov et al. 2014a). In contrast to lithospheric diamonds, which are often regular crystal forms and can exhibit fluid-inclusion-rich fibrous diamond growth, sublithospheric diamonds tend to have more irregular morphologies and fibrous diamond growth has not been observed.

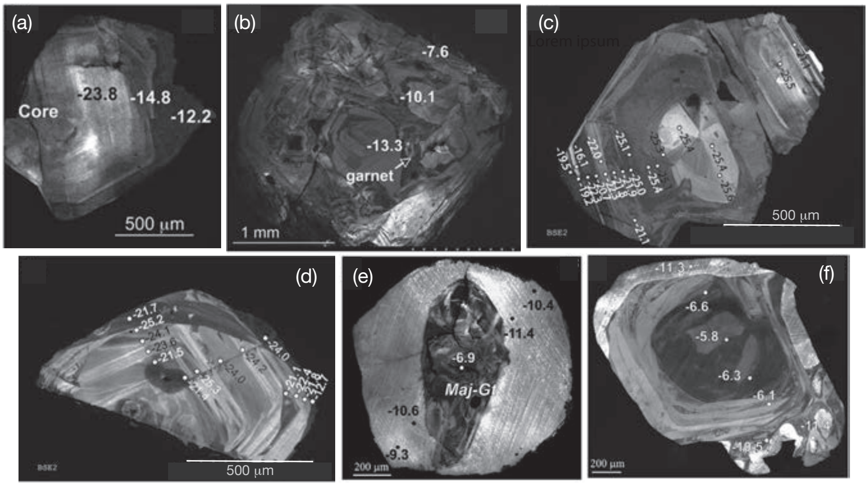

Figure 22. Cathodoluminescence images of sublithospheric diamonds from the Juina region of Brazil. Carbon isotopic compositions $\delta^{13}C$ (‰ relative to PDB standard) are shown at the positions they were analyzed by SIMS. **(a)** diamond with weak octahedral zonation and a large change in $\delta^{13}C$ from core to rim (J2, Collier 4); **(b)** diamond with a core zone with a rounded octahedral/rounded shape and resorption surrounded by an intermediate region showing irregular-aggregate growth with features indicative of deformation and inclusions of diamond-in-diamond in this zone indicating nucleation of multiple diamond seeds, and a narrow rim zone with fine octahedral zoning and plastic deformation (J9, Collier 4); **(c)** octahedral crystal with sector zoned cubo-octahedral core and octahedral zonation (Ju5-115, Juina 5); **(d)** blocky octahedral core and regular octahedral zonation with rounded resorbed corners (Ju5-71, Juina 5); **(e)**; rounded octahedral core with complex zonation with a thick rim showing evidence of plastic deformation present as a 'tatami' pattern with lines that do not correspond to the core zoning structure (36, Sao Luiz); **(f)** Rounded octahedral core showing evidence of intermittent growth and resorption with irregular outer zonation and a rim showing evidence of plastic deformation (34, Sao Luiz). ***Credits***: **a,b** Reprinted by permission from Springer Nature Customer Service Centre GmbH: Springer Nature. Bulanova et al. (2010), Copyright 2010); **c,d** CC BY Thomson et al. (2014); **e,f** Reprinted from Zedgenizov et al. (2014a), Copyright (2014), with permission from Elsevier.

Diamonds precipitate from fluids or melts when carbon species, such as CO_2, CH_4, CO_3^{2-}, or HCO_3^-, become reduced or oxidized as a consequence of changes in temperature (Luth and Stachel 2014; Stachel and Luth 2015), pH (Sverjensky and Huang 2015) and redox conditions (Haggerty 1986; Frost and McCammon 2008; Bulanova et al. 2010; Rohrbach and Schmidt 2011; Shirey et al. 2013; Stagno et al. 2013; Thomson et al. 2016a) (see also Luth et al. 2022, this volume). Gradients in these variables exist, for example, when carbon-bearing fluids and melts permeate and migrate through rocks. On the basis of tomographic imaging of eclogitic mantle xenoliths from cratonic lithosphere, diamonds precipitate at silicate grain boundaries, exhibiting growth along intergranular planes that likely served as pathways for fluid flow (Anand et al. 2004; Liu et al. 2009b; Czas et al. 2018). There are no such examples of diamondiferous sublithospheric mantle xenoliths, but the diamond textural similarities described above are suggestive of a similar fluid-mediated crystallization. By inference, crystalline silicate and oxide inclusions in sublithospheric diamonds likely equilibrated with or crystallized directly from dissolved components in fluids or melts migrating through rocks in subducted lithosphere or the mantle.

Because sublithospheric diamonds are believed to grow at much greater depths than lithospheric diamonds, the fluids and melts will also possess a different chemical character. For example, H_2O-rich fluids are expected to be well beyond their second critical endpoints in both peridotitic and basaltic systems, transitioning into hydrous melts with a large fraction of dissolved silicate component (Kessel et al. 2005; Mibe et al. 2007; Liu et al. 2009a; Mibe et al. 2011; Kawamoto et al. 2012; Wang et al. 2020). Before considering the types of fluids and melts that sublithospheric inclusions may crystallize from, we consider evidence from stable isotopes, particularly carbon, that provide further context for potential source lithologies and for understating different populations of sublithospheric diamonds and their inclusions.

Stable isotope compositions of diamonds and inclusions

The stable isotope compositions of sublithospheric diamonds and their inclusions have been used extensively to inform interpretations of their origin (Deines 1980; Deines et al. 1991; Hutchison et al. 1999; Cartigny 2005; Bulanova et al. 2010; Palot et al. 2012; Shirey et al. 2013, 2019; Thomson et al. 2014; Zedgenizov et al. 2014a; Burnham et al. 2015; Ickert et al. 2015) (see also Stachel et al. 2022b, this volume). Carbon and nitrogen isotopes of the diamonds and oxygen isotopes of inclusions can provide evidence for potential source lithologies of carbon-bearing fluids and melts.

Carbon isotopes have been measured most extensively using SIMS, often at a spatial scale of individual growth layers, revealing distinct populations among sublithospheric diamonds. Figure 23 shows frequency histograms of the carbon isotopic composition for diamonds hosting inclusions in our database, separated by inclusion type. The primitive mantle is assumed to have a carbon isotopic composition of about $\delta^{13}C = -5 \pm 2‰$ (relative to a PDB carbonate standard), whereas carbon in subducted lithosphere lithologies varies from about $\delta^{13}C = 0‰$ (e.g., seawater carbonate) to values lower than $\delta^{13}C = -25‰$ that plausibly represent a source of either biogenic or abiogenic organic carbon (Cartigny 2005). A remarkable distinction is apparent between diamonds hosting inclusions with compositions consistent with a meta-peridotitic association relative to those with a meta-basaltic association.

Both major element and trace element characteristics of low-Cr majoritic garnet inclusions indicate a meta-basaltic or mixed basaltic-peridotitic (meta-pyroxenitic) association. The carbon isotopic composition of diamonds hosting low-Cr garnet inclusions (Fig. 23a) show a wide range of values between about $\delta^{13}C = -3$ to $-25‰$, with the majority being substantially isotopically lighter than mantle carbon, suggestive of a source of carbon in subducted slab lithologies, in particular basaltic oceanic crust (Kaminsky et al. 2001; Stachel et al. 2002; Cartigny 2005; Bulanova et al. 2010; Palot et al. 2012, 2017; Cartigny et al. 2014; Thomson et al. 2014; Zedgenizov et al. 2014a). Supporting this interpretation are measurements of isotopically heavy oxygen exhibited by garnet and SiO_2 inclusions hosted by diamonds with isotopically light carbon, with heavy oxygen attributed to interaction of oceanic crust with seawater (Burnham et al. 2015; Ickert et al. 2015). Further support for this interpretation comes from nitrogen isotopes. Although sublithospheric diamonds generally have very low N contents (~70% are Type II and >90% have N < 100 at.ppm), where it has been analyzed in diamonds that contain low-Cr majoritic garnet, N isotopes are heavy relative to primitive mantle, consistent with an oceanic crustal source (Palot et al. 2012; Regier et al. 2020). Very few of the diamonds hosting high-Cr majoritic garnets have been measured for C isotopes. Four of the five have generally low mantle-like values with one much lighter, but the data is too sparse to draw any firm conclusions.

Diamonds hosting $CaSiO_3$-rich inclusions (Fig. 23b) show a range of $\delta^{13}C$ from about 0 to $-25‰$. Although the measurements are relatively few, there is an apparent distinction between diamonds hosting low-Ti and high-Ti inclusions. Diamonds containing low-Ti inclusions,

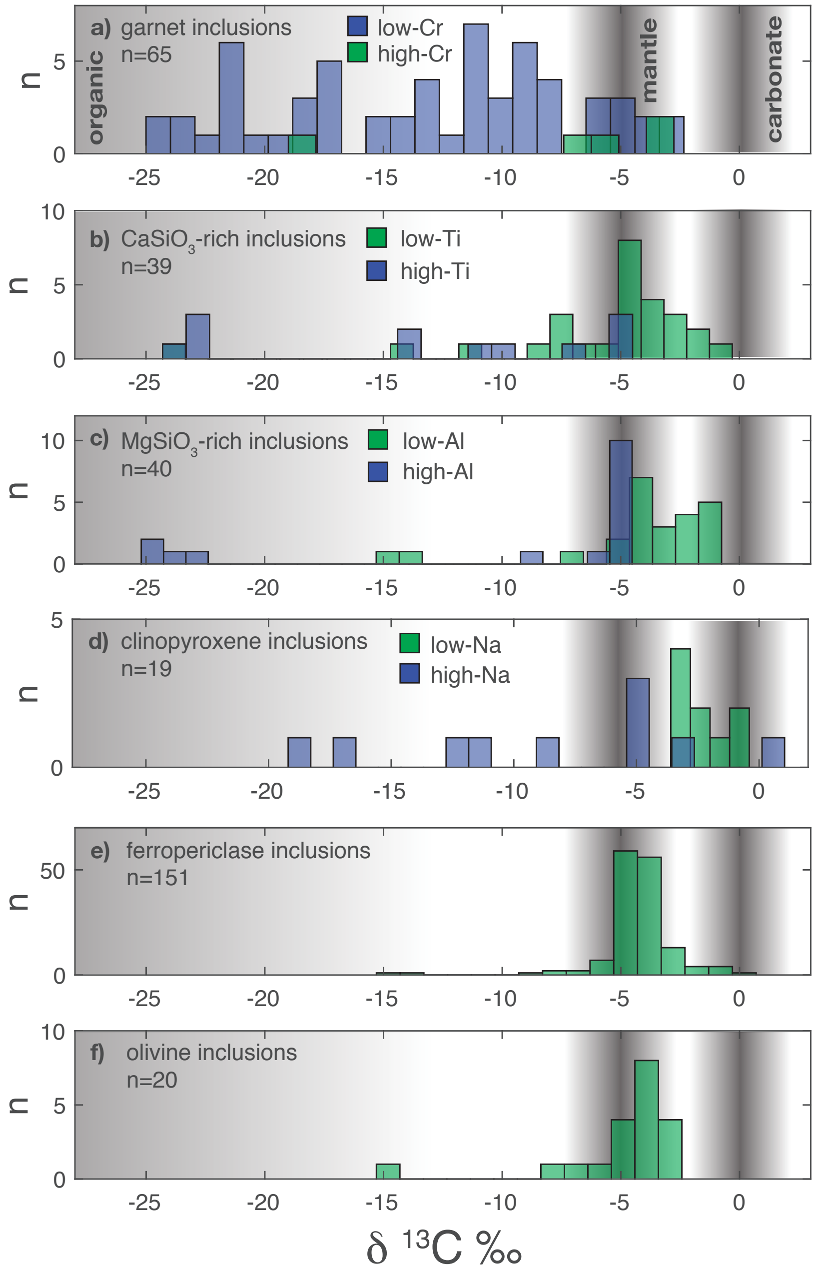

Figure 23. Histograms of carbon isotope (δ^{13}C ‰) compositions of diamonds hosting inclusions in our data compilation (data in Tables 1, 4, 6, 8, 10, 11). Values of mantle carbon, and recycled carbon (seawater carbonate and 'organic' carbon) are based on ranges given in Cartigny (2005). **(a)** Garnet inclusions separated into low-Cr and high-Cr groups; **(b)** $CaSiO_3$-rich inclusions separated into low-Ti and high-Ti groups; **(c)** $MgSiO_3$ inclusions separated into low-Al and high-Al groups; **(d)** clinopyroxene inclusions separated into low-Na and high-Na groups; **(e)** ferropericlase inclusions; **(f)** olivine inclusions.

with chemical features most consistent with a meta-peridotitic association, generally have heavier C, with isotope compositions exhibiting a peak overlapping with mantle carbon; exceptions include one diamond with very light carbon (~ –23‰) and one with anomalously heavy carbon (~ –1‰). In contrast, high-Ti inclusions, with chemical features consistent with a meta-basaltic association, generally occur in diamonds with lighter carbon, with a range similar to low-Cr majoritic garnet.

Diamonds hosting $MgSiO_3$-rich inclusions also show a range of $\delta^{13}C$ from about 0 to –25‰ (Fig. 23c). Low-Al $MgSiO_3$-rich inclusions with chemical features indicating a meta-peridotitic association predominantly occur in diamonds with heavy C, $\delta^{13}C$ from about 0 to –4‰, with two exceptions at $\delta^{13}C$ of ~ –15‰. Indeed, carbon isotope signatures among this group tend to show heavier C than in normal mantle. Although measurements are sparse, high-Al inclusions that are more consistent with a meta-basaltic association occur in diamonds that have $d^{13}C$ from about –5 to –25‰, similar to low-Cr majoritic garnet and high-Ti $CaSiO_3$-rich inclusion-bearing diamonds. Similarly, diamonds with clinopyroxene inclusions (Fig. 23d) with high Na that are compositionally akin to a meta-basaltic association show a wide range of $\delta^{13}C$ from ~ 0 to –18 ‰, whereas diamonds with low Na clinopyroxene are isotopically heavy, generally intermediate between mantle and carbonate.

Ferropericlase inclusions (Fig. 23e) occur in diamonds with a relatively narrow distribution of carbon isotopes with a peak at $\delta^{13}C$ ~ –4‰, generally consistent with mantle carbon but with a distribution toward both heavier and lighter carbon. Diamonds hosting olivine (Fig. 23f) inclusions exhibit a similar distribution to ferropericlase but with a few notable outliers to much lighter C. Both ferropericlase and olivine are minerals typically associated with a meta-peridotitic association, which is generally consistent with their carbon isotope compositions.

Variations in carbon isotopes within diamonds hosting inclusions with compositions indicating a meta-basaltic association (e.g., low-Cr garnet, high-Ti $CaSiO_3$) can be large across growth zones (Fig. 22) (Bulanova et al. 2010; Palot et al. 2012; Thomson et al. 2014; Zedgenizov et al. 2014a). Such large variations can be attributed to changes in the source of carbon in fluids or melts contributing to diamond growth rather than fractionation of carbon during diamond precipitation. In cases where measurements have been made in diamonds from core to rim, examples are found for both large core to rim increases and decreases in carbon isotopic compositions, although there is an apparent tendency that when diamond cores are isotopically light the rims tend to be heavier (Fig. 22) (Bulanova et al. 2010; Thomson et al. 2014; Zedgenizov et al. 2014a; Palot et al. 2017). For example, in ten cases where cores had isotopic compositions lower than $\delta^{13}C$ = –20‰, the compositions of rims were notably heavier extending in some cases to near mantle values (Thomson et al. 2014). Such variations might represent mixing of carbon sources as melts and fluids derived from oceanic crust mix with carbon derived from the mantle as they migrate and evolve (Burnham et al. 2015).

The origin of sublithospheric inclusions in fluids and melts

On the basis of the major, trace and isotopic composition of sublithospheric diamonds and their mineral inclusions both carbonated melts and carbon-bearing hydrous fluids or melts have been postulated as potential diamond-forming media (Walter et al. 2008; Bulanova et al. 2010; Harte 2010; Stachel and Luth 2015; Palot et al. 2016; Thomson et al. 2016a,b; Smith et al. 2018; Timmerman et al. 2019; Zhu et al. 2019) (see also Luth et al. 2022, this volume). We note these kinds of fluids/melts are not mutually exclusive and any melt or fluid in the mantle will likely contain carbon, hydrogen and other volatile incompatible elements. Also implicated as a potential fluid growth medium are Fe–Ni–S–C metallic alloy or sulfide melts (Smith et al. 2016b). Subducting lithospheric slabs are most commonly suggested as the source of volatile-rich fluid components, and here we assess these model diamond-forming fluids.

Low-degree carbon-rich melts and the origin of meta-basaltic inclusions. Inclusions indicating a genetic relationship with meta-basaltic assemblages have been most closely linked to an origin involving low-degree melts of subducted oceanic crust. Lithophile trace element abundances observed in low-Cr majorite and high-Ti $CaSiO_3$-rich phases (Fig. 6 and 9), coupled with considerations of melting phase relations, have been interpreted to reflect equilibration with a low-degree melt of subducted oceanic crust, generally in the range of 300 to 600 km (Walter et al. 2008; Bulanova et al. 2010; Zedgenizov et al. 2014a; Thomson et al. 2016a,b). In this model, diamond co-crystallizes from carbon-bearing low-degree melts through redox reactions as melts migrate away from the oceanic crust and into peridotite, either within the slab or outside the slab in ambient mantle (Bulanova et al. 2010; Rohrbach and Schmidt 2011; Walter et al. 2011; Sun et al. 2020). Modeling indicates that melts can migrate through channelized porous flow and depending on the flux from the slab, remain molten for millions of years, reacting and differentiating as they move (Sun and Dasgupta 2019; Sun et al. 2020, 2021).

Figure 24 shows calculated trace element abundances (normalized to MORB) in melts that could coexist with low-Cr majoritic garnet, high-Ti Ca-silicate perovskite and low Mg#/high-Al bridgmanite on the basis of experimental mineral–melt partition coefficients (Table 3—Available at: https://doi.org/10.5683/SP3/LIVK1K). Also shown for comparison are calculated low-degree melts ($F = 0.01$) of model MORB and processed MORB at 20 GPa as well as the compositions of a suite of oceanic carbonatites (Hoernle et al. 2002). Overall, there is a good correspondence among the calculated coexisting melts from the three meta-basaltic inclusion types, suggesting a similar parental melt compositions, including enrichments in highly incompatible elements (e.g., Th, U, Nb, Ta, La, Ce) and common relative depletions in Sr, Zr, Hf and Pb (not shown, typically unmeasured or below detection limit). Bulanova et al. (2010) and Thomson et al. (2016a) presented trace element models that included Ca-silicate perovskite and majoritic garnet fractionation that can plausibly explain much of the observed trace element abundance variations in inclusion sample suites from individual pipes in the Juina region (e.g., Collier-4, Juina-5). In particular the trace element abundances of the $CaSiO_3$-rich inclusions are strikingly similar to low-degree melts of oceanic crust and with carbonatites from oceanic settings. The expected high U/Pb and relatively unfractionated Rb/Sr and Lu/Hf makes these melts putative candidates for imposing a chemical character to the mantle they interact with that could grow a HIMU like isotopic character over time (Sun et al. 2021).

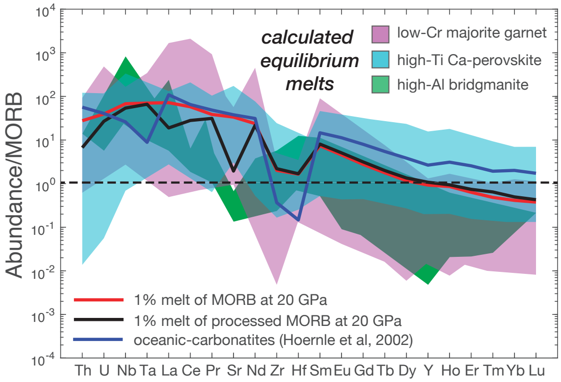

Figure 24. Trace element spider diagram showing MORB normalized abundances of calculated melts that could be in equilibrium with low-Cr majorite (**pink field**), high-Ti Ca perovskite (**cyan field**) and high-Al bridgmanite (**green field**) and model melts for 1% partial melting of MORB at 20 GPa (**red line**) and 1% melting of 'processed' MORB (**black line**) at 20 GPa, using partition coefficients from Table 3. Also shown is an average composition of oceanic carbonatite (Hoernle et al. 2002).

Figure 25 shows the solidus of carbonated oceanic crust (Kiseeva et al. 2013a; Thomson et al. 2016a; Zhang et al. 2020) relative to calculated pressure-temperature profiles for subducting lithosphere at the slab top and Moho in modern subduction zone settings (Shirey et al. 2021). Differences in the solidi among the experimental studies can generally be attributed to variations in the Ca/Mg of the source basalt and should reflect expected variations in subducted, altered MORB. The "slab-therms" indicate that carbonated oceanic crust will melt at pressures of about 13 GPa or greater, with only the coldest slabs potentially avoiding melting. Addition of water to the carbon-bearing system will reduce the solidus further, making melting of oceanic crust an inevitable consequence of subduction to deep upper mantle and transition zone depths.

Subducting slabs are believed to often stagnate in the transition zone due to a combination of buoyancy forces related to phase transitions (Bina 1997; Billen 2008), such that most or all slab crust may be expected to undergo carbonated melting in the transition zone at ~1100–1200 °C. We note that majoritic garnet inclusions indicate two pressure modes at about 9 and 14 GPa (Fig. 4), or with a plausible exsolution correction, at about 13 and 18 GPa (Thomson et al. 2021). The high pressure mode in particular, which is dominated by low-Cr garnets of the meta-basaltic association (Fig. 5b), occurs at pressures generally consistent with a model for melting of carbonated oceanic crust. The experiments of Thomson et al. (2016b) also showed that the products of reaction between carbonated melt from oceanic crust and mantle peridotite include low-Cr, high Ca majorite garnet with compositions intermediate to meta-peridotitic and meta-basaltic majoritic garnet, high-Ti Ca-perovskite with low MgO, and ferropericlase with variable but low Mg#s, all features that are consistent with observations from meta-basaltic inclusions in sublithospheric diamonds.

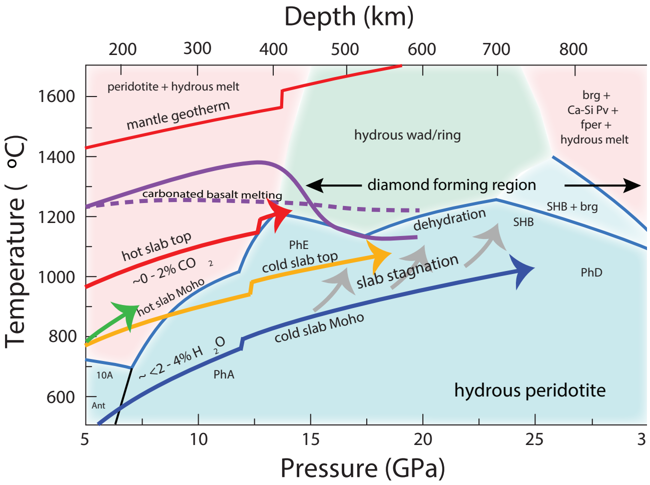

Figure 25. Pressure–temperature diagram showing generalized phase relations for water-saturated peridotite (Poli and Schmidt 2002; Iwamori 2004; Kawamoto 2004; Komabayashi and Omori 2006; Shirey et al. 2021). Phase labels designate generalized regions of stable hydrous magnesian silicates: ant = antigorite; PhA = phase A; PhE = phase E; PhD = phase D; SHB = superhydrous phase B; wad = wadsleyite; ring = ringwoodite; brg = bridgmanite. Average geotherms for cold and hot slabs are shown for peridotite at the Moho (**blue and green arrows**) and for the top of the oceanic crust (**orange and red arrows**) and are from Shirey et al. (2021). Reactions where hydrous phases dehydrate are shown as **solid blue lines**. Melting curves for carbonated basalt are shown as **purple curves** (solid: Thomson et al. 2016b; dashed: Kiseeva et al, 2013). The mantle geotherm is from Katsura et al. (2010). Cold slab mantle can transport H_2O beyond antigorite breakdown and into the transition zone. Slab stagnation and heating may cause dehydration throughout the transition zone and into the shallow lower mantle at temperatures of ~1100 to 1300 °C. Carbonated oceanic crust melts at approximately the same temperature as slab mantle dehydrates, potentially creating a diamond forming region throughout the transition zone and shallow lower mantle related to decarbonation and dehydration of slab crust and mantle.

Hydrous fluids/melts and the origin of meta-peridotitic inclusions. The discovery of a hydrous ringwoodite (~1.5 wt% H_2O) inclusion in a diamond from Juina, Brazil, provides primary evidence for the involvement of H_2O-rich fluids in sublithospheric diamond genesis (Pearson et al. 2014), although only one such inclusion has been identified to date. Crystallographic data indicate an Mg# of 0.75 ± 0.2, and the inclusion co-occurs with a $CaSiO_3$-rich inclusion with a breyite structure, presumably of the low-Ti variety due to a lack of evidence for an exsolved $CaTiO_3$ phase. Thus, the association appears nominally meta-peridotitic. Further evidence for the role of an H_2O-rich peridotitic association comes from exsolved brucite and magnesioferrite in a composite ferropericlase (Mg# = 0.84) inclusion from Juina (Brazil).

Relatively high levels of boron (reaching up to a few ppm) in blue (Type IIb) diamonds that host $MgSiO_3$-rich phases, $CaSiO_3$-rich phases, SiO_2 and ferropericlase inclusions, are postulated to result from dehydration of post-serpentine minerals on the basis of the high-partition coefficient for boron in serpentine during seawater alteration (Smith et al. 2018). Inclusions of ferropericlase, $MgSiO_3$-rich phases, $CaSiO_3$-rich phases, SiO_2, and CF- or NAL-phase in Type IIb diamonds have been found to have a thin layer of methane ± hydrogen fluid coexisting alongside the solid phases within the inclusion cavity, tentatively suggesting the involvement of a hydrous component in diamond growth (Smith et al. 2018). The co-occurring phases reported in Type IIb diamonds also appear to be part of a meta-peridotitic association although chemical analyses were not reported. Evidence for the role of an H_2O-rich basaltic association comes from reports of micro- or nano-inclusions of phase Egg and δ-AlOOH (Wirth et al. 2007; Kaminsky 2017).

Figure 25 shows a representative phase diagram for hydrous peridotite that, together with modeled pressure–temperature paths at the slab Moho for modern subduction zones, can be used to assess the fate of water in the oceanic lithospheric mantle as it subducts into the transition zone. As pointed out by previous workers, retaining water in subducted lithosphere requires that temperatures in the slab mantle remain below the temperature minimum (~ 7 GPa and 700°C) along the dehydration curve where antigorite and 10 Å phase (±Mg-sursassite) remain stable (Iwamori 2004; Komabayashi et al. 2004; Shirey et al. 2021), which has been referred to as a "choke point" (Iwamori 2004). Estimates for the water storage capacity in antigorite-bearing slab mantle is about 4–5 wt% (Iwamori 2004; Komabayashi and Omori 2006), whereas 10 Å phase-bearing (±Mg-sursassite) mantle assemblages have storage capacity of ~1–2 wt% H_2O (Iwamori 2004; Fumagalli and Poli 2005). Warm slabs have temperatures higher than the choke point leading to dehydration of slab mantle at depths shallower than ~250 km, and such slabs are unlikely to transport significant amounts of water deeper into the mantle either in basaltic crust or peridotitic lithosphere (Okamoto and Maruyama 2004; van Keken et al. 2011; Shirey et al. 2021). However, cooler slabs have P–T paths at the Moho and in the even cooler interior portions of the lithosphere that can remain well below the choke point. Depending on the efficiency of hydration of mantle lithosphere near the surface, cooler slabs can potentially transport as much 4–5 wt% water deeper into the mantle, at least locally, in serpentinized regions formed in deep fractures related to slab bending near the Earth's surface (Faccenda 2014). In colder slabs antigorite transforms at ~250 km and deeper to a series of dense hydrous magnesium silicate phases (DHMS) that in mantle peridotite compositions have the capacity to store at least 5 wt% water and potentially more than 10 wt% (Iwamori 2004).

Water retention in DHMS phases in subducting mantle lithosphere has been postulated in a number of previous studies (Thompson 1992; Frost 1999; Poli and Schmidt 2002; Iwamori 2004; Ohtani et al. 2004; Omori et al. 2004; Harte 2010; van Keken et al. 2011; Ohtani 2015; Maurice et al. 2018). As described above, most slabs are expected to slow down and deform in the transition zone (Bina 1997; Billen 2008). During this stagnation H_2O-bearing slabs will heat by conduction before descending into the lower mantle. Figure 25 illustrates that heating by only a few hundred degrees in the transition zone, which can occur in an ~10 m.y. timeframe (Shirey et al. 2021), would result in breakdown of DHMS phases in the slab mantle at ~1200–1300 °C to wadsleyite or ringwoodite-bearing assemblages and a hydrous fluid.

Wadselyite- and ringwoodite-bearing mantle can accommodate ~1–2 wt% water but a free fluid phase is expected for more water rich-regions of slab mantle. If slabs do not heat sufficiently in the transition zone to dehydrate DHMS phases, dehydration is unavoidable at ~ 700–800 km due to another deep trough, or second 'choke point', as they penetrate into the lower mantle. Depending on temperature, phase D, superhydrous phase B or ringwoodite will transform into a nominally anhydrous assemblage of bridgmanite, Ca-silicate perovskite and ferropericlase with a much lower bulk water storage capacity (< ~0.1 wt%) (Fu et al. 2019), possibly resulting in a hydrous melt at the top of the lower mantle (Schmandt et al. 2014; Ohtani 2015, 2020; Walter et al. 2015).

The composition of H_2O-rich, supercritical fluids or melts released at transition zone and lower mantle depths are poorly known but should have a considerable dissolved silicate component derived from either meta-peridotitic or meta-basaltic mantle sources, being well beyond their second critical endpoints (Mibe et al. 2007, 2011; Wang et al. 2020). Such fluids may also have a dissolved carbon component acquired from mantle peridotite or oceanic crust. Precipitation of diamond and inclusions may occur through subsequent reaction as fluids migrate within the slab and potentially out of the slab (Harte 2010). The meta-peridotitic association of low-Al $MgSiO_3$-rich phases, low-Ti $CaSiO_3$-rich phases and ferropericlase may possibly be best explained by crystallization involving such H_2O-rich fluids/melts at low-temperature in subducted lithospheric mantle and especially in a depleted peridotite composition (e.g., harzburgite) (Harte 2010; Smith et al. 2018; Shirey et al. 2021).

Figure 16 illustrates that at ~1200 °C, where dehydration and fluid release is expected to occur, assemblages are dominated by ringwoodite, akimotoite, bridgmanite, Ca-perovskite, garnet and ferropericlase. The generally low Mg content of low-Ti $CaSiO_3$-rich phases and the generally low-Al and low-Ca contents of $MgSiO_3$ inclusions may indicate equilibrium and crystallization from cool, hydrous fluids or melts carrying dissolved peridotitic components. This may either reflect equilibrium assemblages of Ca-silicate perovskite and akimotoite at the base of the transition zone or relatively low-temperature equilibration between Ca-perovskite and bridgmanite where the solvus results in low levels of solid solution (Irifune et al. 2000). Such low temperatures may also explain the co-occurrence of ferropericlase and stishovite.

The role of Fe–Ni–S–C metallic melts. Iron-rich metal and sulfide inclusions have been reported in diamonds containing sublithospheric inclusions (Bulanova et al. 2010; Kaminsky and Wirth 2011; Smith and Kopylova 2014; Smith et al. 2016b, 2018). Bulanova et al. (2010) reported a metallic iron phase co-occurring in a diamond containing a majoritic garnet, and composite inclusions interpreted as retrograde CAS-phase and K-hollandite, and also observed low-Ni (<3 wt%) pyrrhotite inclusions co-occurring with Ti-rich $CaSiO_3$, majoritic garnet and SiO_2 inclusions in seven diamonds from the Collier-4 kimberlite, Juina (Brazil). Kaminsky and Wirth (2011) reported iron carbides (Fe_3C, Fe_2C and $Fe_{23}C_6$) associated with native iron, also in a diamond from the Juina area, and although not occurring with other sublithospheric inclusions, they concluded a sublithospheric origin based on phase relations in the Fe–C system.

Smith et al. (2016b) reported that many high-quality, Type IIa, gem diamonds, exemplified by the Cullinan, Constellation, and Koh-i-Noor, commonly contain iron-nickel-carbon-sulfur inclusions. Metallic inclusions have been found in 67 out of 83 diamonds in the so-called CLIPPIR suite (Cullinan-like, inclusion-poor, relatively pure, irregularly shaped, and resorbed), and some of these diamonds also contain majoritic garnet or $CaSiO_3$-rich (including Ti-rich $CaSiO_3$) phases which, based on the arguments discussed above, indicate a sublithospheric origin (Smith et al. 2016b, 2017, 2021). A thin fluid layer of methane ± hydrogen was also found associated with the metallic inclusions likely dissolved in the original iron melt under reducing conditions. Smith et al. (2018) also report on rare metallic phases similar to those common in the CLIPPIR suite in the boron-bearing (Type IIb) suite of sublithospheric diamonds.

These diamonds contain a wide range of inclusion types with $CaSiO_3$-phases being the most common, but also including majoritic garnet, SiO_2, and possibly CF or NAL phase in a diamond containing a metallic phase. Smith et al. (2016b) interpret the metallic inclusions as the solidified products of a metallic liquid phase in the deep mantle and suggested strong N partitioning into the melt phase, which may explain the characteristically low nitrogen content in CLIPPIR diamonds and perhaps in sublithospheric diamonds more generally (Smith and Kopylova 2014).

Sublithospheric diamonds containing Fe-rich metal alloy and sulfide inclusions are also generally characterized by isotopically variable and often extremely light carbon ($\delta^{13}C$ from −26.9 to −3.8 ‰ in CLIPPIR diamonds; $\delta^{13}C$ −26 to −8‰ in Collier-4 diamonds). Although the number of metal/sulfide-bearing diamonds co-occurring with sublithospheric silicate inclusions is small, the suite observed to date contains phases suggestive of basaltic. A recent study of the Fe isotopic composition of the metallic inclusions reveals a strikingly heavy isotopic signature ($\delta^{56}Fe$ = 0.79 to 0.90‰) thought to be inherited from magnetite and/or Fe–Ni alloys precipitated during serpentinization of oceanic peridotite (Smith et al. 2021). This heavy iron signature is suggestive that the metallic liquid trapped in CLIPPIR diamonds has a lithological connection to subducted, serpentinized peridotite.

SUMMARY AND PERSPECTIVES

On the basis of an analysis of published geochemical data of predominant silicate and oxide inclusions in sublithospheric diamonds and building upon observations and ideas that have been discussed in the literature for over three decades, a framework emerges for understanding processes occurring in the deep mantle related to the subduction of lithospheric plates. Few inclusions have major and trace element chemistry consistent with expectations for primitive meta-peridotitic mantle assemblages at upper mantle, transition zone or lower mantle pressures and temperatures, and we conclude that sublithospheric diamonds do not typically incorporate minerals representative of ambient mantle.

Generally speaking, the inclusions define two populations that appear to reflect different source lithologies, or more specifically, the fluids and melts derived from and/or that interact with those lithologies. Consistent with previous interpretations we assign the two populations of inclusions to meta-peridotitic and meta-basaltic varieties, with the former broadly representative of peridotitic, harzburgitic and dunitic lithologies and the latter including basaltic or pyroxenitic ones. The host diamonds themselves have carbon isotopic compositions that also reveal a distinction among these groups, with meta-peridotitic inclusions hosted by diamonds with a restricted range of predominantly isotopically heavier, mantle-like carbon, whereas the meta-basaltic group exhibits a wider range that extends to isotopically light carbon associated with subducted oceanic crust.

The meta-peridotite group includes low-Al $MgSiO_3$, low-Ti $CaSiO_3$, ferropericlase, high-Cr majoritic garnet, olivine and low-Na clinopyroxene inclusions. Low-Al $MgSiO_3$ (former bridgmanite and/or akimotoite), low-Ti $CaSiO_3$ (former Ca-silicate perovskite) and high Mg# ferropericlase are generally consistent with diamond formation in the shallow lower mantle or deep transition zone, and the observed inclusion suite provides evidence for equilibration at low temperatures (e.g., low Mg in Ca-perovskite; low Ca in $MgSiO_3$; the ferropericlase plus stishovite association) perhaps in the range of 1000–1200 °C. Many inclusions also indicate a depleted source lithology (e.g., low Al, low Ca, high Mg# in some $MgSiO_3$; low Cr, Al and Na in ferropericlase), which when combined with low equilibration temperatures suggests an origin related to depleted slab mantle lithosphere.

Harte (2010) summarized many of these features and suggested an origin related to dehydration of subducted lithospheric mantle near the base of the transition zone, and phase relations for dehydration in subducted mantle support this hypothesis. The heavy iron isotopes in iron-alloy inclusions that may be related to magnetite formation during serpentinization and the generally mantle-like carbon isotopic compositions of the diamonds hosting the meta-peridotitic inclusions all support this hypothesis. This may indicate that slab-derived hydrous fluids acquire their carbon from the mantle portion of the down-going slab or from the ambient mantle, with little or no interaction with subducted oceanic crust.

The presence of methane in some inclusions is suggestive of reduced fluids possibly equilibrated with metal alloy phases. The high-Cr majoritic garnets also have a meta-peridotite chemistry but their apparent formation pressures indicate a predominantly upper mantle origin unrelated to the deeper inclusion assemblage, suggesting these garnet inclusions may have formed in the deepest portions of the lithospheric mantle. Low-Na clinopyroxene, with their unusual co-occurrences with ferropericlase and Ca-rich phases, also remain enigmatic but seemingly reflect an upper mantle and transition zone origin.

The meta-basaltic group is characterized by low-Cr garnet, high-Ti $CaSiO_3$, high-Al $MgSiO_3$, high-Na clinopyroxene as well as rare CF and NAL inclusions (Fig. 1). These inclusions have major element compositions akin to high pressure phases in meta-basaltic to meta-pyroxenitic lithologies. Majoritic garnet barometry places their origin throughout the deep upper mantle to the transition zone, which is consistent with phase equilibrium constraints on the origin of high-Ti $CaSiO_3$ inclusions. In contrast, high-Al $MgSiO_3$, CF and NAL inclusions provide evidence of a shallow lower mantle assemblage. Thus, the meta-basaltic group apparently forms over a wide depth range.

Meta-basaltic inclusions have trace element concentrations that are generally enriched over levels expected in MORB, sometimes by many orders of magnitude, with elemental abundance patterns linking them to deeply subducted oceanic crust. Low-degree melts from oceanic crust, possibly carbonatitic, are implicated in their origin and diamond formation may occur through reduction within slab mantle or ambient mantle through redox freezing. Low temperatures of equilibration are indicated by the high-Ti $CaSiO_3$ inclusions (low-Mg content) consistent with melting of carbonated/hydrated oceanic crust at ~1200 °C as constrained by melting phase relations. Many majoritic garnet and clinopyroxene compositions indicate an origin related to meta-pyroxenite and these may represent hybrid reaction products when melts from subducted oceanic crust infiltrate and react with the slab mantle or ambient mantle. The carbon isotopic compositions of the diamond hosts are consistent with this scenario and may reflect mixing of carbon sourced from subducted oceanic crust and peridotitic mantle sources.

The common theme among models for sublithospheric diamond and inclusion formation is the key role of subducted lithosphere, and particularly the fluids and melts that are derived from lithologies in the slab that infiltrate and react with their surroundings both within and external to the slab, precipitating diamonds and their inclusions. The overall narrative presented here for the generation of sublithospheric diamonds related to subducted slab lithosphere stagnating in the transition zone and shallow lower mantle is reminiscent of the megalith model of Ringwood (1991), an observation echoed in many studies over the intervening years. Yet many questions remain as we continue to develop our understanding of sublithospheric diamond and inclusion formation and what these samples reveal in detail about deep mantle processes.

In this review we have taken a global perspective, highlighting the clear similarities within inclusion groups that span across all sampled cratons. However, processes related to diamond and inclusion formation will also likely be dependent on the specific tectonic and geodynamic setting of subduction, and regional differences can be expected that can only become readily apparent with larger, more diverse data sets. Some outstanding questions that can be addressed in future studies might include:

1. What is the actual distribution of co-occurring phases in sublithospheric diamonds? In many cases, especially in pioneering studies where cracking diamonds to retrieve inclusions was a common practice, the co-occurring phases within individual diamonds are unknown or unreported creating data biases. Future studies should concentrate on identifying all major inclusions co-occurring in single diamonds. This requires a combination of techniques including X-ray diffraction and tomography, especially at synchrotron facilities (Wenz et al. 2019). Diamonds should be fully characterized by cutting and polishing to reveal inclusions, ideally with full major and trace element chemical analysis of inclusions and isotopic analysis of the host diamonds.

2. How are iron-rich ferropericlase inclusions formed and at what depth? Are these lower mantle or upper mantle phases? Do they represent remnants of the redox process during interaction of melts/fluids with the mantle during diamond crystallization? What is the source of the pronounced Ba and Y anomalies? More data on the redox state of the iron-rich inclusions, trace element data and iron isotopic compositions of inclusions are needed to understand these important and abundant inclusions.

3. What is the true majoritic garnet pressure distribution? Although reliable majorite barometers are available and a large dataset reveals a range of pressures from the asthenosphere to the transition zone, majoritic garnet inclusions can only provide accurate depths of origin if their bulk chemistry is accurately known. The common unmixing of clinopyroxene in sublithospheric garnet inclusions currently masks this information. Future studies of majoritic garnet inclusions should concentrate on reconstructing bulk compositions through approaches such as X-ray tomography, sequential sectioning and analysis of all unmixed components.

4. What is the upwelling history of composite inclusions? Unmixing of phases is common in sublithospheric inclusions but the uplift history remains a mystery in most cases. What is their final residence depth and what is the uplift mechanism (i.e., solid-state upwelling in a mantle plume; transport in a percolating melt) remain important unresolved questions.

5. What are the ages of diamond and inclusion formation and can they be linked in space and time to paleo-subduction? How do they relate to the timing of ascent and volcanic emplacement at surface? There is scarce information about the age of sublithospheric diamond formation, yet this is critical for placing models within a geodynamic and tectonic context. Dating of small sulfide grains using Re–Os and $CaSiO_3$-rich phases using U–Pb, although tremendously challenging, likely represent the best opportunity to provide key age constraints.

6. Fluids and melts generated by subducting slab lithosphere are the likely media of diamond formation and inclusion equilibration, yet little is known about the phase equilibria or composition of such melts. What are the compositions of the deep melts and fluids from which the diamonds precipitate and the inclusions likely equilibrate? What reactions occur to form diamonds and their inclusions? Experiments on a range of compositions with mixed volatile phases are required to develop a firmer understanding of the fluids, melts and reactions that form sublithospheric diamonds and their inclusions.

ACKNOWLEDGEMENTS

The tables associated with this chapter can be found at https://doi.org/10.5683/SP3/LIVK1K (Walter et al. 2022). We would like to thank Galina Bulanova, Antony Burnham, Rick Carlson, Ben Harte, Dan Howell, Simon Kohn, Nico Kueter, Sami Mikhail, Fabrizio Nestola, Peng Ni, Graham Pearson, Anat Shahar, Steve Shirey, Chris Smith, Lara Speich, Thomas Stachel, Peter van Keken and Lara Wagner for the many conversations and insights that helped shaped this review. Special thanks to Thomas Stachel for access to his incredible inclusion database. We thank Ben Harte, Thomas Stachel, Karen Smit and Graham Pearson for constructive reviews that improved the clarity of ideas and presentation in this chapter.

REFERENCES

Ackerson MR, Tailby ND, Watson EB (2017a) XAFS spectroscopic study of Ti coordination in garnet. Am Mineral 102:173–183

Ackerson MR, Watson EB, Tailby ND, Spear FS (2017b) Experimental investigation into the substitution mechanisms and solubility of Ti in garnet. Am Mineral 102:158–172

Akaogi M, Akimoto S (1977) Pyroxene–garnet solid-solution equilibria in systems $Mg_4Si_4O_{12}$–$Mg_3Al_2Si_3O_{12}$ and $Fe_4Si_4O_{12}$–$Fe_3Al_2Si_3O_{12}$ at high-pressures and temperatures. Phys Earth Planet Sci 15:90–106

Akaogi M, Akimoto S (1979) High-pressure phase-equilibria in a garnet lherzolite, with special reference to Mg^{2+}–Fe^{2+} partitioning among constituent minerals. Phys Earth Planet Sci 19:31–51

Anand M, Taylor LA, Misra KC, Carlson WD, Sobolev NV (2004) Nature of diamonds in Yakutian eclogites: views from eclogite tomography and mineral inclusions in diamonds. Lithos 77:333–348

Andrault D, Bolfan-Casanova N (2001) High-pressure phase transformations in the $MgFe_2O_4$ and Fe_2O_3–$MgSiO_3$ systems. Phys Chem Mineral 28:211–217

Anzolini C, Prencipe M, Alvaro M, Romano C, Vona A, Lorenzon S, Smith EM, Brenker FE, Nestola F (2018) Depth of formation of super-deep diamonds: Raman barometry of $CaSiO_3$-walstromite inclusions. Am Mineral 103:69–74

Anzolini C, Nestola F, Mazzucchelli ML, Alvaro M, Nimis P, Gianese A, Morganti S, Marone F, Campione M, Hutchison MT, Harris JW (2019) Depth of diamond formation obtained from single periclase inclusions. Geology 47:219–222

Armstrong LS, Walter MJ (2012) Tetragonal almandine pyrope phase (TAPP): retrograde Mg-perovskite from subducted oceanic crust? Eur J Mineral 24:587–597

Armstrong LS, Walter MJ, Tuff JR, Lord OT, Lennie AR, Kleppe AK, Clark SM (2012) Perovskite phase relations in the system CaO-MgO-TiO_2-SiO_2 and implications for deep mantle lithologies. J Petrol 53:611–635

Beyer C, Frost DJ (2017) The depth of sub-lithospheric diamond formation and the redistribution of carbon in the deep mantle. Earth Planet Sci Lett 461:30–39

Billen MI (2008) Modeling the dynamics of subducting slabs. Annu Rev Earth Planet Sci 36:325–356

Bina CR (1997) Patterns of deep seismicity reflect buoyancy stresses due to phase transitions. Geophys Res Lett 24:3301–3304

Boyd SR, Mattey DP, Pillinger CT, Milledge HJ, Mendelssohn M, Seal M (1987) Multiple growth events during diamond genesis - an integrated study of carbon and nitrogen isotopes and nitrogen aggregation state in coated stones. Earth Planet Sci Lett 86:341–353

Brenker FE, Stachel T, Harris JW (2002) Exhumation of lower mantle inclusions in diamond: ATEM investigation of retrograde phase transitions, reactions and exsolution. Earth Planet Sci Lett 198:1–9

Brenker FE, Vincze L, Vekemans B, Nasdala L, Stachel T, Vollmer C, Kersten M, Somogyi A, Adams F, Joswig W, Harris JW (2005) Detection of a Ca-rich lithology in the Earth's deep (> 300 km) convecting mantle. Earth Planet Sci Lett 236:579–587

Brenker FE, Nestola F, Brenker L, Peruzzo L, Harris JW (2021) Origin, properties, and structure of breyite: The second most abundant mineral inclusion in super-deep diamonds. Am Mineral 106:38–43

Brey GP, Bulatov V, Girnis A, Harris JW, Stachel T (2004) Ferropericlase—a lower mantle phase in the upper mantle. Lithos 77:655–663

Brey GP, Bulatov VK, Girnis AV (2008) Geobarometry for peridotites: Experiments in simple and natural systems from 6 to 10 GPa. J Petrol 49:3–24

Brey GP, Girnis AV, Bulatov VK, Hofer HE, Gerdes A, Woodland AB (2015) Reduced sediment melting at 7.5–12 GPa: phase relations, geochemical signals and diamond nucleation. Contrib Mineral Petrol 170:18

Bulanova GP (1995) The formation of diamond. J Geochem Explor 53:1–23

Bulanova GP, Walter MJ, Smith CB, Kohn SC, Armstrong LS, Blundy J, Gobbo L (2010) Mineral inclusions in sublithospheric diamonds from Collier 4 kimberlite pipe, Juina, Brazil: subducted protoliths, carbonated melts and primary kimberlite magmatism. Contrib Mineral Petrol 160:489–510

Bulatov VK, Brey GP, Girnis AV, Gerdes A, Hofer HE (2014) Carbonated sediment–peridotite interaction and melting at 7.5–12 GPa. Lithos 200:368–385

Bulatov VK, Girnis AV, Brey GP, Woodland AB, Hofer HE (2019) Ferropericlase crystallization under upper mantle conditions. Contrib Mineral Petrol 174:45

Burnham AD, Thomson AR, Bulanova GP, Kohn SC, Smith CB, Walter MJ (2015) Stable isotope evidence for crustal recycling as recorded by superdeep diamonds. Earth Planet Sci Lett 432:374–380

Burnham AD, Bulanova GP, Smith CB, Whitehead SC, Kohn SC, Gobbo L, Walter MJ (2016) Diamonds from the Machado River alluvial deposit, Rondonia, Brazil, derived from both lithospheric and sublithospheric mantle. Lithos 265:199–213

Cartigny P (2005) Stable isotopes and the origin of diamond. Elements 1:79–84

Cartigny P, Palot M, Thomassot E, Harris JW (2014) Diamond formation: A stable isotope perspective. Annu Rev Earth Planet Sci 42:699–732

Chatterjee ND, Johannes W, Leistner H (1984) The system CaO–Al_2O_3–SiO_2–H_2O—New phase-equilibria data, some calculated phase-relations, and their petrological applications. Contrib Mineral Petrol 88:1–13

Collerson KD, Williams Q, Kamber BS, Omori S, Arai H, Ohtani E (2010) Majoritic garnet: A new approach to pressure estimation of shock events in meteorites and the encapsulation of sub-lithospheric inclusions in diamond. Geochim Cosmochim Acta 74:5939–5957

Corgne A, Armstrong LS, Keshav S, Fei YW, McDonough WF, Minarik WG, Moreno K (2012) Trace element partitioning between majoritic garnet and silicate melt at 10–17 GPa: Implications for deep mantle processes. Lithos 148:128–141

Czas J, Stachel T, Pearson DG, Stern RA, Read GH (2018) Diamond brecciation and annealing accompanying major metasomatism in eclogite xenoliths from the Sask Craton, Canada. Mineral Petrol 112:311–323

Dalou C, Koga KT, Hammouda T, Poitrasson F (2009) Trace element partitioning between carbonatitic melts and mantle transition zone minerals: Implications for the source of carbonatites. Geochim Cosmochim Acta 73:239–255

Dasgupta R, Hirschmann MM, Withers AC (2004) Deep global cycling of carbon constrained by the solidus of anhydrous, carbonated eclogite under upper mantle conditions. Earth Planet Sci Lett 227:73–85

Davies RM, Griffin WL, O'Reilly SY, Andrew AS (2003) Unusual mineral inclusions and carbon isotopes of alluvial diamonds from Bingara, eastern Australia. Lithos 69:51–66

Deines P (1980) The carbon isotopic composition of diamonds—Relationship to diamond shape, color, occurrence and vapor composition. Geochim Cosmochim Acta 44:943–961

Deines P, Harris JW, Gurney JJ (1991) The carbon isotopic composition and nitrogen-content of lithospheric and asthenospheric diamonds from the Jagersfontein and Koffiefontein kimberlite, South Africa. Geochim Cosmochim Acta 55:2615–2625

Drewitt JWE, Walter MJ, Zhang HL, McMahon SC, Edwards D, Heinen BJ, Lord OT, Anzellini S, Kleppe AK (2019) The fate of carbonate in oceanic crust subducted into earth's lower mantle. Earth Planet Sci Lett 511:213–222

Duffy T, Madhusudhan N, Lee KKM (2015) Mineralogy of super-earth planets. *In*: Treatise on Geophysics. Elsevier, p 149–178

Dymshits AM, Bobrov AV, Bindi L, Litvin YA, Litasov KD, Shatskiy AF, Ohtani E (2013) Na-bearing majoritic garnet in the $Na_2MgSi_5O_{12}$–$Mg_3Al_2Si_3O_{12}$ join at 11–20 GPa: Phase relations, structural peculiarities and solid solutions. Geochim Cosmochim Acta 105:1–13

Faccenda M (2014) Water in the slab: A trilogy. Tectonophysics 614:1–30

Fei Y, Wang Y, Finger LW (1996) Maximum solubility of FeO in (Mg,Fe)SiO_3-perovskite as a function of temperature at 26 GPa: Implication for FeO content in the lower mantle. J Geophys Res-Solid Earth 101:11525–11530

Fischer RA, Campbell AJ, Chidester BA, Reaman DM, Thompson EC, Pigott JS, Prakapenka VB, Smith JS (2018) Equations of state and phase boundary for stishovite and $CaCl_2$-type SiO_2. Am Mineral 103:792–802

Frost DJ (1999) The stability of dense hydrous magnesium silicates in Earth's transition zone and lower mantle. *In*: Mantle Petrology: Field Observations and High-Pressure Experimentation A Tribute to Francis R (Joe) Boyd. Vol 6. Fei Y, Bertka CM, Mysen BO (eds). The Geochemical Society, Houston, TX, p 283–296

Frost DJ, McCammon CA (2008) The redox state of Earth's mantle. Annu Rev Earth Planet Sci 36:389–420

Fu S, Yang J, Karato SI, Vasiliev A, Presniakov MY, Gavriliuk AG, Ivanova AG, Hauri EH, Okuchi T, Purevjav N, Lin JF (2019) Water concentration in single-crystal (Al,Fe)-bearing bridgmanite grown from the hydrous melt: Implications for dehydration melting at the topmost lower mantle. Geophys Res Lett 46:10346–10357

Fumagalli P, Poli S (2005) Experimentally determined phase relations in hydrous peridotites to 6.5 GPa and their consequences on the dynamics of subduction zones. J Petrol 46:555–578

Gale A, Dalton CA, Langmuir CH, Su YJ, Schilling JG (2013) The mean composition of ocean ridge basalts. Geochem Geophys Geosyst 14:489–518

Ghosh S, Ohtani E, Litasov KD, Terasaki H (2009) Solidus of carbonated peridotite from 10 to 20 GPa and origin of magnesiocarbonatite melt in the Earth's deep mantle. Chem Geol 262:17–28

Ghosh S, Litasov K, Ohtani E (2014) Phase relations and melting of carbonated peridotite between 10 and 20 GPa: a proxy for alkali- and CO_2-rich silicate melts in the deep mantle. Contrib Mineral Petrol 167:964

Grassi D, Schmidt MW (2011) Melting of carbonated pelites at 8–13 GPa: generating K-rich carbonatites for mantle metasomatism. Contrib Mineral Petrol 162:169–191

Grew ES, Locock AJ, Mills SJ, Galuskina IO, Galuskin EV, Halenius U (2013) Nomenclature of the garnet supergroup. Am Mineral 98:785–810

Haggerty SE (1986) Diamond genesis in a multiply-constrained model. Nature 320:34–37

Haggerty SE, Fung AT, Burt DM (1994) Apatite, phosphorus and titanium in eclogitic garnet from the upper-mantle. Geophys Res Lett 21:1699–1702

Hammouda T (2003) High-pressure melting of carbonated eclogite and experimental constraints on carbon recycling and storage in the mantle. Earth Planet Sci Lett 214:357–368

Harlow GE (1998) The Nature of Diamonds. Cambridge University Press, Cambridge, UK

Harris J, Gurney J (1979) Inclusions in diamonds. *In*: Properties of Diamond. Field JE (ed) Academic Press, London

Harris J, Hutchison MT, Hursthouse M, Light M, Harte B (1997) A new tetragonal silicate mineral occurring as inclusions in lower-mantle diamonds. Nature 387:486–488

Harte B (2010) Diamond formation in the deep mantle: the record of mineral inclusions and their distribution in relation to mantle dehydration zones. Mineral Mag 74:189–215

Harte B, Cayzer N (2007) Decompression and unmixing of crystals included in diamonds from the mantle transition zone. Phys Chem Mineral 34:647–656

Harte B, Harris JW (1994) Lower mantle mineral associations preserved in diamonds. Mineral Mag A58:384–385

Harte B, Richardson S (2012) Mineral inclusions in diamonds track the evolution of a Mesozoic subducted slab beneath West Gondwanaland. Gondwana Res 21:236–245

Harte B, Harris JW, Hutchison MT, Watt GR, Wilding MC (1999) Lower mantle mineral associations in diamonds from Sao Luiz, Brazil. *In*: Mantle Petrology: Field Observations and High Pressure Experimentation, A Tribute to Francis R (Joe) Boyd. Vol 6. Fei Y, Mysen BO, Bertka CM, (eds). The Geochemical Society, Houston, p 125–153

Hayman PC, Kopylova MG, Kaminsky FV (2005) Lower mantle diamonds from Rio Soriso (Juina area, Mato Grosso, Brazil). Contrib Mineral Petrol 149:430–445

Herzberg C, Zhang JZ (1996) Melting experiments on anhydrous peridotite KLB-1: Compositions of magmas in the upper mantle and transition zone. J Geophys Res-Solid Earth 101:8271–8295

Hirose K (2002) Phase transitions in pyrolitic mantle around 670-km depth: Implications for upwelling of plumes from the lower mantle. J Geophys Res-Solid Earth 107(B4):ECV-3

Hirose K, Fei YW (2002) Subsolidus and melting phase relations of basaltic composition in the uppermost lower mantle. Geochim Cosmochim Acta 66:2099–2108

Hoernle K, Tilton G, Le Bas MJ, Duggen S, Garbe-Schonberg D (2002) Geochemistry of oceanic carbonatites compared with continental carbonatites: mantle recycling of oceanic crustal carbonate. Contrib Mineral Petrol 142:520–542

Hutchison M (1997) Constitution of the Deep Transition Zone and Lower Mantle shown by Diamonds and their Inclusions. PhD, University of Edinburgh

Hutchison M, Cartigny P, Harris J (1999) Carbon and nitrogen compositions and physical characteristics of transition zone and lower mantle diamonds from São Luiz, Brazil. *In*: Proc VII Int Kimberlite Conf. Vol 2. Gurney JJ, Gurney JL, Pascoe MD, Richardson SH, (eds). Red Roof Designs, Cape Town, p 372–382

Hutchison MT, Hursthouse MB, Light ME (2001) Mineral inclusions in diamonds: associations and chemical distinctions around the 670-km discontinuity. Contrib Mineral Petrol 142:119–126

Ickert RB, Stachel T, Stern RA, Harris JW (2015) Extreme O-18-enrichment in majorite constrains a crustal origin of transition zone diamonds. Geochem Perspect Lett 1:65–73

Irifune T (1987) An experimental investigation of the pyroxene garnet transformation in a pyrolite composition and its bearing on the constitution of the mantle. Phys Earth Planet Sci 45:324–336

Irifune T (1994) Absence of an aluminous phase in the upper part of the earths lower mantle. Nature 370:131–133

Irifune T, Ringwood AE (1987) Phase-transformations in a harzburgite composition to 26 GPa—Implications for dynamical behavior of the subducting slab. Earth Planet Sci Lett 86:365–376

Irifune T, Ringwood AE (1993) Phase-transformations in subducted oceanic-crust and buoyancy relationships at depths of 600–800 km in the mantle. Earth Planet Sci Lett 117:101–110

Irifune T, Sekine T, Ringwood AE, Hibberson WO (1986) The eclogite–garnetite transformation at high-pressure and some geophysical implications. Earth Planet Sci Lett 77:245–256

Irifune T, Hibberson WO, Ringwood AE (1989) Eclogite–garnetite transformation at high pressure and its bearing on the occurrence of garnet inclusions in diamond. *In*: Kimberlites and Related Rocks. Vol GSA Spec Publ 14. Ross J (ed) Blackwell, Carlton, p 877–882

Irifune T, Ringwood AE, Hibberson WO (1994) Subduction of continental-crust and terrigenous and pelagic sediments—An experimental-study. Earth Planet Sci Lett 126:351–368

Irifune T, Miyashita M, Inoue T, Ando J, Funakoshi K, Utsumi W (2000) High-pressure phase transformation in $CaMgSi_2O_6$ and implications for origin of ultra-deep diamond inclusions. Geophys Res Lett 27:3541–3544

Irifune T, Shinmei T, McCammon CA, Miyajima N, Rubie DC, Frost DJ (2010) Iron partitioning and density changes of pyrolite in earth's lower mantle. Science 327:193–195

Ishii T, Kojitani H, Akaogi M (2011) Post-spinel transitions in pyrolite and Mg_2SiO_4 and akimotoite–perovskite transition in $MgSiO_3$: Precise comparison by high-pressure high-temperature experiments with multi-sample cell technique. Earth Planet Sci Lett 309:185–197

Ishii T, Kojitani H, Akaogi M (2012) High-pressure phase transitions and subduction behavior of continental crust at pressure-temperature conditions up to the upper part of the lower mantle. Earth Planet Sci Lett 357:31–41

Ishii T, Kojitani H, Akaogi M (2018) Phase relations and mineral chemistry in pyrolitic mantle at 1600–2200 degrees C under pressures up to the uppermost lower mantle: Phase transitions around the 660-km discontinuity and dynamics of upwelling hot plumes. Phys Earth Planet Sci 274:127–137

Ishii T, Kojitani H, Akaogi M (2019) Phase relations of harzburgite and MORB up to the uppermost lower mantle conditions: precise comparison with pyrolite by multisample cell high-pressure experiments with implication to dynamics of subducted slabs. J Geophys Res-Solid Earth 124:3491–3507

Ito E, Takahashi E (1987) Melting of peridotite at uppermost lower-mantle conditions. Nature 328:514–517

Ito E, Takahashi E, Matsui Y (1984) The mineralogy and chemistry of the lower mantle—An implication of the ultrahigh-pressure phase-relations in the system MgO–FeO–SiO_2. Earth Planet Sci Lett 67:238–248

Iwamori H (2004) Phase relations of peridotites under H_2O-saturated conditions and ability of subducting plates for transportation of H_2O. Earth Planet Sci Lett 227:57–71

Joswig W, Stachel T, Harris JW, Baur WH, Brey GP (1999) New Ca-silicate inclusions in diamonds—Tracers from the lower mantle. Earth Planet Sci Lett 173:1–6

Kaminsky F (2012) Mineralogy of the lower mantle: A review of 'super-deep' mineral inclusions in diamond. Earth Sci Rev 110:127–147

Kaminsky FV (2017) Lower-mantle mineral associations. *In*: Earth's Lower Mantle: Composition and Structure. p 23–46

Kaminsky FV, Wirth R (2011) Iron carbide inclusions in lower-mantle diamond from Juina, Brazil. Can Mineral 49:555–572

Kaminsky FV, Zakharchenko OD, Davies R, Griffin WL, Khachatryan-Blinova GK, Shiryaev AA (2001) Superdeep diamonds from the Juina area, Mato Grosso State, Brazil. Contrib Mineral Petrol 140:734–753

Katsura T, Yoneda A, Yamazaki D, Yoshino T, Ito E (2010) Adiabatic temperature profile in the mantle. Phys Earth Planet Sci 183:212–218

Kawamoto T (2004) Hydrous phase stability and partial melt chemistry in H_2O-saturated KLB-1 peridotite up to the uppermost lower mantle conditions. Phys Earth Planet Sci 143:387–395

Kawamoto T, Kanzaki M, Mibe K, Matsukage KN, Ono S (2012) Separation of supercritical slab-fluids to form aqueous fluid and melt components in subduction zone magmatism. PNAS 109:18695–18700

Kessel R, Ulmer P, Pettke T, Schmidt MW, Thompson AB (2005) The water–basalt system at 4 to 6 GPa: Phase relations and second critical endpoint in a K-free eclogite at 700 to 1400 degrees C. Earth Planet Sci Lett 237:873–892

Kesson SE, Fitz Gerald JD, Shelley JMG (1994) Mineral chemistry and density subducted basaltic crust at lower-mantle pressures. Nature 372:767–769

Kesson SE, Fitz Gerald JD, Shelley JMG, Withers RL (1995) Phase-relations, structure and crystal-chemistry of some aluminous silicate perovskites. Earth Planet Sci Lett 134:187–201

Kiseeva ES, Litasov KD, Yaxley GM, Ohtani E, Kamenetsky VS (2013a) Melting and phase relations of carbonated eclogite at 9–21 GPa and the petrogenesis of alkali-rich melts in the deep mantle. J Petrol 54:1555–1583

Kiseeva ES, Yaxley GM, Stepanov AS, Tkalcic H, Litasov KD, Kamenetsky VS (2013b) Metapyroxenite in the mantle transition zone revealed from majorite inclusions in diamonds. Geology 41:883–886

Kiseeva ES, Vasiukov DM, Wood BJ, McCammon C, Stachel T, Bykov M, Bykova E, Chumakov A, Cerantola V, Harris JW, Dubrovinsky L (2018) Oxidized iron in garnets from the mantle transition zone. Nat Geosci 11:144–147

Klein-BenDavid O, Izraeli ES, Hauri E, Navon O (2007) Fluid inclusions in diamonds from the Diavik mine, Canada and the evolution of diamond-forming fluids. Geochim Cosmochim Acta 71:723–744

Klein-BenDavid O, Logvinova AM, Schrauder M, Spetius ZV, Weiss Y, Hauri EH, Kaminsky FV, Sobolev NV, Navon O (2009) High-Mg carbonatitic microinclusions in some Yakutian diamonds-a new type of diamond-forming fluid. Lithos 112:648–659

Komabayashi T, Omori S (2006) Internally consistent thermodynamic data set for dense hydrous magnesium silicates up to 35 GPa, 1600 degrees C: Implications for water circulation in the Earth's deep mantle. Phys Earth Planet Sci 156:89–107

Komabayashi T, Omori S, Maruyama S (2004) Petrogenetic grid in the system MgO-SiO_2-H_2O up to 30 GPa, 1600 degrees C: Applications to hydrous peridotite subducting into the Earth's deep interior. J Geophys Res-Solid Earth 109:B03206

Korolev NM, Kopylova M, Bussweiler Y, Pearson DG, Gurney J, Davidson J (2018) The uniquely high-temperature character of Cullinan diamonds: A signature of the Bushveld mantle plume? Lithos 304:362–373

Kubo A, Suzuki T, Akaogi M (1997) High pressure phase equilibria in the system $CaTiO_3$–$CaSiO_3$: stability of perovskite solid solutions. Phys Chem Mineral 24:488–494

Kuwahara H, Nomura R, Nakada R, Irifune T (2018) Simultaneous determination of melting phase relations of mantle peridotite and mid-ocean ridge basalt at the uppermost lower mantle conditions. Phys Earth Planet Sci 284:36–50

Li XY, Zhang ZG, Lin JF, Ni HW, Prakapenka VB, Mao Z (2018) New High-pressure phase of $CaCO_3$ at the topmost lower mantle: Implication for the deep-mantle carbon transportation. Geophys Res Lett 45:1355–1360

Litasov KD, Ohtani E (2005) Phase relations in hydrous MORB at 18–28 GPa: implications for heterogeneity of the lower mantle. Phys Earth Planet Sci 150:239–263

Liu LG (2002) An alternative interpretation of lower mantle mineral associations in diamonds. Contrib Mineral Petrol 144:16–21

Liu LG, Ringwood AE (1975) Synthesis of a perovskite-type polymorph of $CaSiO_3$. Earth Planet Sci Lett 28:209–211

Liu X, Zhang LF, Hack CA, Zheng HF, Hu XM, Chang LL, He Q (2009a) Effect of water on the partial melting process of some silicate systems: Important implication of the second critical endpoint. Acta Petrologica Sinica 25:3407–3421

Liu Y, Taylor LA, Sarbadhikari AB, Valley JW, Ushikubo T, Spicuzza MJ, Kita N, Ketcham RA, Carlson W, Shatsky V, Sobolev NV (2009b) Metasomatic origin of diamonds in the world's largest diamondiferous eclogite. Lithos 112:1014–1024

Locock AJ (2008) An Excel spreadsheet to recast analyses of garnet into end-member components, and a synopsis of the crystal chemistry of natural silicate garnets. Computers Geosci 34:1769–1780

Luth RW, Stachel T (2014) The buffering capacity of lithospheric mantle: implications for diamond formation. Contrib Mineral Petrol 168:1083

Luth RW, Palyanov YN, Bureau H (2022) Experimental petrology applied to natural diamond growth. Rev Mineral Geochem 88:755–808

Maeda F, Ohtani E, Kamada S, Sakamaki T, Hirao N, Ohishi Y (2017) Diamond formation in the deep lower mantle: a high-pressure reaction of $MgCO_3$ and SiO_2. Sci Rep 7:40602

Mao HK, Chen LC, Hemley RJ, Jephcoat AP, Wu Y, Bassett WA (1989) Stability and equation of state of $CaSiO_3$-perovskite to 134 GPa. J Geophys Res-Solid Earth Planets 94:17889–17894

Maurice J, Bolfan-Casanova N, Padron-Navarta JA, Manthilake G, Hammouda T, Henot JM, Andrault D (2018) The stability of hydrous phases beyond antigorite breakdown for a magnetite-bearing natural serpentinite between 6.5 and 11 GPa. Contrib Mineral Petrol 173:86

McCammon C, Hutchison M, Harris J (1997) Ferric iron content of mineral inclusions in diamonds from Sao Luiz: A view into the lower mantle. Science 278:434–436

McCammon CA, Stachel T, Harris JW (2004) Iron oxidation state in lower mantle mineral assemblages—II. Inclusions in diamonds from Kankan, Guinea. Earth Planet Sci Lett 222:423–434

McDonough WF, Sun SS (1995) The composition of the Earth. Chem Geol 120:223–253

Meyer HOA (1987) Inclusions in diamond. *In*: Mantle xenoliths. Nixon PH (ed) John Wiley & Sons Ltd, Chichester, p 501–522

Mibe K, Kanzaki M, Kawamoto T, Matsukage KN, Fei YW, Ono S (2007) Second critical endpoint in the peridotite–H_2O system. J Geophys Res-Solid Earth 112:B03201

Mibe K, Kawamoto T, Matsukage KN, Fei YW, Ono S (2011) Slab melting versus slab dehydration in subduction-zone magmatism. PNAS 108:8177–8182

Miyajima N, Yagi T, Hirose K, Kondo T, Fujino K, Miura H (2001) Potential host phase of aluminum and potassium in the Earth's lower mantle. Am Mineral 86:740–746

Moore RO, Gurney JJ (1985) Pyroxene solid-solution in garnets included in diamond. Nature 318:553–555

Moore AE, Gurney JJ (1989) Mineral inclusions in diamond from Monastery kimberlite, South Africa. *In*: Kimberlites and Related Rocks. GSA Spec Publ Vol. 14. J Ross et al. (ed) Blackwell, Carlton, p 1029–1041

Moore RO, Otter ML, Rickard RS, Harris JW, Gurney JJ (1986) The occurance of moissanite and ferr-periclase as inclusions in diamond. Geol Soc Aust Abstracts 16:409–411

Moore RO, Gurney JJ, Griffin WL, Shimizu N (1991) Ultra-high pressure garnet inclusions in Monastery diamonds—Trace-element abundance patterns and conditions of origin. Euro J Mineral 3:213–230

Motsamai T, Harris JW, Stachel T, Pearson DG, Armstrong J (2018) Mineral inclusions in diamonds from Karowe Mine, Botswana: super-deep sources for super-sized diamonds? Mineral Petrol 112:169–180

Navon O, Hutcheon ID, Rossman GR, Wasserburg GJ (1988) Mantle-derived fluids in diamond micro-inclusions. Nature 335:784–789

Nestola F, Korolev N, Kopylova M, Rotiroti N, Pearson DG, Pamato MG, Alvaro M, Peruzzo L, Gurney JJ, Moore AE, Davidson J (2018) $CaSiO_3$ perovskite in diamond indicates the recycling of oceanic crust into the lower mantle. Nature 555:237–241

Nimis P (2022) Pressure and temperature data for diamonds. Rev Mineral Geochem 88:533–566

Nimis P, Nestola F, Schiazza M, Reali R, Agrosi G, Mele D, Tempesta G, Howell D, Hutchison MT, Spiess R (2019) Fe-rich ferropericlase and magnesiowustite inclusions reflecting diamond formation rather than ambient mantle. Geology 47:27–30

Nishihara Y, Takahashi E (2001) Phase relation and physical properties of an Al-depleted komatiite to 23 GPa. Earth Planet Sci Lett 190:65–77

Nishiyama N, Yagi T (2003) Phase relation and mineral chemistry in pyrolite to 2200 degrees C under the lower mantle pressures and implications for dynamics of mantle plumes. J Geophys Res-Solid Earth 108(B5):2255

Nishiyama N, Irifune T, Inoue T, Ando J, Funakoshi K (2004) Precise determination of phase relations in pyrolite across the 660 km seismic discontinuity by in situ X-ray diffraction and quench experiments. Phys Earth Planet Sci 143:185–199

Ohtani E (2015) Hydrous minerals and the storage of water in the deep mantle. Chem Geol 418:6–15

Ohtani E (2020) The role of water in Earth's mantle. Natl Sci Rev 7:224–232

Ohtani E, Litasov K, Hosoya T, Kubo T, Kondo T (2004) Water transport into the deep mantle and formation of a hydrous transition zone. Phys Earth Planet Sci 143:255–269

Okamoto K, Maruyama S (1999) The high-pressure synthesis of lawsonite in the MORB+H_2O system. Am Mineral 84:362–373

Okamoto K, Maruyama S (2004) The eclogite-gametite transformation in the MORB+H_2O system. Phys Earth Planet Sci 146:283–296

Omori S, Komabayashi T, Maruyama S (2004) Dehydration and earthquakes in the subducting slab: empirical link in intermediate and deep seismic zones. Phys Earth Planet Sci 146:297–311

Ono S (1998) Stability limits of hydrous minerals in sediment and mid-ocean ridge basalt compositions: Implications for water transport in subduction zones. J Geophys Res-Solid Earth 103:18253–18267

Ono S, Yasuda A (1996) Compositional change of majoritic garnet in a MORB composition from 7 to 17 GPa and 1400 to 1600 degrees C. Phys Earth Planet Sci 96:171–179

Ono S, Ito E, Katsura T (2001) Mineralogy of subducted basaltic crust (MORB) from 25 to 37 GPa, and chemical heterogeneity of the lower mantle. Earth Planet Sci Lett 190:57–63

Otsuka K, Longo M, McCammon CA, Karato SI (2013) Ferric iron content of ferropericlase as a function of composition, oxygen fugacity, temperature and pressure: Implications for redox conditions during diamond formation in the lower mantle. Earth Planet Sci Lett 365:7–16

Palot M, Cartigny P, Harris JW, Kaminsky FV, Stachel T (2012) Evidence for deep mantle convection and primordial heterogeneity from nitrogen and carbon stable isotopes in diamond. Earth Planet Sci Lett 357:179–193

Palot M, Jacobsen SD, Townsend JP, Nestola F, Marquardt K, Miyajima N, Harris JW, Stachel T, McCammon CA, Pearson DG (2016) Evidence for H_2O-bearing fluids in the lower mantle from diamond inclusion. Lithos 265:237–243

Palot M, Pearson DG, Stachel T, Stern RA, Le Pioufle A, Gurney JJ, Harris JW (2017) The transition zone as a host for recycled volatiles: Evidence from nitrogen and carbon isotopes in ultra-deep diamonds from Monastery and Jagersfontein (South Africa). Chem Geol 466:733–749

Pearson DG, Canil D, Shirey SB (2003) Mantle samples included in volcanic rocks: xenoliths and diamonds. *In*: Treatise on Geochemistry. Vol 2. RW C, (ed), p 171–277

Pearson DG, Brenker FE, Nestola F, McNeill J, Nasdala L, Hutchison MT, Matveev S, Mather K, Silversmit G, Schmitz S, Vekemans B (2014) Hydrous mantle transition zone indicated by ringwoodite included within diamond. Nature 507:221–224

Petts DC, Chacko T, Stachel T, Stern RA, Heaman LM (2015) A nitrogen isotope fractionation factor between diamond and its parental fluid derived from detailed SIMS analysis of a gem diamond and theoretical calculations. Chem Geol 410:188–200

Pla Cid J, Nardi LVS, Pla Cid C, Gisbert PE, Balzaretti NM (2014) Acid compositions in a veined-lower mantle, as indicated by inclusions of (K,Na)-hollandite + SiO_2 in diamonds. Lithos 196:42–53

Poli S, Schmidt MW (2002) Petrology of subducted slabs. Annu Rev Earth Planet Sci 30:207–235

Proyer A, Habler G, Abart R, Wirth R, Krenn K, Hoinkes G (2013) TiO_2 exsolution from garnet by open-system precipitation: evidence from crystallographic and shape preferred orientation of rutile inclusions. Contrib Mineral Petrol 166:211–234

Regier ME, Pearson DG, Stachel T, Luth RW, Stern RA, Harris JW (2020) The lithospheric-to-lower-mantle carbon cycle recorded in superdeep diamonds. Nature 585:234–238

Ricolleau A, Perrillat JP, Fiquet G, Daniel I, Matas J, Addad A, Menguy N, Cardon H, Mezouar M, Guignot N (2010) Phase relations and equation of state of a natural MORB: Implications for the density profile of subducted oceanic crust in the Earth's lower mantle. J Geophys Res-Solid Earth 115:B08202

Ringwood AE (1991) Phase-transformations and their bearing on the constitution and dynamics of the mantle. Geochim Cosmochim Acta 55:2083–2110

Rohrbach A, Schmidt MW (2011) Redox freezing and melting in the Earth's deep mantle resulting from carbon–iron redox coupling. Nature 472:209–212

Rzehak LJA, Rohrbach A, Vollmer C, Hofer HE, Berndt J, Klemme S (2020) Ferric–ferrous iron ratios of experimental majoritic garnet and clinopyroxene as a function of oxygen fugacity. Am Mineral 105:1866–1874

Schmandt B, Jacobsen SD, Becker TW, Liu ZX, Dueker KG (2014) Dehydration melting at the top of the lower mantle. Science 344:1265–1268

Schulze DJ, Coopersmith HG, Harte B, Pizzolato LA (2008) Mineral inclusions in diamonds from the Kelsey Lake Mine, Colorado, USA: Depleted Archean mantle beneath the Proterozoic Yavapai Province. Geochim Cosmochim Acta 72:1685–1695

Scott-Smith BH, Danchnin RV, Harris JW, Stracke KJ (1984) Kimberlites near Orrorroo, South Australia. *In*: Kimberlites I: Kimberlites and Related Rocks. Kornprobst J (ed) Elsevier, Amsterdam, p 121–242

Secchiari A, Montanini A, Bosch D, Macera P, Cluzel D (2020) Sr, Nd, Pb and trace element systematics of the New Caledonia harzburgites: Tracking source depletion and contamination processes in a SSZ setting. Geosci Front 11:37–55

Seitz HM, Brey GP, Harris JW, Durali-Muller S, Ludwig T, Hofer HE (2018) Ferropericlase inclusions in ultradeep diamonds from Sao Luiz (Brazil): high Li abundances and diverse Li-isotope and trace element compositions suggest an origin from a subduction melange. Mineral Petrol 112:291–300

Shirey SB, Cartigny P, Frost DJ, Keshav S, Nestola F, Nimis P, Pearson DG, Sobolev NV, Walter MJ (2013) Diamonds and the geology of mantle carbon. *In*: Carbon in Earth. Vol 75. Hazen RM, Jones AP, Baross JA (eds) p 355–421

Shirey S, Smit K, Pearson D, Walter M, Aulbach S, Brenker F, Bureau H, Burnham A, Cartigny P, Chacko T, Frost D (2019) Diamonds and the mantle geodynamics of carbon: deep mantle carbon evolution from the diamond record. *In*: Deep Carbon: Past to Present. Orcutt BN, Daniel I, Dasgupta R, (eds). Cambridge University Press, Cambridge, U.K., p 89–128

Shirey SB, Wagner LS, Walter MJ, Pearson DG, van Keken PE (2021) Slab transport of fluids to deep focus earthquake depths – thermal modeling constraints and evidence from diamonds. AGU Adv 2:e2020AV000304

Smart KA, Chacko T, Stachel T, Muehlenbachs K, Stern RA, Heaman LM (2011) Diamond growth from oxidized carbon sources beneath the Northern Slave Craton, Canada: A delta C-13–N study of eclogite-hosted diamonds from the Jericho kimberlite. Geochim Cosmochim Acta 75:6027–6047

Smit KV, Shirey SB, Stern RA, Steele A, Wang WY (2016) Diamond growth from C–H–N–O recycled fluids in the lithosphere: Evidence from CH micro-inclusions and delta C-13–delta N-15–N content in Marange mixed-habit diamonds. Lithos 265:68–81

Smit KV, Stachel T, Luth RW, Stern RA (2019) Evaluating mechanisms for eclogitic diamond growth: An example from Zimmi Neoproterozoic diamonds (West African craton). Chem Geol 520:21–32

Smit KV, Timmerman S, Aulbach S, Shirey SB, Richardson SH, Phillips D, Pearson DG (2022) Geochronology of diamonds. Rev Mineral Geochem 88:567–636

Smith EM, Kopylova MG (2014) Implications of metallic iron for diamonds and nitrogen in the sublithospheric mantle. Can J Earth Sci 51:510–516

Smith CB, Walter MJ, Bulanova GP, Mikhail S, Burnham AD, Gobbo L, Kohn SC (2016a) Diamonds from Dachine, French Guiana: A unique record of early Proterozoic subduction. Lithos 265:82–95

Smith EM, Shirey SB, Nestola F, Bullock ES, Wang JH, Richardson SH, Wang WY (2016b) Large gem diamonds from metallic liquid in Earth's deep mantle. Science 354:1403–1405

Smith EM, Shirey SB, Wang WY (2017) The very deep origin of the world's biggest diamonds. Gems Gemol 53:388–403

Smith EM, Shirey SB, Richardson SH, Nestola F, Bullock ES, Wang JH, Wang WY (2018) Blue boron-bearing diamonds from Earth's lower mantle. Nature 560:84–87

Smith EM, Ni P, Shirey SB, Richardson SH, Wang WY, Shahar A (2021) Heavy iron in large gem diamonds traces deep subduction of serpentinized ocean floor. Sci Adv 7: eabe9773

Sobolev NV, Wirth R, Logvinova AM, Yelisseyev AP, Kuzmin DV (2016) Retrograde isochemical phase transformations of majoritic garnets included in diamonds: A case study of subcalcic Cr-rich majoritic pyrope from a Snap Lake diamond, Canada. Lithos 265:267–277

Sokolova TS, Dorogokupets PI (2021) Equations of state of Ca-silicates and phase diagram of the $CaSiO_3$ system under upper mantle conditions. Minerals 11:322

Stachel T (2001) Diamonds from the asthenosphere and the transition zone. Euro J Mineral 13:883–892

Stachel T, Harris JW (1997) Syngenetic inclusions in diamond from the Birim field (Ghana)—A deep peridotitic profile with a history of depletion and re-enrichment. Contrib Mineral Petrol 127:336–352

Stachel T, Harris JW (2008) The origin of cratonic diamonds—Constraints from mineral inclusions. Ore Geol Rev 34:5–32

Stachel T, Luth RW (2015) Diamond formation—Where, when and how? Lithos 220:200–220

Stachel T, Harris JW, Brey GP (1998a) Rare and unusual mineral inclusions in diamonds from Mwadui, Tanzania. Contrib Mineral Petrol 132:34–47

Stachel T, Viljoen KS, Brey G, Harris JW (1998b) Metasomatic processes in lherzolitic and harzburgitic domains of diamondiferous lithospheric mantle: REE in garnets from xenoliths and inclusions in diamonds. Earth Planet Sci Lett 159:1–12

Stachel T, Brey GP, Harris JW (2000a) Kankan diamonds (Guinea) I: from the lithosphere down to the transition zone. Contrib Mineral Petrol 140:1–15

Stachel T, Harris JW, Brey GP, Joswig W (2000b) Kankan diamonds (Guinea) II: lower mantle inclusion parageneses. Contrib Mineral Petrol 140:16–27

Stachel T, Harris JW, Aulbach S, Deines P (2002) Kankan diamonds (Guinea) III: delta C-13 and nitrogen characteristics of deep diamonds. Contrib Mineral Petrol 142:465–475

Stachel T, Aulbach S, Brey GP, Harris JW, Leost I, Tappert R, Viljoen KS (2004) The trace element composition of silicate inclusions in diamonds: a review. Lithos 77:1–19

Stachel T, Brey GP, Harris JW (2005) Inclusions in sublithospheric diamonds: Glimpses of deep Earth. Elements 1:73–78

Stachel T, Aulbach S, Harris JW (2022a) Mineral inclusions in lithospheric diamonds. Rev Mineral Geochem 88:307–392

Stachel T, Cartigny P, Chacko T, Pearson DG (2022b) Carbon and nitrogen in mantle-derived diamonds. Rev Mineral Geochem 88:809–876

Stagno V, Ojwang DO, McCammon CA, Frost DJ (2013) The oxidation state of the mantle and the extraction of carbon from Earth's interior. Nature 493:84–88

Stixrude L, Lithgow-Bertelloni C (2011) Thermodynamics of mantle minerals-II. Phase equilibria. Geophys J Int 184:1180–1213

Sueda Y, Irifune T, Yamada A, Inoue T, Liu X, Funakoshi KI (2006) The phase boundary between $CaSiO_3$ perovskite and Ca_2SiO_4+$CaSi_2O_5$ determined by in situ X-ray observations. Geophys Res Lett 33:L10307

Sun CG, Dasgupta R (2019) Slab-mantle interaction, carbon transport, and kimberlite generation in the deep upper mantle. Earth Planet Sci Lett 506:38–52

Sun YZ, Hier-Majumder S, Xu YG, Walter M (2020) Stability and migration of slab-derived carbonate-rich melts above the transition zone. Earth Planet Sci Lett 531:1160000

Sun YZ, Hier-Majumder S, Tauzin B, Walter MJ, Ballmer M, Xu YG, Kim S (2021) Evidence of volatile-induced melting in the Northeast Asian Upper Mantle. J Geophys Res-Solid Earth 126:e2021JB022167

Sunagawa I (1984) Morphology of natural and synthetic diamond crystals. *In*: Materials Science of the Earth's Interior. Sunagawa I, (ed) Terra Science, Tokyo, p 303–330

Sverjensky DA, Huang F (2015) Diamond formation due to a pH drop during fluid–rock interactions. Nat Commun 6:8702

Tao RBA, Fei YW, Bullock ES, Xu C, Zhang LF (2018) Experimental investigation of Fe^{3+}-rich majoritic garnet and its effect on majorite geobarometer. Geochim Cosmochim Acta 225:1–16

Tappert R, Stachel T, Harris JW, Muehlenbachs K, Ludwig T, Brey GP (2005) Diamonds from Jagersfontein (South Africa): messengers from the sublithospheric mantle. Contrib Mineral Petrol 150:505–522

Tappert R, Foden J, Stachel T, Muehlenbachs K, Tappert M, Wills K (2009a) The diamonds of South Australia. Lithos 112:806–821

Tappert R, Foden J, Stachel T, Muehlenbachs K, Tappert M, Wills K (2009b) Deep mantle diamonds from South Australia: A record of Pacific subduction at the Gondwanan margin. Geology 37:43–46

Thompson AB (1992) Water in the Earth's upper mantle. Nature 358:295–302

Thomson AR (2017) Diamonds from the lower mantle? Am Mineral 102:929–930

Thomson AR, Kohn SC, Bulanova GP, Smith CB, Araujo D, Walter MJ, Eimf (2014) Origin of sub-lithospheric diamonds from the Juina-5 kimberlite (Brazil): constraints from carbon isotopes and inclusion compositions. Contrib Mineral Petrol 168:1081

Thomson AR, Walter MJ, Kohn SC, Brooker RA (2016a) Slab melting as a barrier to deep carbon subduction. Nature 529:76–79

Thomson AR, Kohn SC, Bulanova GP, Smith CB, Araujo D, Walter MJ (2016b) Trace element composition of silicate inclusions in sub-lithospheric diamonds from the Juina-5 kimberlite: Evidence for diamond growth from slab melts. Lithos 265:108–124

Thomson AR, Crichton WA, Brodholt JP, Wood IG, Siersch NC, Muir JMR, Dobson DP, Hunt SA (2019) Seismic velocities of $CaSiO_3$ perovskite can explain LLSVPs in Earth's lower mantle. Nature 572:643–647

Thomson AR, Kohn SC, Prabhu A, Walter MJ (2021) Evaluating the formation pressure of diamond-hosted majoritic garnets; A machine learning majorite barometer. J Geophys Res-Solid Earth 126:e2020JB020604

Timmerman S, Honda M, Burnham AD, Amelin Y, Woodland S, Pearson DG, Jaques AL, Le Losq C, Bennett VC, Bulanova GP, Smith CB (2019) Primordial and recycled helium isotope signatures in the mantle transition zone. Science 365:692–694

Tronnes RG, Frost DJ (2002) Peridotite melting and mineral–melt partitioning of major and minor elements at 22–24.5 GPa. Earth Planet Sci Lett 197:117–131

Tschauner O, Huang SC, Yang SY, Humayun M, Liu WJ, Corder SNG, Bechtel HA, Tischler J, Rossman GR (2021) Discovery of davemaoite, $CaSiO_3$-perovskite, as a mineral from the lower mantle. Science 374:891–894

Uenver-Thiele L, Woodland AB, Ballaran TB, Miyajima N, Frost DJ (2017) Phase relations of $MgFe_2O_4$ at conditions of the deep upper mantle and transition zone. Am Mineral 102:632–642

Ulmer P, Sweeney RJ (2002) Generation and differentiation of group II kimberlites: Constraints from a high-pressure experimental study to 10 GPa. Geochim Cosmochim Acta 66:2139–2153

van Keken PE, Hacker BR, Syracuse EM, Abers GA (2011) Subduction factory: 4. Depth-dependent flux of H_2O from subducting slabs worldwide. J Geophys Res-Solid Earth 116:B01401

Walter MJ (1998) Melting of garnet peridotite and the origin of komatiite and depleted lithosphere. J Petrol 39:29–60

Walter MJ, Nakamura E, Tronnes RG, Frost DJ (2004) Experimental constraints on crystallization differentiation in a deep magma ocean. Geochim Cosmochim Acta 68:4267–4284

Walter MJ, Bulanova GP, Armstrong LS, Keshav S, Blundy JD, Gudfinnsson G, Lord OT, Lennie AR, Clark SM, Smith CB, Gobbo L (2008) Primary carbonatite melt from deeply subducted oceanic crust. Nature 454:622–625

Walter MJ, Kohn SC, Araujo D, Bulanova GP, Smith CB, Gaillou E, Wang J, Steele A, Shirey SB (2011) Deep mantle cycling of oceanic crust: Evidence from diamonds and their mineral inclusions. Science 334:54–57

Walter MJ, Thomson AR, Wang W, Lord OT, Ross J, McMahon SC, Baron MA, Melekhova E, Kleppe AK, Kohn SC (2015) The stability of hydrous silicates in Earth's lower mantle: Experimental constraints from the systems $MgO–SiO_2–H_2O$ and $MgO–Al_2O_3–SiO_2–H_2O$. Chem Geol 418:16–29

Walter MJ, Thomson AR, Smith EM (2022) Major and trace element composition of sublithospheric inclusions in diamond. https://doi.org/10.5683/SP3/LIVK1K, Scholars Portal Dataverse, V1.

Wang YB, Weidner DJ (1994) Thermoelasticity of $CaSiO_3$ perovskite and implications for the lower mantle. Geophys Res Lett 21:895–898

Wang WY, Takahashi E (2000) Subsolidus and melting experiments of K-doped peridotite KLB-1 to 27 GPa: Its geophysical and geochemical implications. J Geophys Res-Solid Earth 105:2855–2868

Wang WY, Gasparik T, Rapp RP (2000a) Partitioning of rare earth elements between CaSiO3 perovskite and coexisting phases: constraints on the formation of $CaSiO_3$ inclusions in diamonds. Earth Planet Sci Lett 181:291–300

Wang WY, Sueno S, Takahashi E, Yurimoto H, Gasparik T (2000b) Enrichment processes at the base of the Archean lithospheric mantle: observations from trace element characteristics of pyropic garnet inclusions in diamonds. Contrib Mineral Petrol 139:720–733

Wang JT, Takahashi E, Xiong XL, Chen LL, Li L, Suzuki T, Walter MJ (2020) The water-saturated solidus and second critical endpoint of peridotite: Implications for magma genesis within the mantle wedge. J Geophys Res-Solid Earth 125:e2020JB019452

Waychunas GA (1987) Synchrotron radiation XANES spectroscopy of Ti in minerals—Effects of Ti bonding distances, Ti valence, and site geometry on absorption-edge structure. Am Mineral 72:89–101

Weiss Y, Griffin WL, Navon O (2013) Diamond-forming fluids in fibrous diamonds: The trace-element perspective. Earth Planet Sci Lett 376:110–125

Weiss Y, Kiflawi I, Davies N, Navon O (2014) High-density fluids and the growth of monocrystalline diamonds. Geochim Cosmochim 141:145–159

Wenz MD, Jacobsen SD, Zhang DZ, Regier M, Bausch HJ, Dera PK, Rivers M, Eng P, Shirey SB, Pearson DG (2019) Fast identification of mineral inclusions in diamondat GSECARS using synchrotron X-ray microtomography, radiography and diffraction. J Synchrotron Radiat 26:1763–1768

Wicks JK, Duffy T (2016) Crystal structures of minerals in the lower mantle. *In*: Deep Earth: Physics and Chemistry of the Lower Mantle and Core. Terasaki H, Fischer RA, (eds). Americam Geophysical Union, Washington, D.C., p 69–87

Wijbrans CH, Rohrbach A, Klemme S (2016) An experimental investigation of the stability of majoritic garnet in the Earth's mantle and an improved majorite geobarometer. Contrib Mineral Petrol 171

Wilding MC, Harte B, Harris JW (1991) Evidence for a deep origin for Sao Luiz diamonds. Extd Abstrs 5th Int Kimb Conf:456–458

Wirth R, Vollmer C, Brenker F, Matsyuk S, Kaminsky F (2007) Inclusions of nanocrystalline hydrous aluminium silicate "Phase Egg" in superdeep diamonds from Juina (Mato Grosso State, Brazil). Earth Planet Sci Lett 259:384–399

Wirth R, Dobrzhinetskaya L, Harte B, Schreiber A, Green HW (2014) High-Fe (Mg, Fe)O inclusion in diamond apparently from the lowermost mantle. Earth Planet Sci Lett 404:365–375

Wood BJ (2000) Phase transformations and partitioning relations in peridotite under lower mantle conditions. Earth Planet Sci Lett 174:341–354

Woodland AB, Girnis AV, Bulatov VK, Brey GP, Hofer HE (2020) Breyite inclusions in diamond: Experimental evidence for possible dual origin. Euro J Mineral 32:171–185

Yagi T, Mao HK, Bell PM (1978) Structure and crystal-chemistry of perovskite-type $MgSiO_3$. Phys Chem Mineral 3:97–110

Yasuda A, Fujii T, Kurita K (1994) Melting phase-relations of an anhydrous midocean ridge basalt from 3 to 20 GPa—Implications for the behavior of subducted oceanic–crust in the mantle. J Geophys Res-Solid Earth 99:9401–9414

Zedgenizov DA, Kagi H, Shatsky VS, Ragozin AL (2014a) Local variations of carbon isotope composition in diamonds from Sao-Luis (Brazil): Evidence for heterogenous carbon reservoir in sublithospheric mantle. Chem Geol 363:114–124

Zedgenizov DA, Shatskiy A, Ragozin AL, Kagi H, Shatsky VS (2014b) Merwinite in diamond from Sao Luiz, Brazil: A new mineral of the Ca-rich mantle environment. Am Mineral 99:547–550

Zedgenizov DA, Shatsky VS, Panin AV, Evtushenko OV, Ragozin AL, Kagi H (2015) Evidence for phase transitions in mineral inclusions in superdeep diamonds of the Sao Luiz deposit (Brazil). Russian Geol Geophys 56:296–305

Zedgenizov DA, Ragozin AL, Kalinina VV, Kagi H (2016) The mineralogy of Ca-rich inclusions in sublithospheric diamonds. Geochem Int 54:890–900

Zedgenizov D, Kagi H, Ohtani E, Tsujimori T, Komatsu K (2020) Retrograde phases of former bridgmanite inclusions in superdeep diamonds. Lithos 370: 105659

Zhang JZ, Li B, Utsumi W, Liebermann RC (1996) In situ X-ray observations of the coesite–stishovite transition: Reversed phase boundary and kinetics. Phys Chem Mineral 23:1–10

Zhang YF, Wang C, Jin ZM (2020) Decarbonation of stagnant slab in the mantle transition zone. J Geophys Res-Solid Earth 125:e2020JB019533

Zhu F, Li J, Liu JC, Lai XJ, Chen B, Meng Y (2019) Kinetic control on the depth distribution of superdeep diamonds. Geophys Res Lett 46:1984–1992